MICROWAVE AND MILLIMETER-WAVE PROPAGATION AND SCATTERING IN DENSE RANDOM MEDIA: MODELING AND EXPERIMENTS

Adib Nashashibi

September, 1995

RL-928 = RL-928

MICROWAVE AND MILLIMETER-WAVE PROPAGATION AND SCATTERING IN DENSE RANDOM MEDIA: MODELING AND EXPERIMENTS

by

Adib Yacoub Nashashibi

A dissertation submitted in partial fulfillment
of the requirements for the degree of
Doctor of Philosophy
(Electrical Engineering)
in The University of Michigan
1995

Doctoral Committee:
Assistant Professor Kamal Sarabandi, Chair
Professor Anthony W. England
Professor Linda Katehi
Professor Fawwaz T. Ulaby
Professor John F. Vesecky

© Adib Yacoub Nashashibi 1995
All Rights Reserved

To my parents,

my sisters May and Rula,

and to my brother Mohammad.

ACKNOWLEDGEMENTS

My sincere gratitude and deepest appreciation goes to Professor Kamal Sarabandi for his patience, valuable advice, and constant encouragements during my Ph.D. journey. I thank him for being both my advisor and my friend. Special thanks go to Professor Fawwaz T. Ulaby for introducing me to microwave remote sensing and from whom I learned a lot both in class and during several projects. His generous financial support is deeply appreciated. I would also like to thank all the members of my committee for their time and consideration.

I would like to thank all the people who helped with the experiments reported in this thesis. Special thanks go to Mr. Ron Hartikka for his advice and assistance in the Laboratory. My thanks and gratitude goes to my friend Mr. Paul Siqueira for his help in the Laboratory and for the many technical discussions that we had.

I would like to thank all the support staff in the Radiation Laboratory. Special thanks go to Ms. Sue Duncan, Ms. Jan Rosan, Ms. Sharon Rider, Ms. Patty Wolf, Ms. Carol Tee, and Ms. Bonnie Kidd. I salute them for their prompt help and ever lasting smiles.

I would also like to thank all my friends in the Radiation Laboratory who helped me in many technical and non-technical matters. I thank Mr. Jim Stiles, Dr. John

Kendra, Mr. Roger De Roo, Professor Valdis Liepa, Dr. Leland Pierce, Dr. Yisok Oh, Dr. John Galantowicz, Dr. Richard Austin, Ms. Jasmeet Judge, and Mr. Ed Kim.

Special thanks go to my friends Mr. Nabeel Abel-Jabbar and Dr. Issa Fitian for their support and encouragements. Their unconditional friendship is deeply appreciated. I would like to express also my deepest appreciation and respect to my best friend and my colleague over the last 15 years, Dr. Nihad I. b. His continuing friendship and sincere concern for me across the borders is greatly appreciated.

last but not least, I would like to thank my family for their unlimited support, love, confidence, and encouragements during my Ph.D. journey.

TABLE OF CONTENTS

LIST OF TABLES

LIST OF FIGURES

Figure

CHAPTER I

INTRODUCTION

1.1 Background

Remote sensing is not an alien concept to people. Every person practices remote sensing on a daily basis through a unique biological sensor, called the eye, intended for detecting optical waves. It is not surprising that the oldest and perhaps the most mature area of remote sensing is optical sensing. The ease at which the human brain can process and analyze an optical image has allowed optical sensors to become the primary remote sensing tools in many applications, such as mapping of snow, cloud, and vegetation cover. Of similar interest is the use of microwaves and millimeter-waves in remote sensing.

Development of radars during World War II and its success in detecting targets in adverse weather conditions and during night missions has directed the attention of the remote sensing community to two branches of the electromagnetic spectrum, namely, microwave and millimeter-wave frequencies. In particular, microwave remote sensing of the Earth has become an important source of information in monitoring the Earth's environment. The microwave spectrum of the electromagnetic waves offer certain advantages over the optical spectrum for the purpose of remote sensing the environment. For example microwaves have the ability to penetrate through clouds

(and to some extent rain) and microwave sensors can operate independent of the sun as a source of illumination. As a result, microwave remote sensing has been applied to many branches of science such as meteorological studies and weather prediction [32], geologic mapping [2], and hydrology for the estimation of the moisture content of soil [63].

Millimeter-waves are, on the other hand, late arrivals to the remote sensing arena. Millimeter-waves enjoy, for the most part, the same advantages as microwaves have over optical waves, and millimeter-wave sensors surpass microwave sensors with their high resolution and compactness. Nevertheless, millimeter-wave remote sensing has not received as much attention as microwave and optical remote sensing. The trailing of millimeter-wave remote sensing can be attributed mainly to the technological difficulties associated with building reliable millimeter-wave sensors. With recent advancements in solid-state technology, reliable millimeter-wave components have become available and similarly, interest in millimeter-wave remote sensing is on the rise. Because of the high resolution and compactness of millimeter-wave radars, they have become primary sensors for certain applications such as target discrimination and detection. Nevertheless, the study of millimeter-wave interactions with natural terrain is still at its initial stages [21], [67], [65], [29], [4], [64].

Radar polarimetry is another subject of great importance in remote sensing. As opposed to the conventional single polarization radars, where only one component of the scattered wave is measured and analyzed, polarimetric radars permit the measurement of the full polarization response of the target thereby gathering more information about the target. The full polarization response of a target can be expressed through the scattering matrix, which is a 2×2 matrix of complex numbers, or equivalently, the Mueller matrix, which is a 4×4 matrix of real numbers [60]. In general, the

full polarimetric response of a target contains information about the structure and composition of the target which cannot be revealed from the single polarization response. In many geophysical applications, this additional information can be used for estimating the desired physical parameters of the target. For example, in the case of snow, these physical parameters may be the depth and fractional volume of a snowpack. Polarimetric response can also be used as part of a polarization synthesis technique to discriminate between man-made targets and the background clutter. While a microwave polarimetric radar is configured to measure the complete scattering matrix of a target by measuring the magnitude and phase of the scattered electric field for all linear polarization combinations, a millimeter-wave polarimetric radar measures the full polarimetric response using a different technique, called the coherent-on-receive technique [61],[30]. In this technique, the receiver consists of two orthogonal polarization channels that are capable of measuring simultaneously the magnitudes and phases of the two orthogonal components of the reflected signal. With this technique, the Mueller matrix of a target is obtained from four receiver measurements corresponding to four different transmit polarization states.

1.2 Motivations and Objectives

This thesis is concerned with microwave and millimeter-wave propagation and scattering from dense random media. Examples of naturally occurring dense media are snowpacks, bare soil surfaces, and sand dunes.

The study of millimeter-wave interactions with bare soil surfaces is of importance since soil surfaces contribute both directly and indirectly to the backscatter response from different types of terrain. Radar backscatter from bare soil is influ-

enced, in general, by two sets of parameters: (1) physical parameters such as the permittivities, fractional volumes, and size distributions of the different constituents of the soil medium, and surface roughness statistics, and (2) radar parameters such as frequency, polarization, and incidence angle. At microwave frequencies a set of polarimetric measurements, aimed at characterizing the backscatter response from soil surfaces, was conducted over a number of bare soil surfaces with different roughness and moisture conditions [33]. These measurements, which were supported by an extensive collection of ground truth data, were able to shed light on the dependence of the backscatter response for a given frequency, incidence angle, and polarization configuration on the physical parameters of the soil medium. In addition, an empirical surface scattering model was developed [33] to predict the microwave radar backscatter response from bare soil surfaces. A similar study would be of value to millimeter-wave radar design engineers as they design sensors that can discriminate between man-made targets and bare soil surfaces. Unfortunately, very few documented studies of polarimetric radar backscatter from bare soils that were conducted at millimeter-wave frequencies can be found in the open literature [9], [36], [66], [7]. Due to the lack of precise ground truth data, accurate calibrations, complete angular and/or polarization response measurements, the existing data sets have not been able to contribute much to the understanding of the scattering from soil surfaces. Therefore, no reliable model that can predict the backscatter response from soil surfaces at millimeter-wave frequencies is available.

Volume scattering from dense random media has received a lot of interest over the past decade. This is because the depth and fractional volume of a snowpack and the wetness of a soil surface cannot be determined from the microwave backscatter response without considering the volume scattering contribution from within the scat-

tering layer. It should be noted that in a dense random medium where the scatterers occupy a substantial fractional volume ($f > 0.01$), the location of one particle is not independent from the locations of other particles and electromagnetic wave interactions with any one particle cannot be considered in the absence of nearby particles.

A number of theoretical models were developed over the years to predict the volume scattering contribution from layered random media. They can be categorized into two groups: (1) continuous media perturbation approaches such as the Born approximation [22], [5], [55], [23], and (2) discrete scatterer approaches such as radiative transfer [62], [52], [21], [19]. In either of these two approaches, characterization of the propagation constant of the mean-field in the random medium is of great importance. The effective propagation constant specifies how the mean-field propagates in a scattering medium. The real and imaginary parts of the effective propagation constant are respectively proportional to the phase velocity and the attenuation rate caused by absorption and scattering within the medium. For dense random media, analytical models, such as the effective field approximation (EFA) and the quasicrystalline approximation with coherent potential (QCA-CP), are widely used to compute the effective propagation constant. The QCA-CP model which includes in its derivation the effects of multiple scattering between particles has been used in the development of the dense medium radiative transfer theory (DMRT) [53]. In turn, the DMRT has been used to model the backscattering response from layered dense random media [68],[69]. The applicability of these models depends in part on the range of validity of the QCA-CP model which has not yet been determined. Accurate measurements of the effective propagation constant can be used for establishing the range of validity of the existing analytical models. Unfortunately, the inaccuracy associated with the existing free space transmission measurement technique intended for measuring the

effective propagation constant of dense random media (see [27], [17]) hinders any serious effort to determine experimentally the regions of validity of the QCA-CP model.

The goals of this thesis are: (a) accurate characterization of the polarimetric radar backscatter response from bare soil surfaces at millimeter-wave frequencies, and (b) determination of the validity region of existing analytical models that were developed for computing the effective propagation constant of dense random media. To achieve the first goal, the following steps were taken: (1) development of an accurate calibration technique for the millimeter-wave coherent-on-receive polarimetric radars, (2) collection of the radar backscatter response from soil surfaces with different roughnesses and moisture conditions, and (3) collection of ground truth data for the surface roughness, soil moisture, and particle size distribution. A semi-empirical surface scattering model is developed based on the measured polarimetric backscatter response from wet surfaces. The volume scattering contribution from the dielectric inhomogeneities underneath dry soil surfaces is modeled using radiative transfer theory. The total backscatter response from soil surfaces, whether wet or dry, can be predicted by adding both the surface scattering contribution, computed using the semi-empirical model, and the volume scattering contribution, computed using radiative transfer theory.

To achieve the second goal, the following steps are taken: (1) development of a new technique for measuring the effective propagation constant of dense random media that circumvents the problems associated with the free space transmission measurement technique, (2) performance of an experimental examination on the dependence of the effective propagation constant on the physical and electrical parameters describing a dense random medium.

1.3 Thesis Overview

In this section, the outline of the thesis is first presented, then the contents of each chapter are discussed briefly. In chapter 2, a detailed description of the coherent-on-receive millimeter-wave polarimetric radar, to be used in the measurements reported in Chapters 3 and 4, is discussed. In addition, a new and accurate calibration technique is developed. In Chapters 3 and 4, polarimetric backscatter measurements of bare soil surfaces conducted at millimeter-wave frequencies are described and a hybrid model that characterizes the surface and volume scattering contributions from soil surfaces is developed. In Chapter 5, a new technique for measuring the bistatic scattering matrix of a point target using a monostatic radar and a ground plane is explained. This technique is the backbone of a second technique, developed and verified in Chapter 6, which is intended for measuring the effective propagation constant of dense random medium regardless of the physical properties of the medium. In Chapter 7, an experimental study of the effective propagation constant aimed at establishing the regions of validity of existing theoretical models is conducted.

In Chapter 2, the principles of operation of the millimeter-wave coherent-on-receive polarimetric radar are discussed and a new technique for calibrating the radar is introduced. The calibration technique requires the use of two calibration targets, a metallic sphere and any depolarizing target (for which knowledge of its scattering matrix is not required) to determine the system distortion parameters. In comparison, other technique requires the use of a sphere and a wire grid (limited by polarization purity of the wire grid). The validity of the new calibration technique is examined by measuring the scattering matrices of spheres and cylinders as test targets using a coherent-on-receive radar operating at 34.5 GHz.

In Chapter 3, the millimeter-wave backscatter response of bare-soil is examined

by conducting experimental measurements at 35 and 94 GHz using a truck-mounted polarimetric scatterometer. The experimental measurements are conducted for three soil surfaces with different roughnesses under both dry and wet conditions. Analysis of the data shows that volume scattering from beneath the soil surface is significant when the soil is dry. This chapter will be devoted to studying the surface scattering component of the total backscatter response. Hence, only wet soil surfaces are examined here while analysis of the measured response from dry soil surfaces is deferred to Chapter 4. The measured backscattering response of wet soil is analyzed and compared to theoretical models. From this, semi-empirical surface scattering model is developed that relates the surface scattering component of the total backscatter to the roughness parameter and the dielectric constant of the soil surface. The proposed model is compared with independently conducted experimental observations of wet soils at 60 GHz done by Yamasaki *et al.* [73].

In Chapter 4, the surface and volume scattering contributions to the measured backscattering response from dry soil surfaces are considered. Evidence on the presence of significant volume scattering from dry soil surfaces at millimeter-wave frequencies is presented. A model based on radiative transfer theory is introduced to compute the volume scattering contribution from a thin dry soil layer with an undulating surface. Then the sum of two contributions, the surface scattering contribution, computed using the semi-empirical model developed in Chapter 3, and the volume scattering contribution, computed using the radiative transfer-based model, is compared with the measured backscattering response from dry soil surfaces.

In Chapter 5, a novel technique for the bistatic scattering measurement of point targets is developed. In this technique, a monostatic radar with fine spatial resolution in conjunction with a rotatable ground plane is used to measure the bistatic scattering

matrix. The new technique circumvents the difficulties associated with the traditional measurement technique. It is shown that for depolarizing targets, an independent radar measurement after loading the ground plane with a dielectric slab is required for determining the cross-polarized components of the bistatic scattering matrix. The accuracy of the new method is demonstrated by comparing the measured bistatic scattering matrices of cylinders and spheres with the theoretical ones over a wide range of scattering angles.

In Chapter 6, a new technique for measuring the effective propagation constant of dense random media is introduced. The proposed method is not restricted by the physical properties of the random medium such as particles size, shape and density. In this technique, the mean bistatic scattered fields of a cluster of random medium, confined in a known geometrical boundary, are measured using a monostatic radar and a rotatable ground plane. The measured mean bistatic scattered fields are fitted to the bistatic scattered fields of a homogeneous lossy material with the same geometrical boundary. Thus, the effective propagation constant of the random medium is the same as that of the homogeneous body that exhibits similar scattered fields. The accuracy of the new technique in measuring the effective propagation constant of a dense random medium was verified both experimentally and numerically in the low volume fraction limiting case. It is also shown that using this technique, the permittivity of low dielectric materials such as styrofoam can be measured very accurately.

In Chapter 7, an experimental study of the effective propagation constant of dense random media aimed at establishing the region of validity of existing theoretical models is performed using the measurement technique developed in Chapter 6. Measurements of the effective propagation constants of different dense random media comprising homogeneous spherical particles with different packing densities are compared

with existing analytical models. It is shown that none of the existing analytical models, including the QCA-CP model that was developed specifically for dense media, are able to predict the extinction accurately at volume fractions beyond 10%. It is also shown that Polder-Van Santen mixing formula can be used to predict the real part of the effective propagation constant with a reasonable accuracy.

CHAPTER II

MILLIMETER-WAVE COHERENT-ON-RECEIVE POLARIMETRIC RADAR SYSTEMS: A NEW CALIBRATION TECHNIQUE

2.1 Introduction

In general, polarimetric radars can be categorized into three major groups: 1) coherent radars, 2) incoherent radars, and 3) coherent-on-receive radars. With coherent radars, which are capable of measuring both the magnitude and the phase of the scattered signal, the scattering matrix of a target can be determined directly. This is accomplished by measuring the scattered waves from the target using two receive channels with orthogonal polarizations for two successive transmissions at each of the two orthogonal polarizations. Although capable of measuring only the magnitude of the scattered wave, incoherent radars can be used to determine the Mueller matrix of a target by measuring the power received in the co-polarized channels for each of six different, independent, transmit polarization states [18]. At microwave frequencies, coherent radar systems are often used because the coherence requirements of the mea-

surement technique can be met by available microwave technology. The incoherent technique, on the other hand, is used mostly at optical wavelengths. Neither of these two types of radar systems is of interest to the present study.

In this thesis we are concerned with the third type of polarimetric radars, namely the coherent-on-receive configuration, which is intermediate between the other two techniques in terms of the coherence requirements imposed by the measurement technique. In this configuration, which has been used successfully at millimeter wavelengths [61],[30], the receiver has two orthogonal polarization channels and is capable of measuring simultaneously the magnitudes and phases of the two signals. With this type of radar, the Mueller matrix of a target can be obtained from four receiver measurements corresponding to four different transmit polarization states.

Measurement accuracy and precision are critical elements of any meaningful analysis or interpretation of the measured data. For radar systems, it is customary to use external calibration techniques to determine the overall system transfer function. By measuring the backscatter from a set of calibration targets with known scattering matrices, the radar distortion parameters, which include channel imbalances, antenna gain, and antenna distortion parameters, can be determined. Then, by applying an inverse algorithm to the data measured for a target of interest, the errors introduced by these parameters can be removed. Several techniques are available for calibrating coherent polarimetric radar systems, including those proposed by Barnes [1], Sarabandi *et al.* [47], and Whitt *et al.* [71]-[72].

Traditionally, calibration of a coherent-on-receive radar is performed in two steps [30]. First, the receiver is calibrated using a wire grid placed in front of the receive antenna at three different orientations (see Fig. 2.1). Then the polarization states of the four desired transmitted waves are determined by measuring the wave backscat-

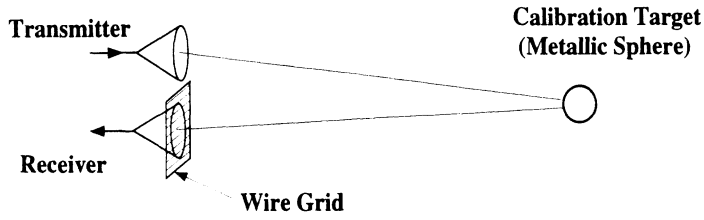

Figure 2.1: In the traditional calibration technique the receiver is calibrated using a wire grid placed in front of the receive antenna.

tered from a corner reflector with the calibrated receiver. In this technique calibration errors caused by the wire grid itself are not considered. The sources of error introduced by the wire grid include: (1) the polarization purity (axial ratio) of the wire grid, which is on the order of that of the receiving antenna (20-30 dB), (2) the proximity of the wire grid to the receiving antenna, which affects the antenna radiation characteristics and (3) errors associated with the grid orientation angles.

In this chapter we propose an alternate technique with which calibration can be performed in two steps and requires measuring the backscatter response of a metallic sphere (or trihedral reflector) in addition to any depolarizing target for four and two transmitted wave polarizations respectively. In this algorithm the knowledge of the scattering matrix of the depolarizing target is not required. By applying this technique, it is possible to determine the polarization states of the transmitted waves, the antennas cross-talk factors and receiver channel imbalances, while avoiding the use of the wire grid.

In the next section, principles of operation of the coherent-on-receive radar are presented in detail. In Section 2.3, the imperfections of the coherent-on-receive radar components are modeled and a system distortion model is constructed. A calibration

procedure is proposed in Section 2.4 that requires the use of two targets, a target with known scattering matrix and any depolarizing target. Finally, in Section 2.5 the validity of the new calibration technique is examined by measuring the scattering matrices of known targets at 34.5 GHz.

2.2 Coherent-on-Receive Polarimetric Radars

The main advantage of the coherent-on-receive radars is in the measurement of random fluctuating targets or when the radar platform is not stable. In this section we briefly introduce the basic concepts of this system to guide the reader in understanding the calibration procedure.

By defining a set of orthogonal directions $\left(\hat{v}, \hat{h}\right)$ in a plane perpendicular to the direction of propagation, the components of the scattered field $\mathbf{E}^s$ from a given target can be related to the components of the incident wave $\mathbf{E}^i$ through the scattering matrix of the target, i.e.,

$$\mathbf{E}^s = \frac{e^{-ik_0 r}}{r} \begin{bmatrix} S_{vv} & S_{vh} \\ S_{hv} & S_{hh} \end{bmatrix} \mathbf{E}^i \tag{2.1}$$

where k_0 is the propagation constant and r is the range from the target to the receive antenna. In general, the polarization state of the transmitted wave can be any arbitrary elliptical polarization. An elliptically polarized wave can be characterized by two angles known as the rotation angle (ψ) and ellipticity angle (χ) [60]. The modified Stokes vector $\mathbf{F}_m(\psi, \chi)$ provides an alternate but equivalent representation

of wave polarization:

$$\mathbf{F}_m(\psi,\chi) = \begin{bmatrix} |E_v|^2 \\ |E_h|^2 \\ 2Re[E_v E_h^*] \\ 2Im[E_v E_h^*] \end{bmatrix}$$

$$= \begin{bmatrix} \frac{1}{2}(1+\cos 2\psi \cos 2\chi) \\ \frac{1}{2}(1-\cos 2\psi \cos 2\chi) \\ \sin 2\psi \cos 2\chi \\ \sin 2\chi \end{bmatrix} \left(|E_v|^2 + |E_h|^2\right) \qquad (2.2)$$

Upon using (2.1) the scattered (received) modified Stokes vector $\mathbf{F}_m^r$ can be related to the incident (transmitted) Stokes vector *via* the modified Mueller matrix $\bar{\bar{\mathcal{L}}}_m$ by

$$\mathbf{F}_m^r = \frac{1}{r^2}\ \bar{\bar{\mathcal{L}}}_m\ \mathbf{F}_m^t \qquad (2.3)$$

where $\bar{\bar{\mathcal{L}}}_m$ is a 4×4 matrix whose entries in terms of the scattering matrix elements are given by

$$\bar{\bar{\mathcal{L}}}_m = \begin{bmatrix} |S_{vv}|^2 & |S_{vh}|^2 & \bullet & \bullet & \bullet \\ |S_{hv}|^2 & |S_{hh}|^2 & & & \\ 2Re(S_{vv}S_{hv}^*) & 2Re(S_{vh}S_{hh}^*) & & & \\ 2Im(S_{vv}S_{hv}^*) & 2Im(S_{vh}S_{hh}^*) & & & \end{bmatrix}$$

$$
\begin{bmatrix}
 & Re(S_{vh}^{*}S_{vv}) & -Im(S_{vh}^{*}S_{vv}) \\
 & Re(S_{hh}^{*}S_{hv}) & -Im(S_{hv}S_{hh}^{*}) \\
\bullet\ \bullet\ \bullet & Re(S_{vv}S_{hh}^{*}+S_{vh}S_{hv}^{*}) & -Im(S_{vv}S_{hh}^{*}-S_{vh}S_{hv}^{*}) \\
 & Im(S_{vv}S_{hh}^{*}+S_{vh}S_{hv}^{*}) & Re(S_{vv}S_{hh}^{*}-S_{vh}S_{hv}^{*})
\end{bmatrix} \tag{2.4}
$$

When dealing with natural targets, such as soil surfaces and vegetation canopies, the quantity of interest is $< \bar{\bar{\mathcal{L}}}_m >$, the ensemble average of $\bar{\bar{\mathcal{L}}}_m$. Given $< \bar{\bar{\mathcal{L}}}_m >$, the technique of polarization synthesis can be used to compute the polarization response of the target under consideration [[60], Chapter 2]. With a coherent polarimetric radar, the process starts by measuring the scattering matrix for many statistically independent samples of the target. Each scattering matrix is converted to its corresponding modified Mueller matrix $\bar{\bar{\mathcal{L}}}_m$, and then all the $\bar{\bar{\mathcal{L}}}_m$ matrices are averaged together. With incoherent and coherent-on-receive polarimetric radars, $< \bar{\bar{\mathcal{L}}}_m >$ is measured directly. To examine how the coherent-on-receive radar functions, consider the two-antenna system shown in Fig. 2.2. The transmitter part of the system consists of an upconverter followed by an RF amplifier with a rectangular waveguide as its output port. The rectangular waveguide is connected to a circular waveguide through a transition, followed by two waveguide polarizers which are connected to the antenna structure. The waveguide polarizers are independently rotatable in a plane perpendicular to the direction of propagation. The dielectric card inside a waveguide polarizer enforces two different wave velocities for waves with polarization vectors parallel and perpendicular to the card's surface. The position of the dielectric card with respect to the polarization of the incoming wave determines the polarization of the outgoing wave from the waveguide polarizer. To minimize reflection by the card, the dielectric constant of the card must be chosen to be relatively small. The dielectric cards are

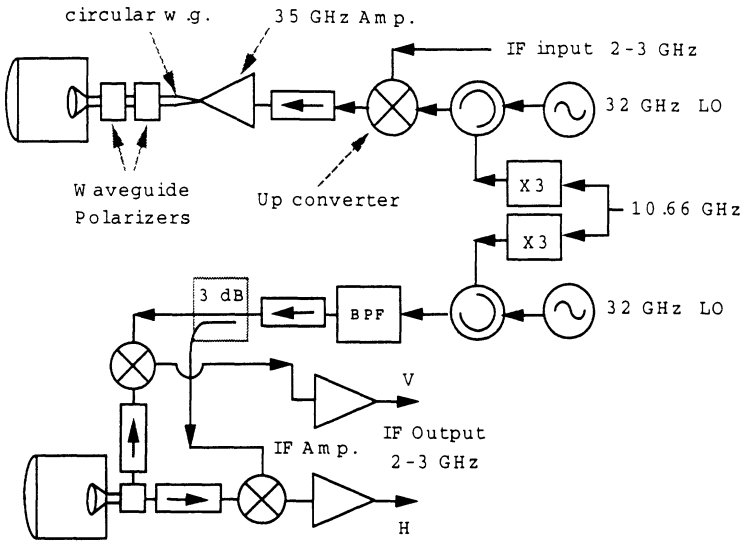

Figure 2.2: Block diagram of the coherent-on-receive radar system operating at 34.5 GHz.

designed such that the phase difference between two outgoing waves corresponding to two incoming waves whose electric fields are parallel and perpendicular to the card is 90°. This feature allows the generation of any polarization configuration of interest including vertical (V), 45° linear (45), left-hand circular (LHC), and right-hand circular (RHC), which together are used to obtain the elements of the Mueller matrix.

The receiver part of the radar includes a dual polarized antenna capable of receiving the vertical and horizontal polarization components of the scattered wave simultaneously. After down-converting the frequency of the received signals, the two IF signals are measured in both magnitude and phase. The Stokes vector corresponding to the transmitted polarization is computed from the coherent measurement of the scattered field components as given by (2.2). For coherent systems, phase coherence must be maintained during the measurement of the scattering matrix elements. Therefore, if the relative position of the radar platform with respect to the target is not fixed to within a very small fraction of a wavelength, the phase information

will be lost. However this is not the case for coherent-on-receive systems, since each column of the Mueller matrix is completely determined from a single pulse.

To measure the Mueller matrix with 16 unknowns, we are required to perform at least four measurements. The entries of the Mueller matrix can easily be obtained by transmitting four different polarizations, namely, vertical, 45° linear, right-hand circular, and left-hand circular, whose modified Stokes vectors are given by

$$\mathbf{F}_v^t = \begin{bmatrix} 1 \\ 0 \\ 0 \\ 0 \end{bmatrix}, \quad \mathbf{F}_{45}^t = \begin{bmatrix} \frac{1}{2} \\ \frac{1}{2} \\ 1 \\ 0 \end{bmatrix}, \quad \mathbf{F}_{LHC} = \begin{bmatrix} \frac{1}{2} \\ \frac{1}{2} \\ 0 \\ 1 \end{bmatrix}, \quad \mathbf{F}_{RHC} = \begin{bmatrix} \frac{1}{2} \\ \frac{1}{2} \\ 0 \\ -1 \end{bmatrix} \tag{2.5}$$

The received Stokes vectors can also be computed using the measured E_v^r and E_h^r in (2.2). By denoting the ith column of the modified Mueller matrix by $\mathcal{L}_m^i$ it is a straightforward matter to show that

$$\begin{aligned} \mathcal{L}_m^1 &= \frac{1}{r^2}\mathbf{F}_V^r \\ \mathcal{L}_m^2 &= \frac{1}{r^2}\left[\mathbf{F}_{LHC}^r + \mathbf{F}_{RHC}^r - \mathbf{F}_V^r\right] \\ \mathcal{L}_m^3 &= \frac{1}{r^2}\left[\mathbf{F}_{45}^r - \frac{1}{2}\left(\mathbf{F}_{LHC}^r + \mathbf{F}_{RHC}^r\right)\right] \\ \mathcal{L}_m^4 &= \frac{1}{r^2}\left[\frac{1}{2}\left(\mathbf{F}_{LHC}^r - \mathbf{F}_{RHC}^r\right)\right] \end{aligned} \tag{2.6}$$

where $\mathbf{F}_p^r$ represents the received Stokes vector corresponding to the transmit polarization p.

In case of distributed targets, measurements of $\mathbf{F}_p^r$ are repeated many times to estimate the expected value $< \mathbf{F}_p^r >$. Then, $< \bar{\bar{\mathcal{L}}}_m >$ can be determined from $< \mathbf{F}_p^r >$ following the procedure outlined by equation (2.6), from which the radar

cross section can be computed for any desired combination of transmit and receive antenna polarizations using the polarization synthesis technique [60].

This procedure of computing $< \bar{\bar{\mathcal{L}}}_m >$ works well for an ideal radar system with the transmitted Stokes vectors as given in (2.5). In practice, the measurements required to compute $< \bar{\bar{\mathcal{L}}}_m >$ are contaminated by two types of errors: systematic errors due to imperfections in the radar components and non-systematic errors due to noise and finite sampling of the random process. The systematic errors can be removed using the calibration procedure described in section 2.4, while the non-systematic errors can be reduced by estimating $< \bar{\bar{\mathcal{L}}}_m >$ using the received Stokes vectors corresponding to N (≥ 4) different transmit polarizations. One possible computation procedure to estimate $< \bar{\bar{\mathcal{L}}}_m >$, as suggested in [30], is to use the least mean squared procedure for individual rows of the Mueller matrix.

Let $\bar{\bar{\mathbf{V}}}$ and $\bar{\bar{\mathbf{W}}}$ be $4 \times N$ matrices whose columns represent the received and transmitted Stokes vectors respectively. It is easy to show from (2.3) that $\bar{\bar{\mathbf{V}}}$ and $\bar{\bar{\mathbf{W}}}$ are related to $\bar{\bar{\mathcal{L}}}_m$ through

$$< \bar{\bar{\mathbf{V}}} > = < \bar{\bar{\mathcal{L}}}_m > \ \bar{\bar{\mathbf{W}}} \tag{2.7}$$

Here, the coefficient $(1/r^2)$ has been suppressed for simplicity. The error in the ith row is defined by

$$e_i = \sum_{j=1}^{N} \left(v_{ij} - \sum_{k=1}^{4} \mathcal{L}_{ik} w_{kj} \right)^2$$

and elements of $\mathcal{L}_{ik}$ are chosen such that e_i is minimized. This procedure ends up with the following expression for the measured Mueller matrix

$$< \bar{\bar{\mathcal{L}}}_m >= \left[(\bar{\bar{\mathbf{W}}} \bar{\bar{\mathbf{W}}}^T)^{-1} \ \bar{\bar{\mathbf{W}}} < \bar{\bar{\mathbf{V}}} >^T \right]^T$$

A better estimation of the Mueller matrix from the measured data is perhaps the global minimization instead of minimization from individual rows. Moreover in backscattering there are only nine independent parameters in the Mueller matrix. The Mueller matrix in terms of the independent parameters can be represented by

$$< \bar{\bar{\mathcal{L}}}_m >= \left\langle \begin{bmatrix} x_1 & x_3 & x_8 & -x_9 \\ x_3 & x_2 & x_6 & -x_7 \\ 2x_8 & 2x_6 & (x_4 + x_3) & -x_5 \\ 2x_9 & 2x_7 & x_5 & (x_4 - x_3) \end{bmatrix} \right\rangle$$

where $x_1 = |S_{vv}|^2$, $x_2 = |S_{hh}|^2$, $x_3 = |S_{hv}|^2$, $x_4 = Re[S_{vv}S_{hh}^*]$, $x_5 = Im[S_{vv}S_{hh}^*]$, $x_6 = Re[S_{hv}S_{hh}^*]$, $x_7 = Im[S_{hv}S_{hh}^*]$, $x_8 = Re[S_{vv}S_{hv}^*]$, and $x_9 = Im[S_{vv}S_{hv}^*]$. Using global minimization, elements of the Mueller matrix ($\mathcal{L}_{ik}$) are obtained such that the global error

$$E = \sum_{i=1}^{4} \sum_{j=1}^{N} \left(v_{ij} - \sum_{k=1}^{4} \mathcal{L}_{ik} w_{kj} \right)^2$$

is minimized. Basically, a linear system of equations for the nine unknown parameters is obtained by setting the partial derivatives of E (with respect to x_i) equal to zero.

2.3 System Distortion Model

The technique described in the preceding section for measuring the Mueller matrix is for a distortion-free radar system. It minimizes the error due to random variations and finite sample size, but it does not correct for system biases. In practice, however, the radar components are not perfect. For example, it is not possible to construct antennas that are totally free of polarization contamination (coupling between the orthogonal polarization ports of the antenna). Also, the polarization state of the trans-

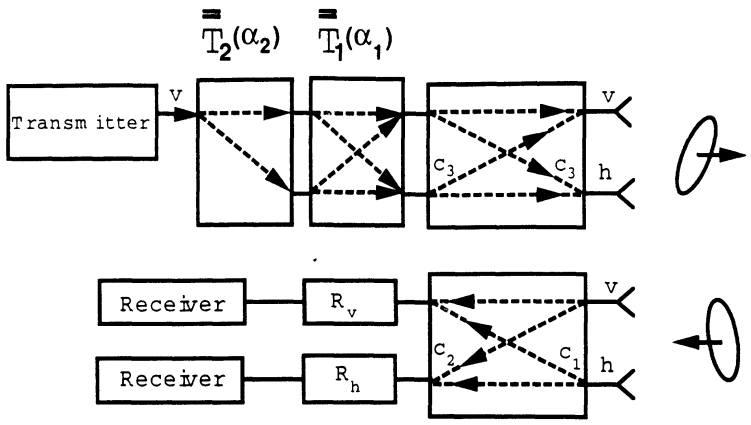

Figure 2.3: Signal flow diagram of a coherent-on-receive radar.

mitted wave depends primarily on the phase-shift characteristics of the waveguide polarizers and the transmit antenna polarization contamination. Another factor that affects the measurement accuracy is the receive channel imbalances which include the variation in magnitude and phase of the system transfer function for different ports of the receiver. A simplified block diagram of such a system is depicted in Fig. 2.3. These imperfections in the radar system components can lead to serious errors in the measured Mueller matrix. The role of calibration is then to correct for these systematic errors in the measured target response before constructing the measured Mueller matrix.

In this section, the imperfections of the radar components will be modelled and a mathematical system distortion model will be constructed. This system distortion model will then form the basis of the new calibration technique discussed in the next section.

First, let us examine the effect of the phase shift introduced by the dielectric cards on the polarization tate of the transmitted wave. As mentioned earlier the thickness and dielectric constant of the dielectric cards are chosen such that the reflected field is minimal and can be ignored. Suppose the transmission coefficient of the card for

the waves whose electric fields are parallel (slow wave) and perpendicular (fast wave) to the dielectric card are, respectively, denoted by the complex quantities Υ_s, and Υ_f. Further assume that the card is oriented such that it makes an angle α with respect to a specified horizontal direction as shown in Fig. 2.4. The unit vectors parallel and perpendicular to the card are denoted by $\hat{s}$ and $\hat{f}$, which are given by

$$\begin{cases} \hat{s} &= \sin\alpha\ \hat{v} - \cos\alpha\ \hat{h} \\ \hat{f} &= \cos\alpha\ \hat{v} + \sin\alpha\ \hat{h} \end{cases}$$

If the wave incident on the card, is denoted by $\mathbf{E}^i = E_v^i\ \hat{v} + E_h^i\ \hat{h}$, then by decomposing each component into components along $\hat{f}$ and $\hat{s}$ and multiplying the resultant components, by the corresponding transmission coefficients Υ_f and Υ_s, the outgoing field through the polarizer can be obtained from

$$\mathbf{E}^o = \bar{\bar{\mathbf{T}}}\ \mathbf{E}^i$$

where $\bar{\bar{\mathbf{T}}}$ is the polarization transformation matrix given by

$$\bar{\bar{\mathbf{T}}} = \begin{bmatrix} \cos^2\alpha\ \Upsilon_f + \sin^2\alpha\Upsilon_s & \sin\alpha\ \cos\alpha\ (\Upsilon_f - \Upsilon_s) \\ \\ \sin\alpha\ \cos\alpha(\Upsilon_f - \Upsilon_s) & \cos^2\alpha\ \Upsilon_s + \sin^2\alpha\ \Upsilon_f \end{bmatrix}$$

Now by cascading two polarizers and ignoring reflections from the cards, the transmitted wave $\mathbf{E}^t$ at the output of the second polarizer is related to the wave at the input of the first polarizer $\mathbf{E}^{in}$ by

$$\mathbf{E}^t = \bar{\bar{\mathbf{T}}}_1\ \bar{\bar{\mathbf{T}}}_2\ \mathbf{E}^{in}$$

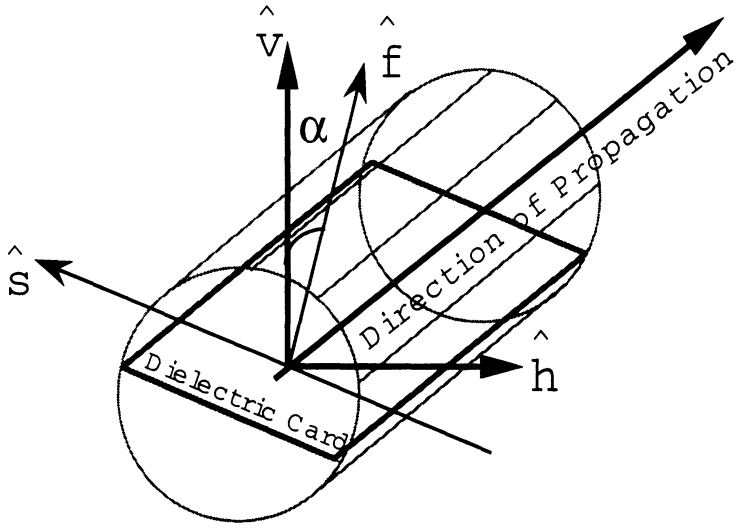

Figure 2.4: Orientation of the principal axes of the dielectric card with respect to $\hat{v}$ and $\hat{h}$.

Here $\bar{\bar{\mathbf{T}}}_1$ and $\bar{\bar{\mathbf{T}}}_2$ are the transformation matrices of the first and second polarizers corresponding to the rotation angles α_1 and α_2 respectively. It is assumed, without loss of generality, that the electric field in the rectangular waveguide preceding the polarizers coincides with the specified vertical direction $\hat{v}$ ($\mathbf{E}^{in} = T_t(1,0)$). Introducing the phase-shift factor $\tau_i = \frac{\Upsilon_{gi}}{\Upsilon_{fi}}$ $(i = 1,2)$ the transmitted wave through the polarizers is given in terms of the phase-shift factors and orientation angles by

$$\mathbf{E}^t = T \begin{bmatrix} \{\cos(\alpha_1 - \alpha_2)(\cos\alpha_1 \cos\alpha_2 + \tau_1\tau_2 \sin\alpha_1 \sin\alpha_2) \\ +\sin(\alpha_1 - \alpha_2)(\sin\alpha_1 \cos\alpha_2\tau_1 - \cos\alpha_1 \sin\alpha_2\tau_2)\} \\ \\ \{\cos(\alpha_1 - \alpha_2)(\sin\alpha_1 \cos\alpha_2 - \cos\alpha_1 \sin\alpha_2\tau_1\tau_2) \\ -\sin(\alpha_1 - \alpha_2)(\cos\alpha_1 \cos\alpha_2\tau_1 + \sin\alpha_1 \sin\alpha_2\tau_2)\} \end{bmatrix} \tag{2.8}$$

where $T = T_t \Upsilon_{f1} \Upsilon_{f2}$ includes the transmitter transfer function (T_t). The nominal

Rotation Angle	v	h	45°	135°	LHC	RHC
α_1	0	45	0	0	45	-45
α_2	0	45	45	-45	0	0

Table 2.1: Wave plates rotation angles for the desired polarization states of the transmitted wave.

value for the phase-shift factors (τ_i) is $e^{-i\frac{\pi}{2}}$ and for this value Table 2.1 gives the rotation angles for the desired polarizations. In general τ_i is not exactly $e^{-i\frac{\pi}{2}}$ and is a function of frequency. Using the above rotation angles, the actual polarizations of the waves transmitted through the polarizers are

$$\tilde{\mathbf{E}}^{tV} = \begin{bmatrix} 1 \\ 0 \end{bmatrix}, \quad \tilde{\mathbf{E}}^{tH} = \begin{bmatrix} \frac{1+\tau_1\tau_2}{2} \\ \frac{1-\tau_1\tau_2}{2} \end{bmatrix},$$

$$\tilde{\mathbf{E}}^{t45} = \begin{bmatrix} \frac{1+\tau_2}{2} \\ \frac{\tau_1-\tau_1\tau_2}{2} \end{bmatrix}, \quad \tilde{\mathbf{E}}^{t135} = \begin{bmatrix} \frac{1+\tau_2}{2} \\ \frac{-\tau_1+\tau_1\tau_2}{2} \end{bmatrix},$$

$$\tilde{\mathbf{E}}^{tLHC} = \begin{bmatrix} \frac{1+\tau_1}{2} \\ \frac{1-\tau_1}{2} \end{bmatrix}, \quad \tilde{\mathbf{E}}^{tRHC} = \begin{bmatrix} \frac{1+\tau_1}{2} \\ \frac{-1+\tau_1}{2} \end{bmatrix}. \tag{2.9}$$

where $\tilde{\mathbf{E}}^{tp} = \mathbf{E}^{tp}/T$. Deviations of τ_1 and τ_2 from their nominal values lead to errors in the presumed polarization states.

The physical structure of the antenna may modify the polarization of the bounded wave as the wave transforms into an unbounded wave and vice versa. The transmitted unbounded wave in terms of the bounded wave at the input is given by

$$\tilde{\mathbf{E}}_o^t = T \begin{bmatrix} 1 & c_3 \\ c_3 & 1 \end{bmatrix} \tilde{\mathbf{E}}^t \tag{2.10}$$

where c_3 ($|c_3| < 1$) is the transmit antenna cross-talk factor. The off-diagonal terms in (2.10) are assumed to be identical because of the circular symmetry of the transmit antenna. It is worth noting that the polarizers and the antenna structure are passive devices, thus the phase-shift factors τ_1 and τ_2 as well as the antenna cross-talk factor c_3 are time invarient.

Now we can turn to study the distortions caused by the receiver. In a recent study reported by Sarabandi and Ulaby [40], it was shown that for a dual polarized receiver the measured signal $\mathbf{E}^r$ is related to the wave incident upon the receive antenna by

$$\mathbf{E}^r = \begin{bmatrix} R_v & 0 \\ 0 & R_h \end{bmatrix} \begin{bmatrix} 1 & c_1 \\ c_2 & 1 \end{bmatrix} \tilde{\mathbf{E}}^r \tag{2.11}$$

where c_1 and c_2 are the receiver cross-talk factors and R_v and R_h are the vertical and horizontal system transfer functions of the receiver ports. It was also shown that c_1 and c_2 are only a feature of the passive devices in the antenna system and hence are not affected by instability of active components in the radar system. On the other hand, the unbounded transmitted and received waves at the antennas are related by

$$\tilde{\mathbf{E}}^r = \frac{e^{-2ik_0 r}}{r^2} \bar{\bar{\mathbf{S}}}\, \tilde{\mathbf{E}}^t_o \tag{2.12}$$

where r is the range between the radar antenna and the target. By inserting (2.10) and (2.12) into (2.11), we can relate the measured signal $\mathbf{E}^r$ to the bounded wave at the output of the polarizers $\tilde{\mathbf{E}}^t$ by

$$\mathbf{E}^r = \frac{e^{-2ik_0 r}}{r^2} \begin{bmatrix} R_1 & 0 \\ 0 & R_2 \end{bmatrix} \begin{bmatrix} 1 & c_1 \\ c_2 & 1 \end{bmatrix} \begin{bmatrix} S_{vv} & S_{vh} \\ S_{hv} & S_{hh} \end{bmatrix} \begin{bmatrix} 1 & c_3 \\ c_3 & 1 \end{bmatrix} \tilde{\mathbf{E}}^t \tag{2.13}$$

where we have included the transmitter transfer function into the receiver transfer functions, i.e., $R_1 = TR_v$ and $R_2 = TR_h$. Furthermore, let

$$\bar{\bar{\mathbf{R}}}_d = \begin{bmatrix} R_1 & 0 \\ 0 & R_2 \end{bmatrix} \begin{bmatrix} 1 & c_1 \\ c_2 & 1 \end{bmatrix},$$

$$\bar{\bar{\mathbf{T}}}_d = \begin{bmatrix} 1 & c_3 \\ c_3 & 1 \end{bmatrix}. \tag{2.14}$$

The system distortion model for the coherent-on-receive radar shown in Figs. 2.2 and 2.3 can be expressed in matrix format by

$$\mathbf{E}^r = \frac{e^{-2ik_0 r}}{r^2} \; \bar{\bar{\mathbf{R}}}_d \; \bar{\bar{\mathbf{S}}} \; \bar{\bar{\mathbf{T}}}_d \; \tilde{\mathbf{E}}^t \tag{2.15}$$

2.4 Calibration Procedure

So far the system distortions have been modelled mathematically. The next step is to determine the distortion parameters and then, by applying a correction algorithm, calculate the actual Mueller matrix. The standard approach used to find the distortion parameters is to measure a target with a known scattering matrix. A metallic sphere is an excellent candidate for this purpose because its scattering matrix is orientation-independent and its radar cross section is known theoretically. However, as will become apparent later on, the measurements of only a metallic sphere with any combination of transmitted polarizations is not sufficient to determine the seven unknown distortion parameters of the radar system. The measurement of an additional independent depolarizing target is needed in order to determine all distortion parameters. Fortunately, the scattering matrix of the additional target need not be

known. It should be noted that once the distortion parameters are determined carefully using the two calibration targets, a simpler procedure using only a sphere can be used to find the time varient parameters R_1 and R_2 in subsequent calibration of the radar.

The fields, detected at the V-channel of the receiver, that are scattered from a sphere with a radar cross section $\sigma = 4\pi \mid S^\circ \mid^2$ due to vertical, 45-linear, right-hand circular, and left-hand circular polarizations can be expressed in terms of the distortion parameters as follows

$$\begin{aligned} E_v^{oV} &= R_1 S^o (1 + c_1 c_3) \\ E_v^{oLHC} &= \frac{R_1 S^o}{2} [(1 + c_1 c_3)(1 + \tau_1) + (c_1 + c_3)(1 - \tau_1)] \\ E_v^{oRHC} &= \frac{R_1 S^o}{2} [(1 + c_1 c_3)(1 + \tau_1) - (c_1 + c_3)(1 - \tau_1)] \\ E_v^{o45^o} &= \frac{R_1 S^o}{2} [(1 + c_1 c_3)(1 + \tau_2) + \tau_1 (1 - \tau_2)(c_1 + c_3)] \end{aligned} \tag{2.16}$$

Here, the quantities on the left-hand side are the components of the received signal modified by $r_o^2 e^{2ik_0 r_o}$ and the first superscript denotes the sphere and the second one denotes the polarization of the transmitted wave. Solving (2.16) simultaneously provides the following expressions for the distortion parameters τ_1 and τ_2

$$\begin{aligned} \tau_1 &= A_v + B_v - 1 \\ \tau_2 &= 2\frac{(A_v - 1) + (2 - A_v - B_v)\ D_v + \frac{B_v^2 - A_v^2}{2}}{(1 - A_v^2) + (1 - B_v)^2} \end{aligned}$$

where

$$A_v = \frac{E_v^{oLHC}}{E_v^{oV}}, \qquad B_v = \frac{E_v^{oRHC}}{E_v^{oV}}$$

$$D_v = \frac{E_v^{o45}}{E_v^{oV}}. \tag{2.17}$$

The field $\tilde{\mathbf{E}}^t$ can now be determined from (2.9) for any given rotational angles α_1 and α_2 of the dielectric cards. The system distortion model given by (2.15) can be cast into a matrix equation by juxtaposing the measured responses due to two transmitted polarizations; for example for the transmit V and 45^o linear polarizations,

$$\bar{\bar{\mathbf{E}}}^r = \frac{e^{-2ik_0 r}}{r^2} \bar{\bar{\mathbf{R}}}_d \ \bar{\bar{\mathbf{S}}} \ \bar{\bar{\mathbf{T}}}_d \ \bar{\bar{\mathbf{E}}}^t \tag{2.18}$$

where $\bar{\bar{\mathbf{E}}}^t = \left[\tilde{\mathbf{E}}^{tV}, \tilde{\mathbf{E}}^{t45}\right]$ and $\bar{\bar{\mathbf{E}}}^r = \left[\mathbf{E}^{rV}, \mathbf{E}^{r45}\right]$. Noting that the scattering matrix of the sphere is diagonal, the following equation can be obtained from (2.18)

$$\bar{\bar{\mathbf{A}}} = \bar{\bar{\mathbf{E}}}^{r\,o} \ \left(\bar{\bar{\mathbf{E}}}^t\right)^{-1} = \frac{e^{-2ik_0 r_o}}{r_o^2} \ S^o \ \bar{\bar{\mathbf{R}}}_d \ \bar{\bar{\mathbf{T}}}_d \tag{2.19}$$

where $\bar{\bar{\mathbf{E}}}^{r\,o}$ is the matrix of the measured response of the sphere for two transmitted polarizations. Equation (2.19) shows that the sphere measurements can provide at most four independent equations. Since there are five unknowns in $\bar{\bar{\mathbf{R}}}_d$ and $\bar{\bar{\mathbf{T}}}_d$ matrices (R_1, R_2, c_1, c_2, and c_3), an additional independent equation is needed. This can be accomplished by measuring any depolarizing target for any two transmit polarizations and then enforcing the reciprocity theorem.

If $\bar{\bar{\mathbf{E}}}^{r\,d}$ represents the matrix of the measured response of the depolarizing target for two given transmit polarizations, using (2.18) and defining $\bar{\bar{\mathbf{B}}} = \bar{\bar{\mathbf{E}}}^{r\,d} \ \left(\bar{\bar{\mathbf{E}}}^t\right)^{-1}$, the scattering matrix of the depolarizing target can be obtained from

$$\bar{\bar{\mathbf{S}}}^d = r_d^2 \ e^{2ik_o r_d} \ \bar{\bar{\mathbf{R}}}_d^{-1} \ \bar{\bar{\mathbf{B}}} \ \bar{\bar{\mathbf{T}}}_d^{-1} \tag{2.20}$$

Obtaining $\bar{\bar{\mathbf{R}}}_d^{-1}$ from (2.19) and substituting in (2.20), the scattering matrix of the depolarizing target can be expressed by

$$\bar{\bar{\mathbf{S}}}^d = \frac{r_d^2}{r_o^2}\ e^{2ik_o(r_d-r_o)}\ S^o\ \bar{\bar{\mathbf{T}}}_d\ \bar{\bar{\mathbf{A}}}^{-1}\ \bar{\bar{\mathbf{B}}}\ \bar{\bar{\mathbf{T}}}_d^{-1} \tag{2.21}$$

which is only a function of c_3. Enforcing the reciprocity condition ($S_{vh}^d = S_{hv}^d$), the following quadratic equation for c_3 can be obtained

$$c_3^2 + 2\frac{\Omega_1}{\Omega_o}c_3 + 1 = 0 \tag{2.22}$$

where

$$\begin{aligned}
\Omega_o &= a_{21}b_{11} - a_{11}b_{21} + a_{22}b_{12} - a_{12}b_{22} \\
\Omega_1 &= a_{12}b_{21} - a_{22}b_{11} - a_{21}b_{12} + a_{11}b_{22}
\end{aligned}$$

Parameters a_{ij} and b_{ij} ($i,j = 1,2$) are the elements of $\bar{\bar{\mathbf{A}}}$ and $\bar{\bar{\mathbf{B}}}$ matrices respectively. The acceptable root of (2.22) is the one that satisfies the condition $|c_3| < 1$. The only restriction on choosing the depolarizing target is that its scattering matrix must have non-zero eigenvalues; otherwise c_3 cannot be computed from (2.22). Once c_3 is found, the other system distortion parameters can be obtained systematically from (2.19) and are given by

$$\begin{aligned}
c_1 &= \frac{c_3(a_{11}/a_{12}) - 1}{c_3 - (a_{11}/a_{12})} \\
c_2 &= \frac{c_3(a_{22}/a_{21}) - 1}{c_3 - (a_{22}/a_{21})} \\
R_1 &= R_1'\ r_o^2\ e^{2ik_o r_o}, \qquad R_1' = \frac{1}{S^o}\frac{a_{12}}{c_1 + c_3}
\end{aligned}$$

$$R_2 = R_2' \, r_o^2 \, e^{2ik_o r_o}, \qquad R_2' = \frac{1}{S^o} \frac{a_{21}}{c_2 + c_3} \tag{2.23}$$

2.4.1 Special Cases

If the transmit antenna cross-talk factor is very small ($c_3 \simeq 0$), the depolarizing target is not required and the distortions can be determined from the sphere alone. The phase-shift factors τ_1 and τ_2 can be determined as before while the other parameters can be determined as follows

$$\begin{aligned} c_1 &= \frac{A_v - B_v}{2 - A_v - B_v} \\ c_2 &= \frac{2 - A_v - B_v}{A_h - B_h} \\ R_1 &= \frac{E_v^{oV}}{S^o}, \qquad R_2 = \frac{E_h^{oV}}{S^o} \cdot \frac{A_h - B_h}{2 - A_v - B_v} \end{aligned}$$

where

$$A_h = \frac{E_h^{oLHC}}{E_h^{oV}}, \qquad B_h = \frac{E_h^{oRHC}}{E_h^{oV}}.$$

If in addition, the receive antenna cross-talk factors are very small, then measurements of A_h and B_h are very noisy and unreliable. In such cases where $c_1 = c_2 \simeq 0$, (2.16) reduces to

$$\begin{cases} E_v^{oV} &= R_1 S^o \\ E_v^{oLHC} &= R_1 S^o \frac{1 + \tau_1}{2} \\ E_h^{oLHC} &= R_2 S^o \frac{1 - \tau_1}{2} \\ E_v^{o45} &= R_1 S^o \frac{1 + \tau_2}{2} \end{cases}$$

These equations can be solved to obtain

$$\begin{aligned}
\tau_1 &= 2\frac{E_v^{oLHC}}{E_v^{oV}} - 1 \\
\tau_2 &= 2\frac{E_v^{o45}}{E_v^{oV}} - 1 \\
R_1 &= \frac{E_v^{oV}}{S^o}, \qquad R_2 = \frac{E_h^{oLHC}}{\left(E_v^{oV} - E_v^{oLHC}\right)} \cdot \frac{E_v^{oV}}{S^o}
\end{aligned}$$

2.4.2 Correction Schemes

Now we are in a position to correct for the distortions in the measurements of an unknown target. For a coherent-on-receive radar, two correction schemes are considered:(1) Coherent, and (2) Incoherent. The Coherent correction scheme can be used whenever the relative distance between the target and the radar remains constant during the measurements as it is usually the case for indoor measurements. In this case, the scattering matrix is determined from the scattered fields when the target is illuminated by two independent polarizations, for example V and 45^o linear. The incoherent correction scheme must be used whenever the relative distance between the target and the radar changes during the measurements (unstable platform or moving target) as it is usually the case for outdoor measurements. In this case, the received stokes vectors for at least four different transmitted polarizations are used to construct the modified Mueller matrix directly, as was discussed in section 2.2.

In the coherent correction scheme the scattering matrix of the unknown target can be determined from (2.18) directly

$$\bar{\bar{\mathbf{S}}}^u = r_u^2 \; e^{2ik_o r_u} \; \bar{\bar{\mathbf{R}}}_d^{-1} \; \bar{\bar{\mathbf{U}}} \; \bar{\bar{\mathbf{T}}}_d^{-1} \tag{2.24}$$

where $\bar{\bar{\mathbf{U}}} = \bar{\bar{\mathbf{E}}}^{r\,u}.(\bar{\bar{\mathbf{E}}}^t)^{-1}$, and $\bar{\bar{\mathbf{E}}}^{r\,u} = \left[\mathbf{E}_u^{rV}, \mathbf{E}_u^{r45}\right]$ is the measured target response and

r_u is the range to the unknown target.

In the incoherent correction scheme the unbounded transmitted wave, $\tilde{\mathbf{E}}_o^t$, can be determined from (2.8) and (2.10) for any prescribed rotation angles α_1 and α_2 of the dielectric cards. Furthermore, the unbounded received wave, $\tilde{\mathbf{E}}^r$, can be obtained from the measured field $\mathbf{E}^r$ and is given by

$$\tilde{\mathbf{E}}^r = r_u^2 \; e^{2ik_o r_u} \; \bar{\bar{\mathbf{R}}}_d^{-1} \; \mathbf{E}^r \tag{2.25}$$

The transmitted and received Stokes vectors, needed to compute the modified Mueller matrix, can be determined by substituting $\tilde{\mathbf{E}}_o^t$ and $\tilde{\mathbf{E}}^r$, respectively, into the definition of the Stokes vector given by (2.2).

2.5 Comparison With Measured Data

The validity of the new calibration technique is examined by measuring the scattering matrices of cylinders and spheres as test targets using a coherent-on-receive network analyzer-based scatterometer operating at 34.5 GHz. A block diagram of the system is shown in Fig. 2.2. For each transmitted polarization, the network analyzer sweeps over a bandwidth of 1 GHz in 401 steps and collects simultaneously the received fields at the V and H channels. Using the time domain capability of the network analyzer, the target return can then be separated from the unwanted short-range returns and nearby objects. The received signal at the target range includes the target response in addition to disturbances due to the thermal and background noises. The effects of the thermal noise, which is a zero-mean random process, can be minimized by averaging over many samples and the effects of the background, which is due to returns adjacent to the target can be eliminated by subtracting the

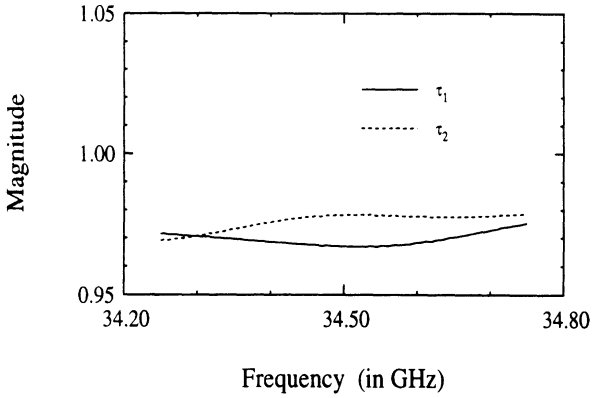

(a)

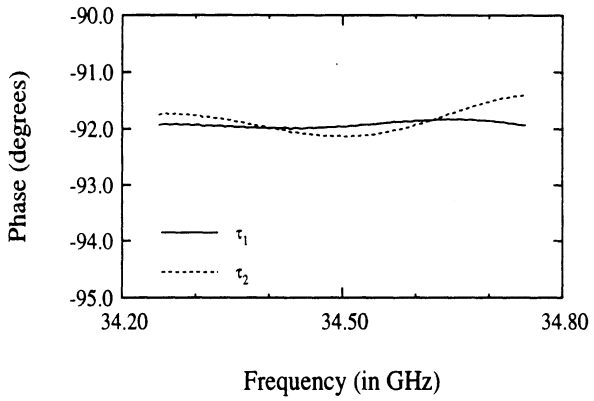

(b)

Figure 2.5: The measured variations of the magnitude (a) and phase (b) of the phase-shift factors, τ_1 and τ_2 , as function of frequency.

background response (in the absence of the target) from the response of the target and background.

Target orientation was facilitated by an elevation over azimuth stepper motor positioner. An 8.1 cm sphere and a finite array of parallel wires were used as the calibration targets. The test targets include a 4.45 cm sphere and a conducting cylinder with a diameter of 0.552 cm and a length of 6.045 cm. The cylinder is measured for two different orientations: vertical and 45° in a plane normal to the direction of incidence. The measured scattering matrices using (2.24) are compared with those computed using the exact eigenfunction expansion solution and the method of moments in conjunction with the Fourier transform technique (body of revolution) for the sphere and cylinders, respectively.

Using averaging and background subtraction, a signal-to-noise ratio of better than 65 dB was achieved. For targets with $S_{vh} = S_{hv} = 0$ (sphere and vertical cylinder), the signal-to-noise ratio in the cross-polarized channels was better than 40 dB.

Applying the calibration technique, the magnitude and phase of the phase-shift factors of the two polarizers, τ_1 and τ_2 are measured and shown in Fig. 2.5 as a function of frequency. As expected, both polarizers exhibit negligible transmission losses as the magnitudes of the transmission coefficients vary between 0.968 and 0.98 over the measured bandwidth. The phases of τ_1 and τ_2 are measured to be around -92^o, which is very close to the expected phase shift of -90.0^o. The measured antennas cross-talk factors of the system as computed by (2.22) and (2.23) are shown in Fig. 2.6.

Fig. 2.7 compares the theoretical and measured scattering matrix elements of the 4.45 cm sphere. The error in the magnitudes of co-polarized terms is less than 0.5 dB and the error in the phase-difference between the co-polarized terms is less

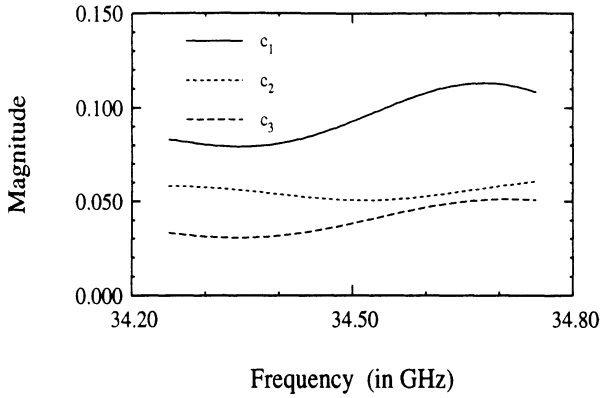

(a)

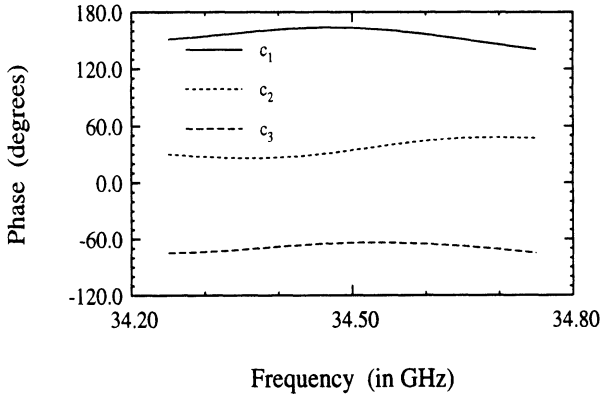

(b)

Figure 2.6: The measured variations of the magnitude (a) and phase (b) of the antenna cross-talk factors c_1, c_2, and c_3 as function of frequency.

than 4°. The cross-polarized term is shown in Fig. 2.7a and shows that an effective cross-polarization isolation of at least -40 dB is obtained which represents a 20 dB improvement in the system cross-polarization isolation.

Excellent agreement is also achieved between the theoretical and measured scattering matrix elements of the cylinder oriented at vertical and 45°. The comparisons are shown in Figs. 2.8 and 2.9 which show a maximum discrepancy of about 0.4 dB in magnitude and 4° in phase. In Figs. 2.8a and 2.9a, the values of σ_{vv} and σ_{hh} are overlapped. The experiments were repeated many times and consistant results were achieved.

2.6 Conclusions

Practical aspects of a calibration procedure for a coherent-on-receive polarimetric radar system are discussed. The polarization state of the transmitter is related to the transmit antenna cross-talk factor and the phase-shift factors of the waveguide polarizers in the radar system. Distortions in the receiver, such as channel imbalances and cross-talk factors, together with the transmitter distortion parameters are obtained from measurements of a metallic sphere and a depolarizing target with unknown scattering matrix for four and two transmit polarizations respectively. The validity and accuracy of the calibration technique is verified by measuring the scattering matrix of independent point targets with known scattering matrices.

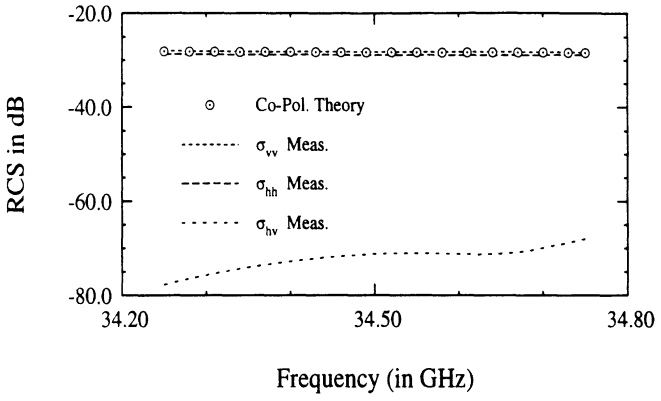

(a)

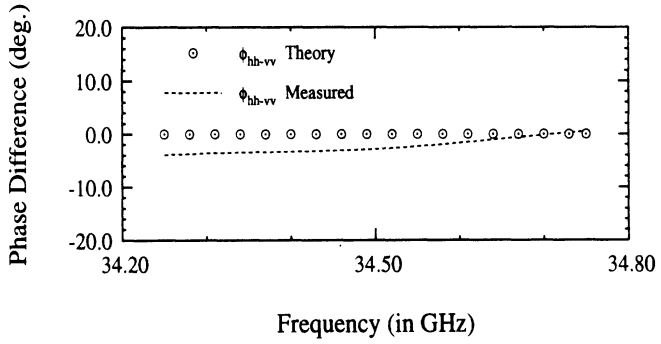

(b)

Figure 2.7: The magnitude (a) and phase-difference (b) of the scattering matrix elements of a 4.45 cm sphere.

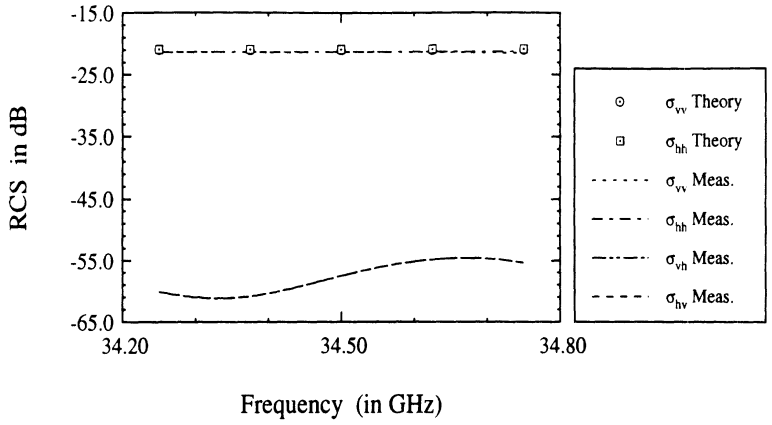

(a)

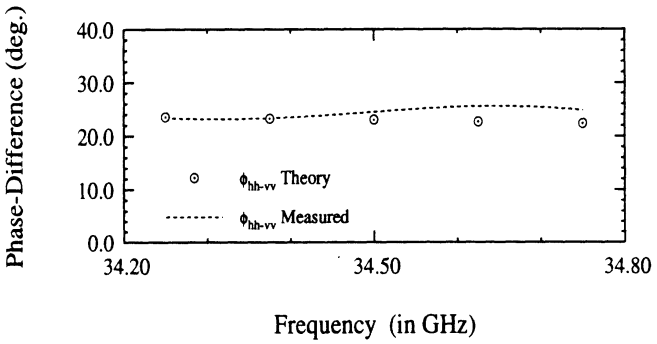

(b)

Figure 2.8: The magnitude (a) and phase-difference (b) of the scattering matrix elements of a vertical cylinder.

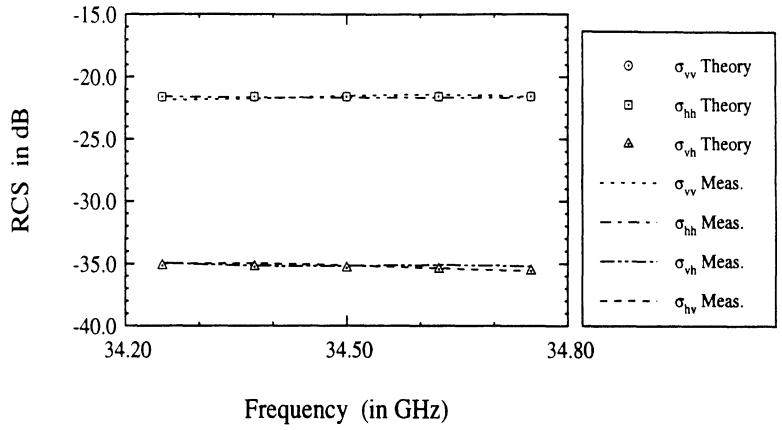

(a)

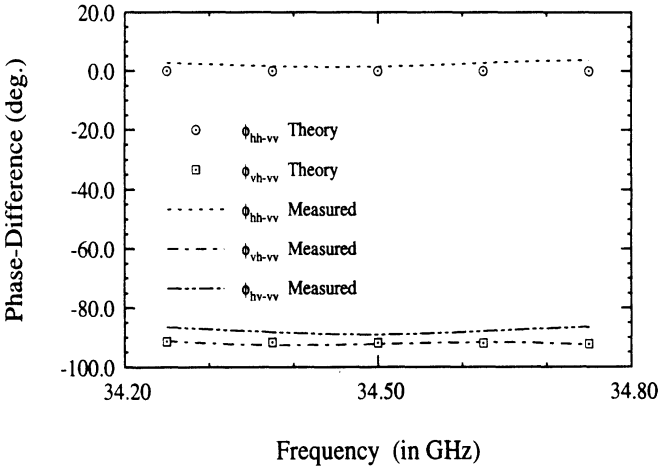

(b)

Figure 2.9: The magnitude (a) and phase-difference (b) of the scattering matrix elements of a cylinder oriented at 45° from vertical.

CHAPTER III

POLARIMETRIC RADAR MEASUREMENTS OF BARE SOIL SURFACES AT MILLIMETER-WAVES: A SEMI- EMPIRICAL MODEL

3.1 Introduction

The millimeter-wave (MMW) backscatter response of bare-soil was examined by conducting experimental measurements at 35 and 94 GHz using a truck-mounted polarimetric scatterometer and by developing appropriate models to relate the backscattering coefficient to the soil's surface and volume properties. The experimental measurements were conducted for three soil surfaces with different roughnesses under both dry and wet conditions. The experimental measurements indicate that in general the backscattering coefficient is comprised of a surface scattering component σ^s and a volume scattering component σ^v. For wet soil conditions, the backscatter is dominated by surface scattering, while for dry conditions both surface and volume scattering are significant, particularly at 94 GHz. Because theoretical surface scattering models were found incapable of predicting the measured backscatter, a semi-empirical surface

scattering model was developed that relates the surface scattering component of the total backscatter to the roughness parameter ks, where $k = 2\pi/\lambda$ and s is the rms height, and the dielectric constant of the soil surface.

An extensive experimental investigation was conducted over the past Five years to examine the polarimetric backscatter behavior of bare soil surfaces in the 1-10 GHz frequency range [33]. Using a set of truck mounted coherent polarimetric scatterometers with center frequencies at 1.25, 4.75 and 9.5 GHz, measurements were made of the Mueller matrix as a function of incidence angle for soil faces covering wide ranges of surface roughness and moisture content. Using the relations outlined in [33] and [34], the measured Mueller matrices were then used to compute the co-polarized backscattering coefficients σ^o_{vv} and σ^o_{hh}, the cross-polarized backscattering coefficient σ^o_{hv}, and the probability density functions of the co-polarized and cross-polarized phase differences. Comparison of the measured data with calculations based on the physical optics model, the geometric optics model, and the small perturbation method revealed that all three models are incapable of correctly predicting the backscatter response of random rough surfaces, even when applied within their presumed ranges of validity. This realization led Oh *et al.* [33] to develop a semi-empirical model that relates σ^o_{ij}, for $i, j = h \, or \, v$, to the incidence angle θ and the surface parameters ks and ϵ_r, where $k = 2\pi/\lambda$, s is the rms height and ϵ_r is the complex relative dielectric constant. The semi-empirical model, which was developed on the basis of measurements made during one season of experimental observations, was found to provide excellent agreement with observations made during two succeeding years for different sets of soil surfaces and conditions.

The work presented in this chapter and in the next chapter extends the preceding work by examining the backscatter response of soil surfaces at millimeter wavelengths

(MMW), specifically 35 and 94 GHz. One of the major lessons learned from the present study is that at centimeter wavelengths it is reasonable to assume that the backscatter from a half-space soil medium is due to scatter by the soil surface alone, but at millimeter wavelengths the backscatter may consist of both surface and volume scattering contributions. Furthermore, for dry soils the volume-scattering component may be comparable to or greater than the surface-scattering component, but for wet soil the volume scattering component becomes negligibly small in comparison with the surface-scattering component. This behavior is consistent with calculations based on radiative transfer theory.

The next section contains detailed descriptions of the 35 and 94 GHz radar systems, the measurement procedure, and the measured properties of the soil surfaces. Section 3.3 provides an overview of the observed angular variation of σ^o for various surface roughnesses and compares the measured response for wet soil surfaces with predictions by classical surface scattering models. A semi-empirical surface scattering model is introduced in Section 3.4 that provides a better fit to the data than the expression previously derived by Oh *et al.* [33] for surface scattering at centimeter wavelengths. Then, the semi-empirical model is compared to experimental observations reported by Yamasaki *et al.* [73] for wet soil surfaces at 60 GHz.

3.2 Experimental Setup

The first part of this section provides a brief description of the polarimetric scatterometers used in support of the present study. It is then followed with discussions of the techniques employed in preparing the surfaces and the methods used in characterizing the physical properties of the observed surfaces.

3.2.1 Polarimetric Scatterometer System

The University of Michigan's Millimeter-wave polarimetric scatterometer system is designed with the capability of measuring directly the Mueller matrix of distributed targets at 35 and 94 GHz. The coherent-on-receive measurement technique described in Section 2.2 is used to measure the Mueller matrix. The scatterometer consists of a computer, an automatic vector network analyzer (HP 8753C), polarization control circuitry, IF switch box, and 35 and 94 GHz front end RF circuitry as shown in Fig. 3.1. A block diagram of the 35 GHz front end RF circuitry is shown in Fig. 2.2. Each radar enjoys a 1 GHz bandwidth (corresponds to 15 cm range resolution). The effective beam widths of the 35 GHz and 94 GHz antenna systems are 3^o and 1.5^o respectively. This corresponds to a spot size of 0.6 m at 35 GHz and 0.3 m at 94 GHz at a range of 10 m. The computer is used to control the network analyzer to insure automatic data acquisition. The computer also controls the IF switch box and the polarization control circuitry to select the desired frequency and polarization configuration.

To allow for an easy access of the soil surfaces, the polarimetric scatterometer systems were mounted on a truck (see Fig. 3.2). In this configuration, the system operates from a variable-angle mount on the end of an extendable boom mounted on the truck. The front end RF components, the IF switch box, and the network analyzer were all mounted on the boom top while the computer and polarization control circuitry were mounted in a control house on the bed of the truck. In this setup, the network analyzer is connected to the radars *via* short IF cables as opposed to the long IF cables normally required in the conventional setup of mounting the network analyzer along with the computer and other equipment in the control house.

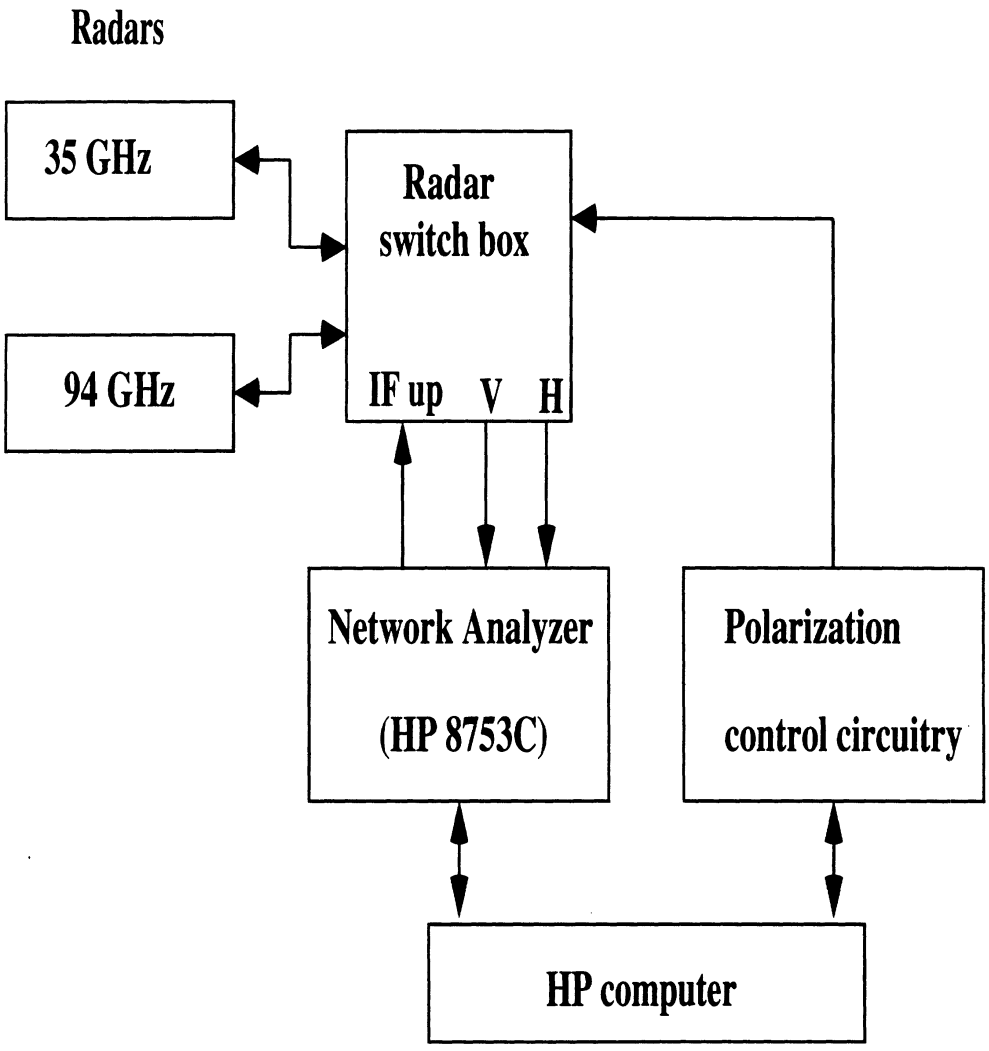

Figure 3.1: System block diagram of the MMW polarimetric scatterometer.

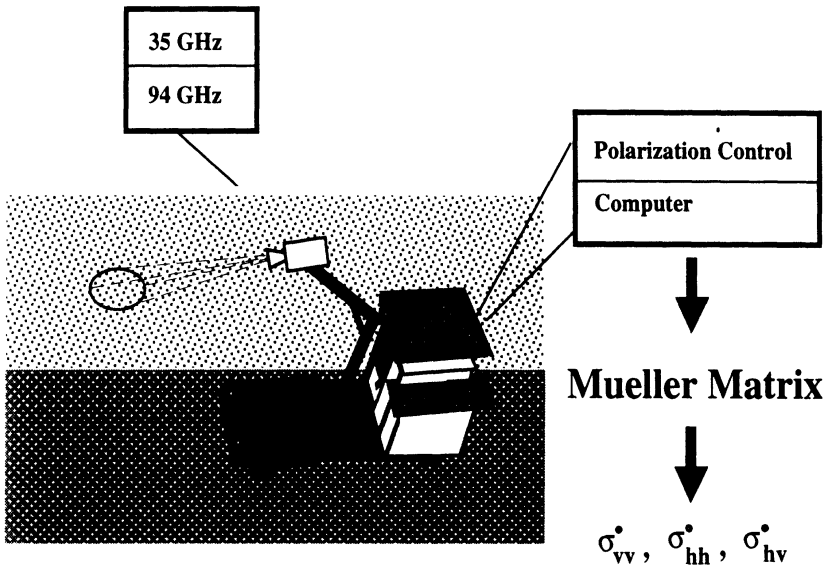

Surfaces :

S1 (s = 0.66 mm.)
S2 (s = 2.62 mm.)
S3 (s = 7.77 mm.)

Figure 3.2: Experimental setup with MMW polarimetric scatterometer mounted on the boom of a truck.

3.2.2 Measurement Procedure

Backscatter measurements of each soil surface were performed at three incidence angles (20^o, 45^o, and 70^o) during which the distance to the soil surface was kept constant at 10 m. Measurement sessions started by pointing the scatterometer system towards the target at the appropriate range and incidence angle. While the boom was not moving, the computer first selected the 35 GHz radar to measure the backscattering response for six different sequentially transmitted polarizations (V, H, 45L, 135L, LHC, and RHC). The measurement was then repeated for the 94 GHz radar. The process was repeated after the scatterometer system was moved to a new spot by rotating the boom around its axis. Overall, 60 independent spatial samples were collected for each surface.

Raw data was saved on the computer hard disk in binary format to reduce the data acquisition time. To process the data, the raw traces were sent back to the network analyzer where the signal of the desired target was isolated from signals of other (unwanted) targets using the gating capabilities of the network analyzer. Once the gated data was calibrated and the received Stokes vectors were computed and averaged over all spatial samples, the Mueller matrix was computed using the procedure described in Section 2.2.

Additional independent samples were obtained by performing frequency averaging over the 1 GHz bandwidth. Overall, between 120 samples at $\theta = 20^o$ and 240 samples at $\theta = 70^o$ were collected for each target.

3.2.3 Surface Preparation

The wavelengths corresponding to 35 and 94 GHz are 8.6 mm and 3.2 mm, respectively. Special care was taken in preparing the three soil surfaces in order to insure that the backscattering measurements cover a wide range of surface roughness relative to λ and to replicate a wide range of naturally occurring surface conditions. Initially, all surfaces were cleared from grass and vegetation debris. Then, in order to have a "smooth" surface with rms height less than 1 mm, a heavy roller was moved across surface S1. This technique resulted in a compacted soil medium with an rms height $s = 0.66$ mm. Surface S1 resembles a packed-down dirt road surface. For surface S3, the top layer was turned over by a hand shovel resulting in an undulating surface with $s = 7.77$ mm, and the surface represented a freshly plowed soil surface. Surface S2 was a slightly rough surface with $s = 2.62$ mm and it represented what surface S3 would look like after cultivation by a farm implement to break down the large soil clods or after natural smoothing action by rain and wind. Surface height characterization was performed by a laser profiler, as will be discussed later.

Two sets of measurements were conducted, one for dry soil conditions and the other for wet soil conditions. A tree sprayer with an adjustable nozzle was used to spray a fine mist of water droplets to insure a constant surface wetness during radar measurements while preserving the surface roughness. As an example of the effectiveness of this technique, the gravimetric moisture content collected during measurements of surface S3 under wet conditions is shown in Fig. 3.3 as function of time.

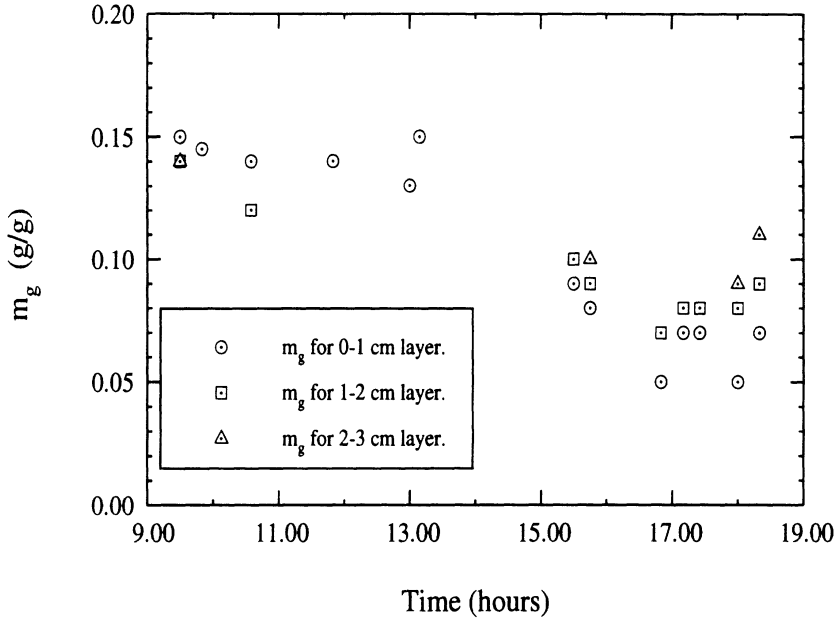

Figure 3.3: The gravimetric moisture content m_g as a function of time for wet surface S3. Spraying the surface with water was stopped once the backscattering measurements were concluded at 14.00 hours.

3.2.4 Surface Characterization

Surface height profiles and soil samples were collected for each soil surface under wet and dry conditions in order to determine the surface height statistics, the bulk soil density and moisture content. In addition, size distributions of the solid soil particles and the air voids were generated.

Surface Height Profiles

The height profile of each soil surface was measured by a laser profiler mounted on an x-y table. The profiler, which is driven by stepper motors, measured 30-cm long linear segments with 0.3 mm horizontal resolution and 0.3 mm vertical resolution. An IBM-PC was used to control the stepper motors and to collect and store the heights measured by the laser profiler. At least five height profiles of different areas were recorded for each surface. Samples of surface profiles of the three surfaces and their auto-correlation functions , each normalized to its maximum value at zero displacement, are shown in Fig. 3.4. The rms height s and correlation length l are listed in Table 3.1 for each of the three surfaces.

surface	$s(mm)$	$l(mm)$	Freq(GHz)	ks	kl
S1	0.66	27	35	0.48	19.8
			94	1.3	53
S2	2.62	30	35	1.92	22
			94	5.16	59
S3	7.77	20	35	5.69	14.7
			94	15.3	39.4

s = rms height
l = correlation length
$k = 2\pi / \lambda$

Table 3.1: Surface roughness statistical parameters for the three soil surfaces.

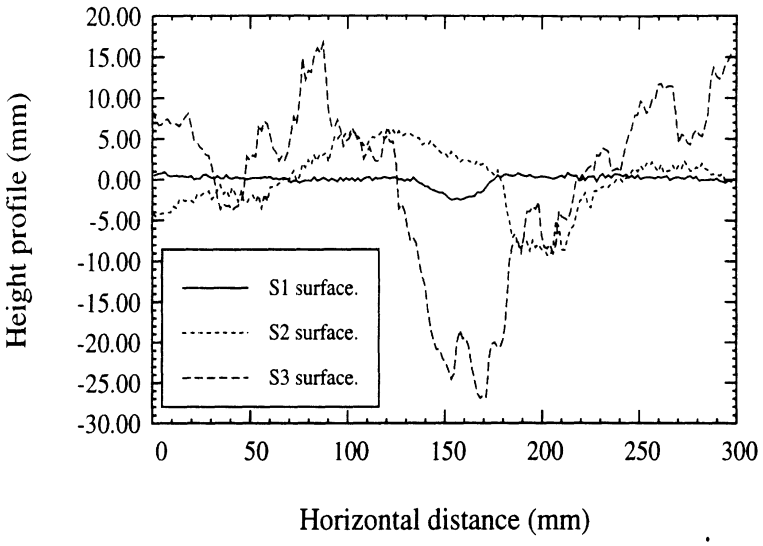

(a)

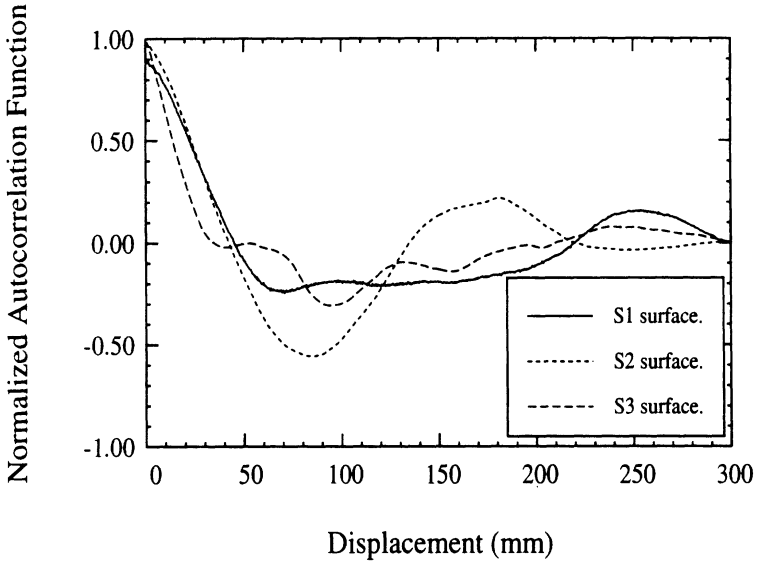

(b)

Figure 3.4: (a) Samples of the Surface height profiles, measured using a laser profiler, and (b) autocorrelation functions of the three surfaces.

Soil Density and Moisture Content

In conjunction with the radar measurements, the soil bulk density ρ_b and the volumetric moisture content m_v were measured by collecting 1-cm thick soil samples for each of the top 3-cm soil layers. The procedure is shown in Fig. 3.5 where a 15×15 cm metallic frame of 1-cm thickness is placed on top of the soil surface and gently forced into the soil with minimal disturbance to the soil medium. The soil within the metallic frame is then removed to a container and immediately weighed *via* a sensitive electronic scale, baked overnight in an oven and weighed once again when dry. The moisture content and the bulk soil density were determined using the following relations:

$$\begin{aligned} m_g &= \frac{(W_{wet} - W_{dry})}{W_{dry}} \\ \rho_b &= \frac{W_{dry}}{V} \\ m_v &= m_g \times V \end{aligned}$$

where W_{wet} is the weight of the soil before baking, W_{dry} is the weight of the soil after baking, m_g is the gravimetric moisture content, and V is the volume of the soil sample ($15 \times 15 \times 1\, cm^3$). The average values of ρ_b and m_v are listed in Table 3.2, for all three surfaces.

Soil Particle Size Distribution

The soil particle size distrib is shown in Fig. 3.6, indicating that the bulk of the soil material consists of s nd (diameter $\geq$ 0.02 mm). To investigate the void size distribution of the soil ...edium, thin soil slices were collected and then photographed by a microscope camera. Two histograms of the void-size distribution

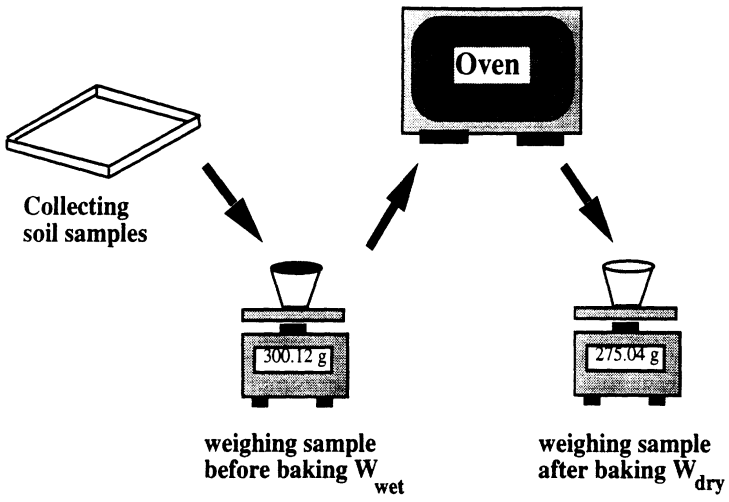

Figure 3.5: The procedure used to collect 1-cm thick soil samples and estimate the gravimetric moisture content.

were generated, one for bulk soil density $\rho_b = 1.69$ g/cm^3 (for soil surface S1) and another for $\rho_b = 1.32$ g/cm^3 (for soil surface S3), by treating the voids as spherical in shape. The mean void diameter was calculated to be 0.165 mm for the high-density soil, compared to 0.242 mm for the low-density soil. The void size distribution of the soil with $\rho_b = 1.69$ g/cm^3 and $\rho_b = 1.32$ g/cm^3 are shown in Fig. 3.7.

In order to compare the radar observations to theoretical models, we need to obtain good estimates of the soil's dielectric constant or relate the dielectric constant to the soil's physical properties. Unfortunately, no theoretical or empirical model is available in the literature that can correctly predict the effective dielectric constant of soils at MMW frequencies. In this thesis, the effective dielectric constant of the soils observed in this study were estimated by applying the semi-empirical formula found in [62], [14]. The results are given in Table 3.2. For the measured dry surfaces with low moisture content, it is difficult to determine accurately the amount of free water. In addition, it was observed that the first few millimeters of the soil medium

					m_v		ϵ_r	
Surface	ρ_b	ν_a	d_p mm	d_v mm	0-1 cm	2-3 cm	35 GHz	94 GHz
S1-dry	1.69	0.36	0.3	0.165	0.02	0.08	(3.1, 0.05)	(3.1, 0.05)
S1-wet	1.69	0.36	0.3	0.165	0.23	0.19	(7.3,4.5)	(5.0,2.4)
S2-dry	1.37	0.45	0.3	0.165	0.04	0.07	(2.5, 0.05)	(2.5, 0.05)
S2-wet	1.37	0.45	0.3	0.165	0.12	0.12	(4.6,2.0)	(3.5,1.1)
S3-dry	1.32	0.50	0.3	0.242	0.04	0.07	(2.5, 0.05)	(2.5, 0.05)
S3-wet	1.32	0.50	0.3	0.242	0.19	0.18	(5.9,3.5)	(4.1,1.9)

ρ_b = soil bulk density (g/cm^3).
ν_a = air-voids volume fraction.
d_p = mean soil particle diameter.
d_v = mean air-void ‹ neter.
m_v = volumetric mo re content.
ϵ_r = effective dielectı constant.

Table 3.2: Summary of soil properties.

were very dry, and the soil wetness increased gradually with depth. The values given in Table 3.2 for the dielectric constants of the dry soil surfaces are for the very top surface layer. The thickness of that dry surface layer plays an important role in determining the relative contribution of volume scattering to the total backscatter, as discussed later in Chapter IV.

3.3 Experimental Observations and Comparison with Classical Models

This section examines the experimental behavior of the backscattering coefficient σ^o as a function of (1) the radar parameters: frequency, receive-transmit polarization configuration, and the incidence angle θ, and (2) the soil surface parameters: the rms surface height s, the surface correlation length l, and moisture content m_v.

In general, two scattering mechanisms contribute to the backscattering coefficient σ^o (Fig. 3.8), a surface scattering contribution σ^s which is a function of the surface

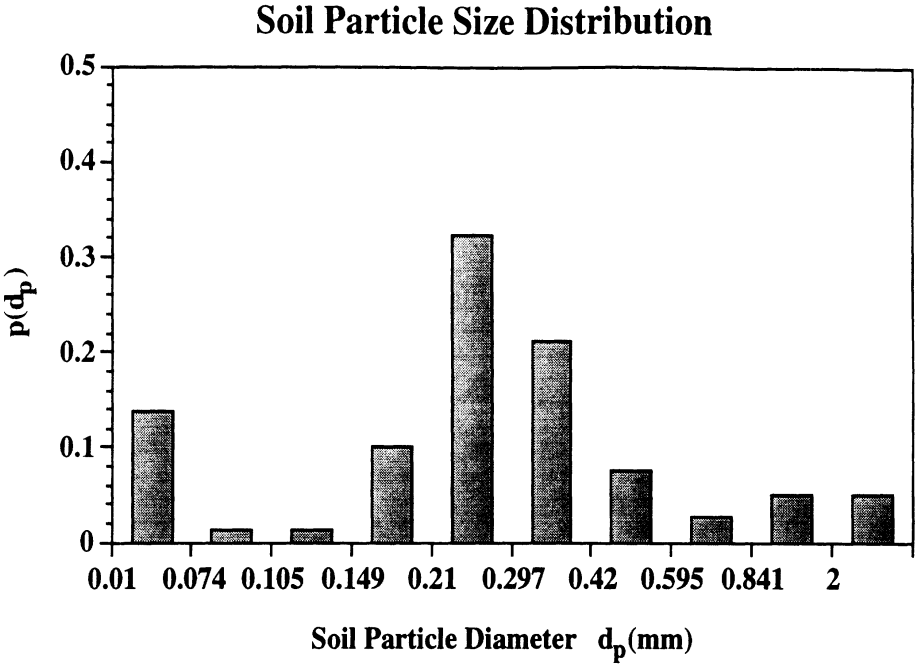

Figure 3.6: Soil particle size distribution $p(d_p)$.

height statistics and ϵ_r of the lower half space, and a volume scattering contribution σ^v that is due to inclusions underneath the rough interface:

$$\sigma^o_{ij} = \sigma^s_{ij} + \sigma^v_{ij} \qquad i,j = h \text{ or } v. \tag{3.1}$$

The volume scattering contribution is in turn governed by the height statistics of the rough interface and the size, shape, and orientation distributions of the inclusions in the soil medium (air voids in this case) and the dielectric constant of the host material (soil particles). Depending on the surface roughness, the density of the volume scatterers, and the dielectric properties of both the scatterers and the background medium one type of scattering can dominate over the other [35]. Calculations based on radiative transfer theory reveal that σ^v is much smaller than the observed scattering coefficient σ^o, and hence much smaller than σ^s, except for dry soil at 94 GHz. This can be explained by noting that at 35 GHz the air voids are very small in size

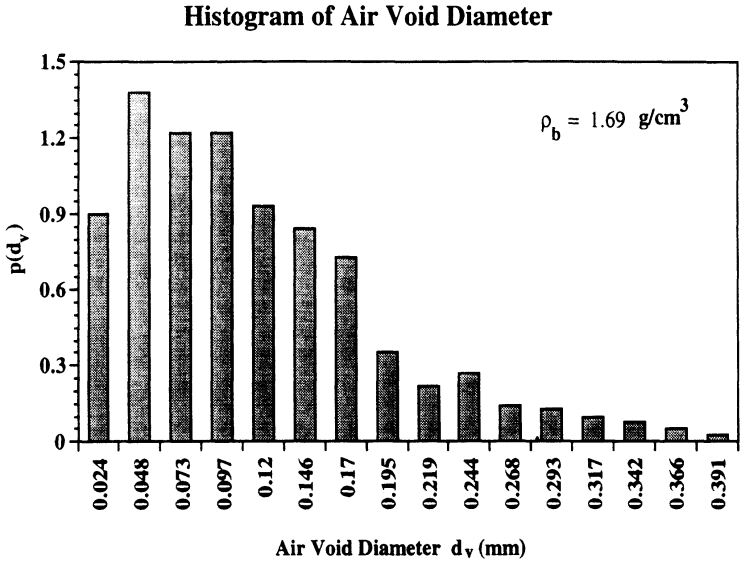

(a)

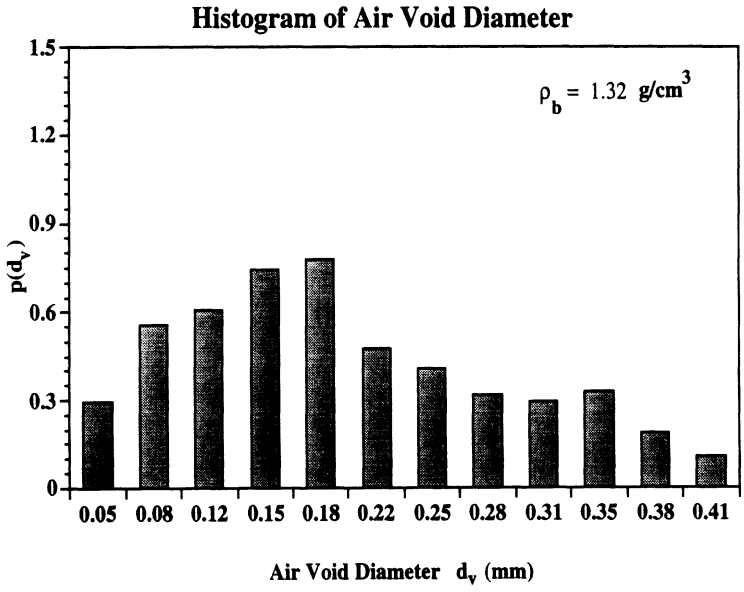

(b)

Figure 3.7: Histogram of the air void-size distribution $p(d_v)$ for the soil with (a) $\rho_b = 1.69$ g/cm^3, and (b) $\rho_b = 1.32$ g/cm^3.

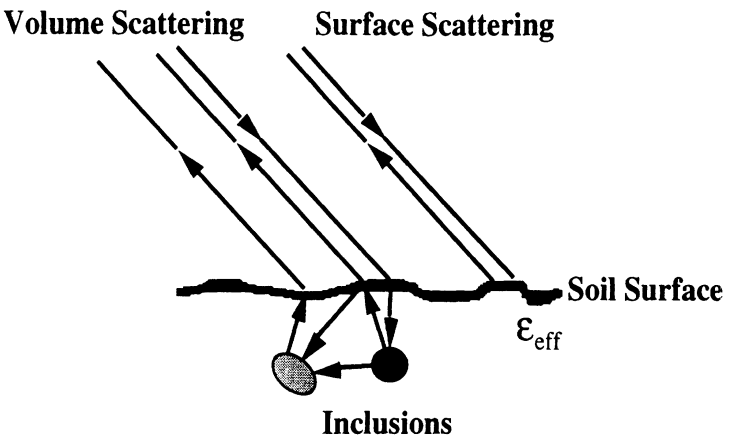

Figure 3.8: Surface and volume-scattering mechanisms contributing to the total backscatter.

(see Fig. 3.7) relative to λ, and at 94 GHz the attenuation in wet soil reduces the penetration depth to a very thin surface layer, thereby reducing the volume scattering contribution to a negligible level. In this chapter, we will limit the analysis to the wet soil cases in order to examine the surface scattering component alone and then in the next chapter we will use radiative transfer theory to model the volume-scattering component. Hence, for the cases presented in this section, $\sigma^o = \sigma^s$.

3.3.1 Experimental Observations

As was stated earlier, the radar observations were made at 35 GHz and 94 GHz for each of three surfaces with widely different roughnesses. Figure 3.9 displays the angular variation of σ^o, for each of the three principal polarization configurations, for the surface with the smallest value of ks (surface S1 with $s = 0.66$ mm, observed at 35 GHz) and the surface with the largest value of ks (surface S3 with $s = 7.77$ mm, observed at 94 GHz). We note that the curves for the co-polarized scattering coefficients, σ^o_{vv} and σ^o_{hh}, diverge as a function of θ for the smooth surface represented

by Fig. 3.9a, but they remain approximately equal for the very rough surface represented by Fig. 3.9b. This behavior is consistent with previous observations made at centimeter wavelengths [33]. We also note that the difference in level between the σ^o_{vv} and σ^o_{hv} curves is at least 18 dB for the smooth surface (actually 21 dB at 20°, decreasing to 18 dB at 70°), whereas the difference never exceeds 13 dB for the very rough surface. These observations clearly indicate that surface roughness exercises a significant influence on both the co-polarized ratio $p = \sigma^s_{hh}/\sigma^s_{vv}$ and the cross-polarized ratio $q = \sigma^s_{hv}/\sigma^s_{vv}$. It should be noted that the continuous curves shown in Fig. 3.9 are based on the semi-empirical expressions which will be introduced in Section 3.4.

3.3.2 Comparison with Classical Surface Scattering Models

In this section, the data measured at 35 and 94 GHz for wet soil surfaces is compared with the classical surface scattering models such as the small perturbation (SPM), the physical optics (PO), and the geometric optics (GO) models. Derivations and explicit expressions for σ^o along with regions of validity for these models can be found in [62], [60]. It should be noted that none of the surfaces examined here fell within the regions of validity of the small perturbation model. Hence, no comparison with this model was conducted.

Being first order scattering models, the PO model and the GO model cannot predict the cross-polarized return in the backscattering direction. Hence, only the co-polarized return is examined here. The surface roughness parameters of surfaces S1 and S2 were found to be within the range of validity of the PO model at both frequencies while the surface roughness parameters of surface S3 were found to be within the range of validity of GO model at both frequencies. Furthermore, surface

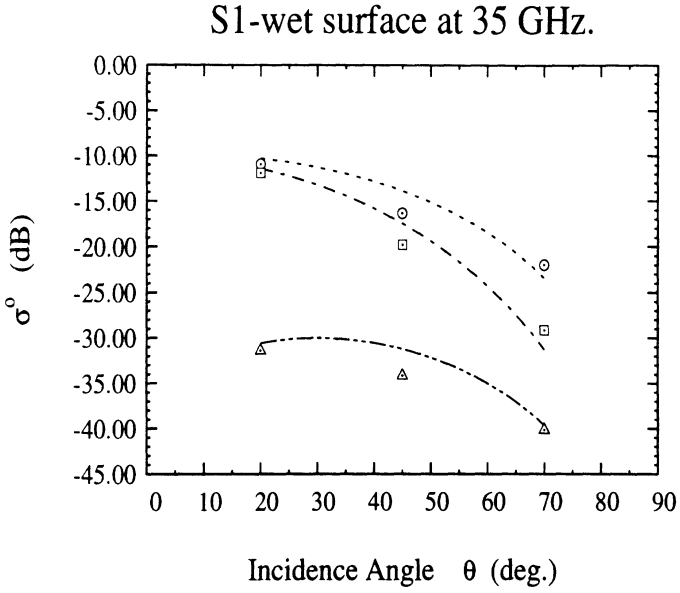

(a)

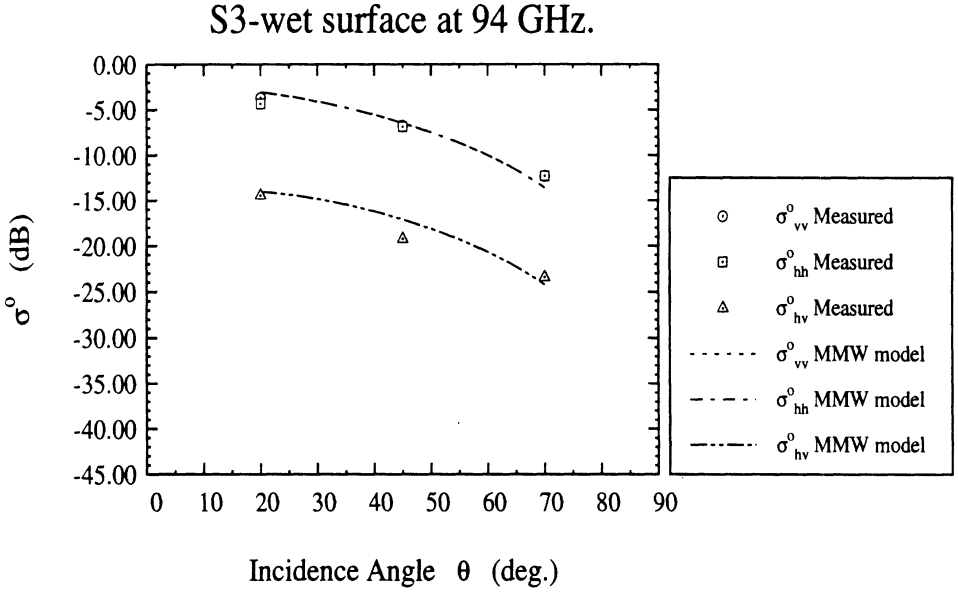

(b)

Figure 3.9: Comparison of the measured backscattering coefficients for wet soil surfaces with calculations based on the semi-empirical surface scattering model given in Section 3.4 for (a) the smoothest surface at 35 GHz ($ks = 0.48$), and (b) the roughest surface at 94 GHz ($ks = 15.3$).

S2 at 94 GHz was found to be within the ranges of validity of both PO and GO models. Comparison between the measured data with values calculated in accordance with PO and GO models reveals poor agreement between the theoretical predictions and the experimental observations, as shown in Fig. 3.10a for the smoothest surface at 35 GHz, whose roughness parameters fall in the validity range of the physical optics model, and in Fig. 3.10b for the other two surfaces at 94 GHz, for which the geometric optics model is supposed to be applicable. It should also be noted that the measured σ^o_{vv} is higher than or equal to σ^o_{hh} in all measurements reported in this chapter, which is contrary to the predictions of the PO model (see Fig. 3.10).

In summary, both GO and PO do not provide good agreement with measured data at millimeter-wave frequencies. Also, they cannot be used for the cross-polarized response. In addition, the PO model predicts that $\sigma^o_{vv} < \sigma^o_{hh}$ contrary to the measured data at both centimeter and millimeter-wave frequencies [33].

3.3.3 Comparison with Microwave Semi-Empirical Surface Scattering Model

In this section, the data measured at 35 and 94 GHz for wet soil surfaces is compared with the semi-empirical surface scattering model developed by Oh *et al.* [33] at centimeter wavelengths. As mentioned earlier, the semi-empirical model was based on data collected at L, C, and X frequency bands as a function of incidence angle for four bare soil surfaces with different roughnesses. This data covered a wide range of surface roughnesses ($0.1 < ks < 6.0$ and $2.6 < kl < 19.7$) and soil moisture content ($0.09 < m_v < 0.31$). However, only a fraction of the data corresponding to incidence angles of $\theta = 30^o, 40^o$, and 50^o was used in the development of this model.

While only two cases are chosen here for detailed comparisons with the L-C-X

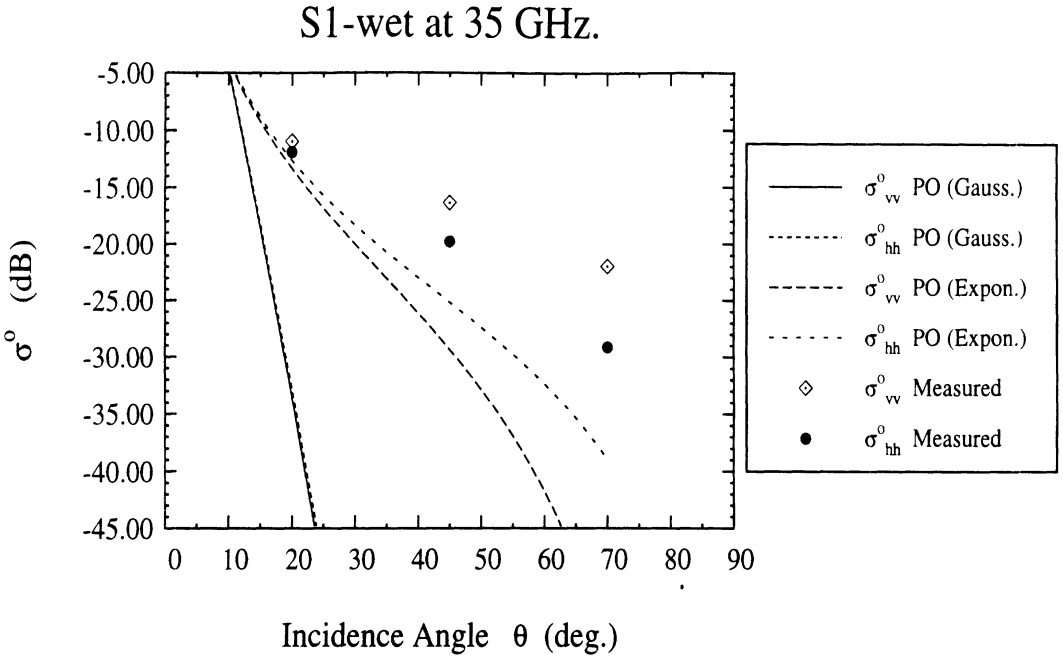

(a)

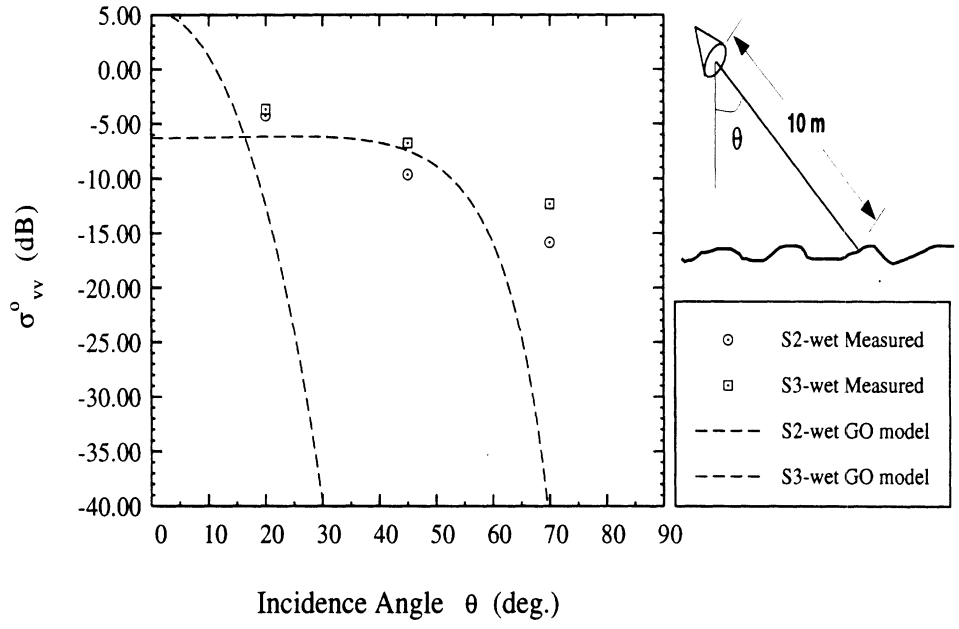

(b)

Figure 3.10: Comparison between (a) measured data for surface S1 and predictions based on the physical optics (PO) model at 35 GHz for both gaussian and exponential surface height autocorrelation functions, and (b) measured data for surfaces S2 and S3 and predictions based on the geometric optics (GO) model at 94 GHz.

empirical model, the conclusions drawn from these comparisons apply to the other measured cases. The first example is surface S1-wet measured at 35 GHz which has its ks, kl, and m_v within the ranges covered by the L-C-X empirical model. For this surface, the L-C-X empirical model predicts well σ^o_{vv} and σ^o_{hh}, however, it overestimates σ^o_{hv}, as shown in Fig. 3.11a. The second example is surface S3-wet measured at 94 GHz which has its ks and kl, outside the ranges covered by the L-C-X empirical model. In this case, the model underestimates the measured data by at least 4 dB for all polarizations, as observed in Fig. 3.11b.

In conclusion, the L-C-X empirical model is not adequate for millimeter-wave frequencies since it does not predict consistently the backscattering response from soil surfaces at these frequencies. This can be attributed to the fact that the model is insensitive to roughnesses, beyond $ks = 3.0$, and that a wider range of incidence angles was not used in constructing the model.

Faced with these inadequacies in both the classical surface scattering models (PO and GO) and the L-C-X emirical model, an improved semi-empirical model is developed in the next section based on measured data at 35 and 94 GHz.

3.4 Semi-Empirical Surface Scattering Model at Millimeter-Wave Frequencies

An examination of Table 3.1 shows that among the three surfaces, the surface correlation length l varies over a narrower range of $1.5:1$ (between a minimum of 2 cm for S3 and a maximum of 3 cm for S2). The corresponding range on the kl scale (where $k = 2\pi/\lambda$), is approximately $4:1$. In contrast, the rms height s varies over a range of $12:1$, and ks covers the range $32:1$. A third surface roughness parameter

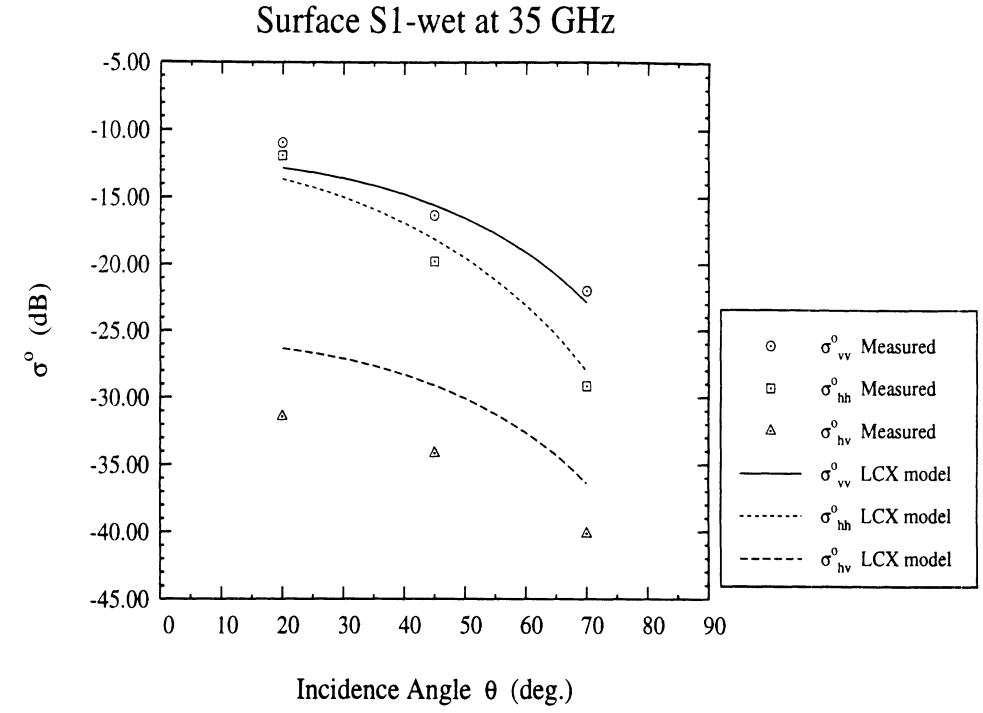

(a)

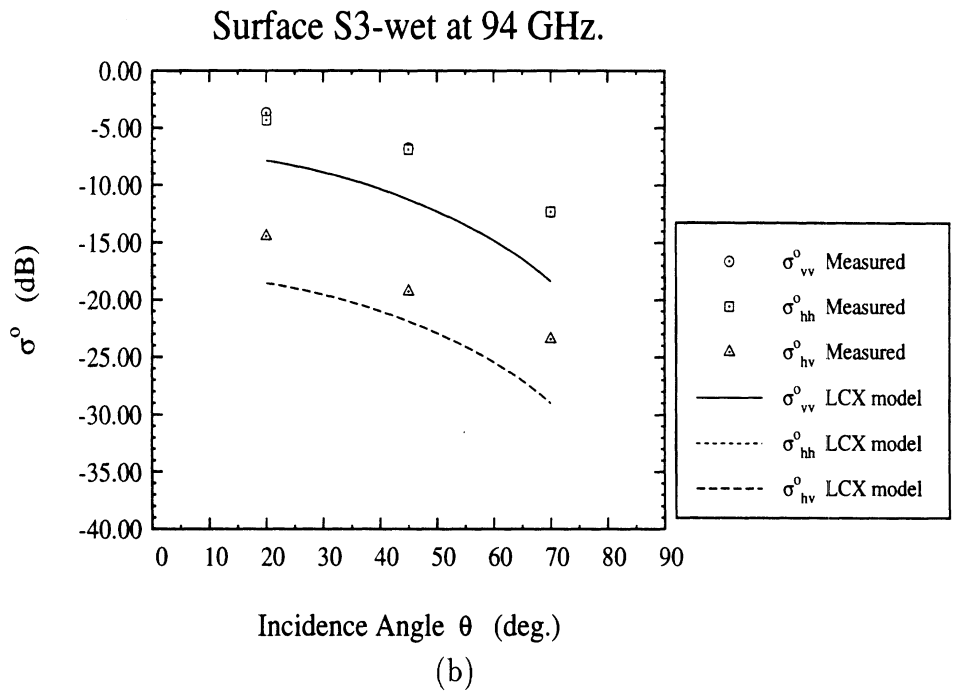

(b)

Figure 3.11: Comparison between the L-C-X semi-empirical surface scattering model and the backscattering response for (a) surface S1-wet measured at 35 GHz, and (b) surface S3-wet measured at 94 GHz.

of interest is the ratio $m = s/l$ which is equal to or proportional to the rms slope of the surface, with the proportionality constant being determined by the form of the surface autocorrelation function. For the three surfaces, m varies from 0.025 for S1 to 0.39 for S2. A detailed analysis was conducted to determine the sensitivities of the backscattering coefficients σ^o_{vv}, σ^o_{hh}, and σ^o_{hv} to s, l, ks, kl, and m. Plots of the backscattering coefficients *versus* the five surface roughness descriptors revealed the following: (a) strong but different dependences on s at 35 GHz and 94 GHz, (b) the individual frequency plots coincide with each other when the data is plotted against ks, (c) random variations with l and kl, and (d) the variation with m is driven by the dependence on s. Considering that l exhibits a relatively narrow range among the three surfaces, it is not surprising that s was found to be the primary parameter governing the dependence of the radar backscatter on surface roughness.

3.4.1 Co-Polarization Ratio

The dependences of the co-polarized and cross-polarized ratios p and q on ks are illustrated in Fig. 3.12. At $\theta = 20^o$, p exhibits no discernible dependence on ks, as expected, because θ is close to normal incidence. At the higher angles of 45° and 70°, p increases with increasing ks until ks reaches a value of 4, beyond which p assumes the constant ratio of 1.0. The continuous curves shown in Fig. 3.12a are based on the following expression:

$$p = \frac{\sigma^s_{hh}}{\sigma^s_{vv}} = \left[1 - \left(\frac{2\theta}{\pi}\right)^{1/(3\Gamma_o)} exp[-0.4ks]\right]^2 \tag{3.2}$$

where θ is the incidence angle in radians and Γ_o is the reflectivity for normal incidence,

$$\Gamma_o = \left| \frac{1 - \sqrt{\epsilon_r}}{1 + \sqrt{\epsilon_r}} \right|^2 \tag{3.3}$$

The form of (3.2), which was adapted from the experience gained previously from the centimeter-wave study [33], includes a dependence on the dielectric constant ϵ_r. The plots shown in Fig. 3.12a correspond to $\epsilon_r = 5.07 + j2.56$, which is in the middle of the range of the dielectric constants corresponding to the wet-soil surfaces observed by the radar (see Table 3.2). Thus, part of the data scatter in Fig. 3.12a is attributed to the non-uniformity of dielectric constants among the data points.

3.4.2 Cross-Polarization Ratio

The cross-polarization ratio q, which exhibits an inverse negative exponential dependence on ks for all angles of incidence (Fig. 3.12b), is modeled by the expression:

$$q = \frac{\sigma^s_{hv}}{\sigma^s_{vv}} = 0.23 \sqrt{\Gamma_o} \; [1 - exp(-0.5 \, sin\theta \, ks)] \tag{3.4}$$

To eliminate the dependence on the dielectric constant ϵ_r, the ratio q shown in Fig. 3.12b has been normalized by dividing it by $\Gamma_o^{1/2}$ for both the data points and the expression given by (3.4).

3.4.3 σ^s_{vv} Response

So far we have characterized the ratios of σ^s_{hh} and σ^s_{hv} with respect to σ^s_{vv} through (3.2) and (3.4). Now, we turn our attention to the response of σ^s_{vv} to θ, ks and ϵ_r.

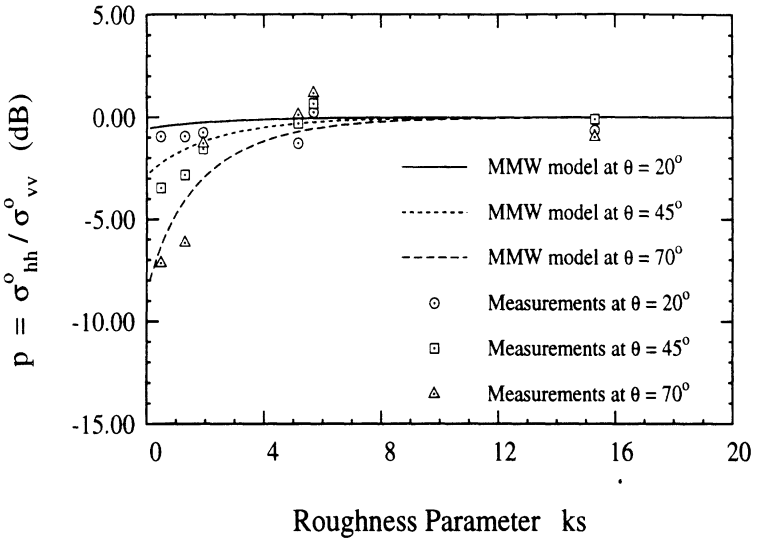

(a)

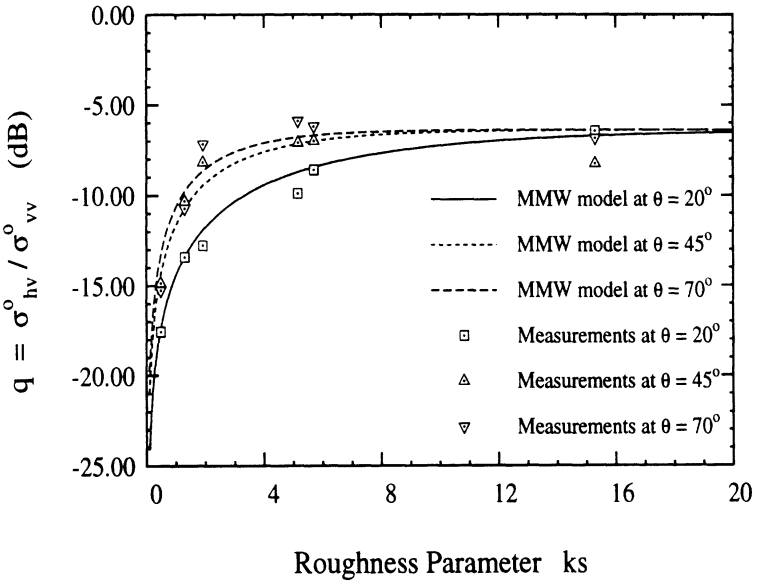

(b)

Figure 3.12: Measured sensitivity of (a) the co-polarized ratio p, and (b) the cross-polarized ratio q to surface roughness for wet soil surfaces at various incidence angles. The continuous curves are based on the expressions given in Section 3.4.

The proposed functional form is:

$$\sigma^s_{vv} = g \, \frac{cos^x\theta}{\sqrt{p}} \, [\Gamma_v(\theta) + \Gamma_h(\theta)] \tag{3.5}$$

where p is given by (3.2), $\Gamma_v(\theta)$ and $\Gamma_h(\theta)$ are the Fresnel reflectivities at incidence angle θ for v and h polarizations, respectively, and the function g is given by:

$$g = 2.2 \, (1 - exp[-0.2ks]) \tag{3.6}$$

The exponent of the $\cos\theta$ term in (3.5) accounts for the change in the angular dependency of σ^s_{vv} as a function of ks, and is given by:

$$x = 3.5 + \frac{1}{\pi} \, tan^{-1}[10 \, (1.65 - ks)] \tag{3.7}$$

For a very rough surface with ks very large, $p \approx 1$, $g \approx 2.2$, and $x \approx 3$, in which case (3.5) reduces to:

$$\sigma^s_{vv} = 2.2 \, \cos^3\theta \, [\Gamma_v(\theta) + \Gamma_h(\theta)] \, , \qquad for \quad ks >> 1 \tag{3.8}$$

The inclusion of the sum $[\Gamma_v(\theta) + \Gamma_h(\theta)]$ in the expression for σ^s_{vv} simply insures that for a very rough surface, $\sigma^s_{vv} = \sigma^s_{hh}$, and yet the magnitudes of these two co-polarized coefficients are somehow related to the angle-dependent reflectivity of the surface.

To compare the proposed model with the experimental data (Fig. 3.13) we first normalized the measured values of σ^s_{vv} by dividing each by the sum of the reflectivities corresponding to the dielectric values associated with the surface and incidence angle

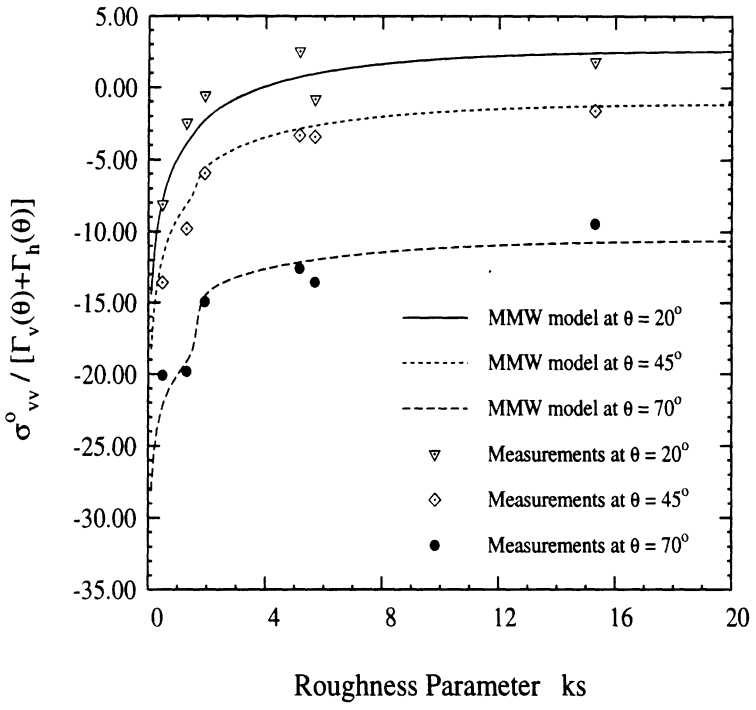

Figure 3.13: The sensitivity of σ^o_{vv} to surface roughness for wet soils at various incidence angles.

and then plotted the results as a function of ks. The same normalization procedure was applied to (3.5) prior to plotting it in Fig. 3.13. In fact, the values of the coefficients appearing in (3.6) and (3.7) were selected by matching the expression given by (3.5) to the data.

3.4.4 Comparison of Model with Observations

The expressions given by (3.2)-(3.7) represent a semi-empirical model for characterizing the surface-scattering component of millimeter-wave backscattering from a random rough surface. The continuous curves shown in Fig. 3.9 are based on this model as are the curves shown in Fig. 3.14 for surface S2 (with intermediate roughness) and in Fig. 3.15 where the model is compared with an independent data set (not used in constructing the surface model) reported by Yamasaki, *et al.* [73] at 60 GHz, also for wet-soil surfaces.

3.5 Conclusions

The backscattering coefficients of three soil surfaces were measured as a function of incidence angle using two scatterometers operating at 35 GHz and 94 GHz. The soil surfaces, with roughnesses ranging between $ks = 0.48$ and $ks = 15.3$, were measured under wet and dry conditions. When compared to measurements, the physical optics and geometric optics surface-scattering models, as well as the empirical surface-scattering model given in [33], failed to consistently predict the measured backscattering coefficients.

Analysis of the measured radar data indicates that in general both surface and volume scattering contributions are present at MMW frequencies. For wet soil condi-

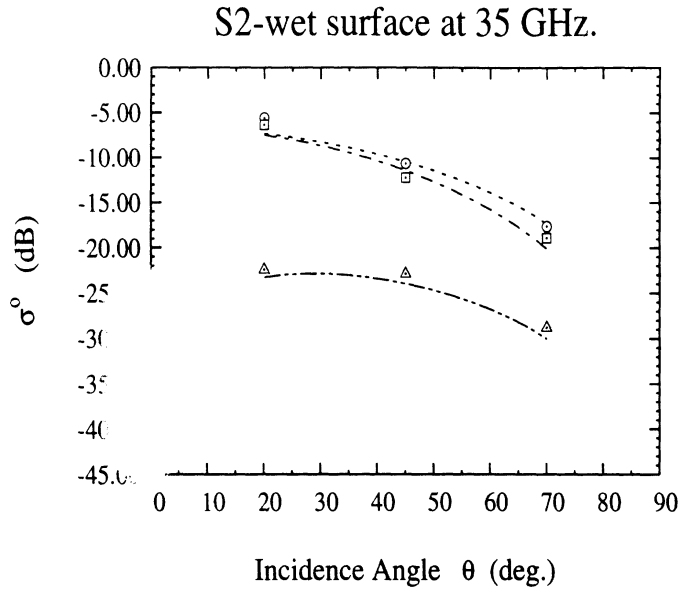

(a)

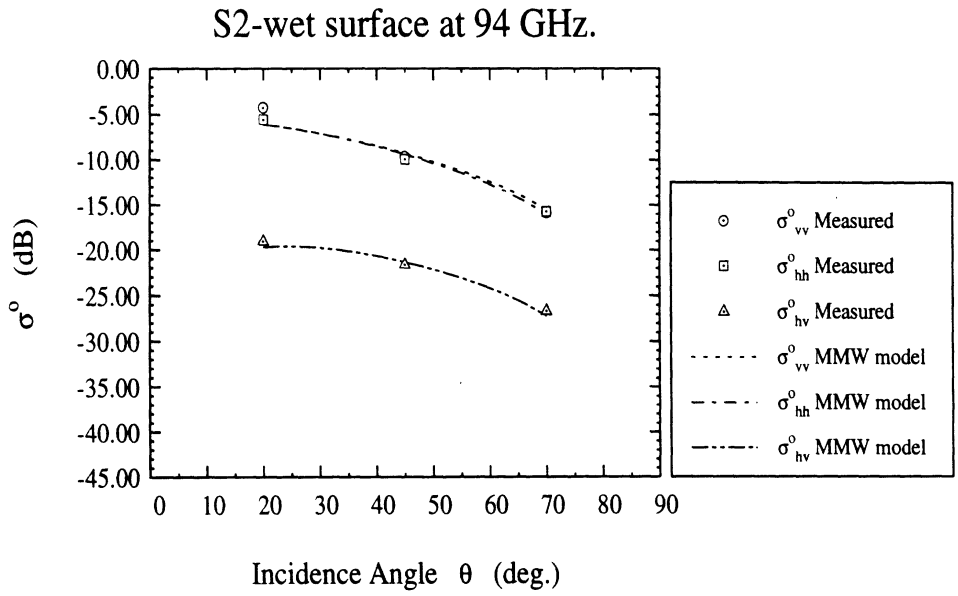

(b)

Figure 3.14: Comparison between measured data of S2-wet soil surface and the MMW semi-empirical surface scattering model at (a) 35 GHz, (b) 94 GHz.

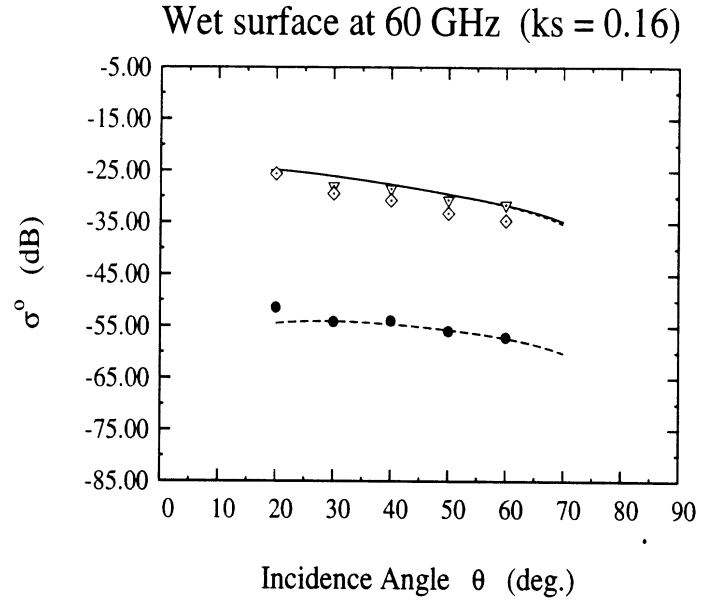

(a)

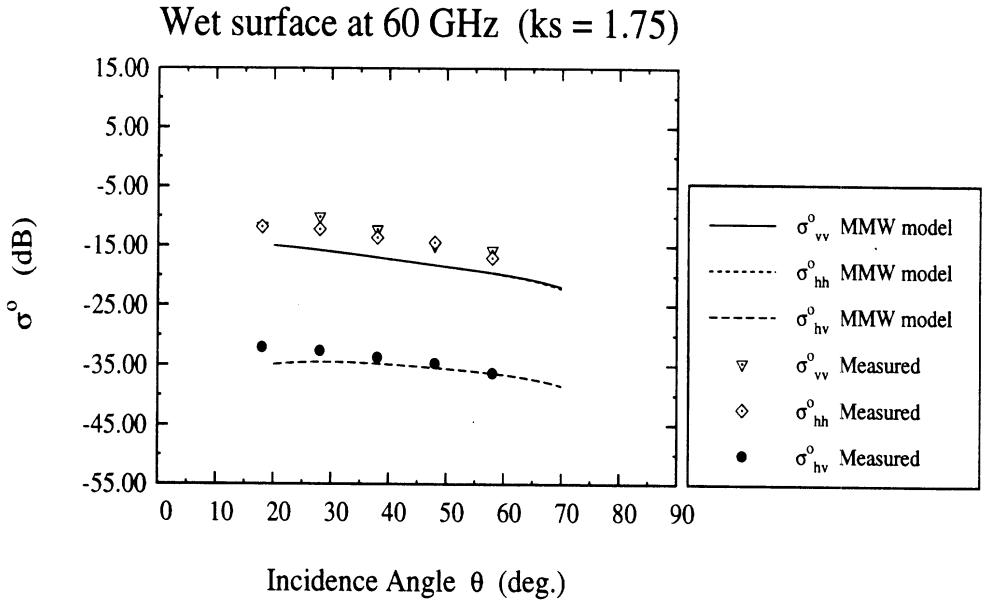

(b)

Figure 3.15: Comparison between measured data for wet soil surfaces ($\epsilon_r = 1.9 + j\ 0.4$) at 60 GHz and the MMW semi-empirical surface scattering model for (a) $ks = 0.16$, and (b) $ks = 1.75$. (Data from Yamasaki *et al.*).

tions, surface scattering is the dominant contribution and it can be modeled using a set of semi-empirical expressions. The semi-empirical model was found to be in good agreement with an independent data set for wet soil surfaces measured at 60 GHz.

CHAPTER IV

MODELING OF VOLUME SCATTERING FROM SOIL SURFACES AT MILLIMETER-WAVE FREQUENCIES

4.1 Introduction

In Chapter III, wet-soil data, measured at 35 and 94 GHz, was used to develope a semi-empirical surface scattering model that relates the surface scattering component of the total backscatter to the roughness parameter ks and the dielectric constant of soil. None of the dry soil data was incorporated in the developement of the semi-empirical model under the assumption that volume scattering might be significant at millimeter-wave frequencies. This assumption is based on the fact that at millimeter-wave frequencies the dielectric inhomogenieties within the dry soil medium can be of appreciable size compared to wavelength.

In this chapter, the surface and volume scattering contributions to the measured backscattering response from dry soil surfaces are considered. The semi-empirical surface scattering model, developed in the previous chapter, is used to compute the surface scattering contribution from the dry soil surfaces while the radiative transfer theory is used to compute the volume scattering contribution.

In the next section, evidence on the presence of significant volume scattering from dry soil surface at millimeter-wave frequencies is presented. In Section 4.3, the various available volume scattering models are discussed briefly. Then, a model based on radiative transfer theory is proposed in Section 4.5 to compute the volume scattering contribution from a thin dry soil layer with an undulating surface. Finally, in Section 4.6, the sum of the surface scattering contributions, computed using the semi-empirical model, and the volume scattering contribution, computed using the radiative transfer based-model, is compared with the measured backscattering response from the dry soil surfaces.

4.2 Evidence of Volume Scattering from Soils

Before we embark on a detailed examination of σ^v, the volume backscattering contribution to the total backscattering coefficient σ^o, it would be instructive to examine the evidence we have in support of conducting such an examination in the first place. After all, studies conducted at centimeter wavelengths have shown that the behavior of the backscatter from random surfaces can be explained by surface scattering alone, without the need to add a volume-scattering contribution. The need to consider volume scattering at millimeter wavelengths can be illustrated through an examination of the experimental data shown in Fig. 4.1 which include a set of plots of σ^o_{hh} and σ^o_{hv} for a dry soil surface and another set for the same surface immediately after wetting the surface with a fine mist using a sprinkler system, thereby preserving the roughness of the surface. According to surface scattering models, both theoretical and empirical, increasing the soil moisture content causes the level of σ^o to increase at all angles of incidence for all polarization configurations as depicted in Fig. 4.1.

This is certainly not the behavior observed in Fig. 4.1. For HH polarization, σ^o_{hh} of the dry surface at $\theta = 20^o$ is slightly lower than that for the wet surface, but at 70^o, σ^o_{hh} for the dry soil surface is *higher* than that for the wet surface. A similar, but even more pronounced, behavior is observed for HV polarization. The explanation for these observations stems from the following properties:

1. Surface scattering increases with increasing moisture content (dielectric constant), as stated earlier.

2. For surface scattering, σ^s varies with θ as $\cos^3\theta$ to $\cos^4\theta$, depending on surface roughness.

3. Volume scattering decreases with increasing moisture content, in part because the air-soil transmission coefficient decreases with increasing moisture content and in large part because the extinction in the soil medium increases rapidly with moisture content.

4. The volume scattering coefficients exhibit a very weak response as a function of the incidence angle θ.

5. The dimensions of the air voids (see Fig. 3.7), which constitute the scattering particles in the soil medium, are such that the scattering is in the Rayleigh region, which exhibits a λ^{-4}-dependence. Consequently, volume scattering is insignificantly small at centimeter wavelengths, but becomes important at millimeter wavelengths when the soil surface is dry.

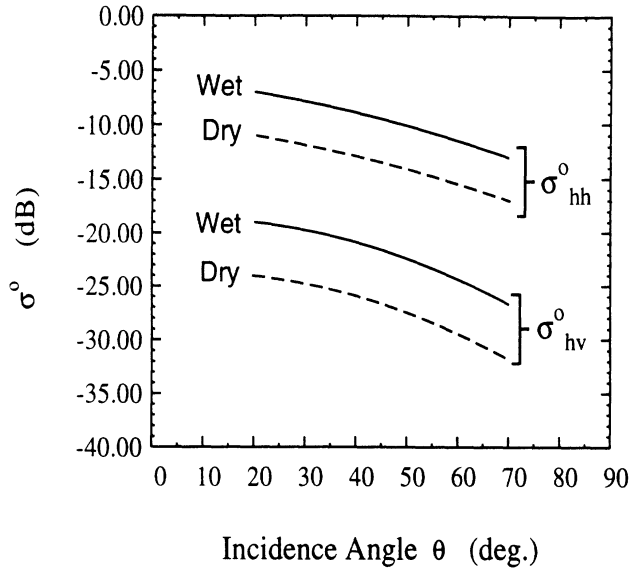

(a)

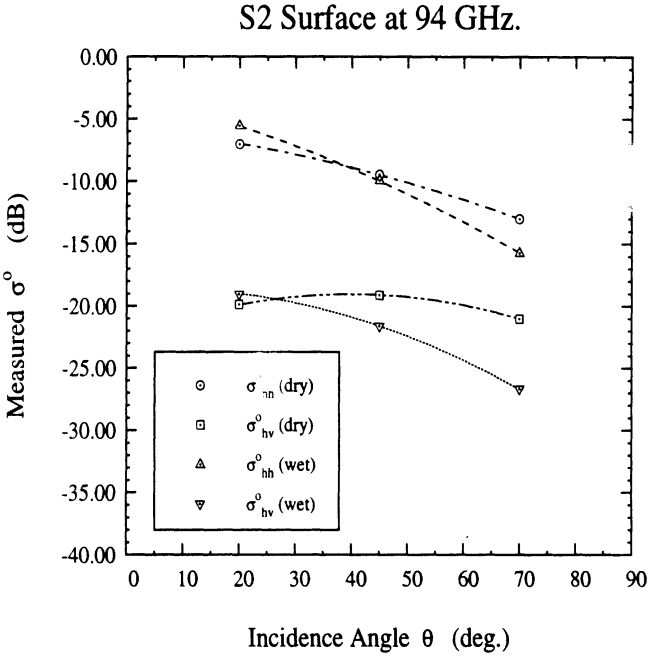

(b)

Figure 4.1: (a) Expected angular behavior of the backscatter response from soil surfaces under dry and wet conditions when only surface scattering is present, and (b) measured σ^o_{hh} and σ^o_{hv} for wet and dry surface conditions at 94 GHz ($ks = 5.16$). Note that at 70°, σ^o(dry) is greater than σ^o(wet) for both polarizations, evidence of volume scattering contribution.

4.3 Review of Volume Scattering Models

Two distinct approaches have been developed over the years to model volume scattering from random media, namely, the wave approach (or analytic wave theory) and the intensity approach (or radiative transfer theory). The wave approach starts with Maxwell's equations and in principle includes all multiple scattering, interference, and diffraction effects [19]. However, the mathematical complexity associated with solutions of the analytic wave theory prohibit its implementation unless certain approximations are applied. One frequently used approximation is the Born approximation [5], [22], [23], [55]. In this approximation, the permittivity at any point in the random medium is modeled as the sum of two components, a constant (mean) component and a fluctuating component. The scattered field is then expressed in terms of a volume integral equation [8] with unknown distributed sources that are proportional to both the total field inside the random medium and the fluctuating component of the permittivity. The integral equation is solved iteratively. However, the iterative solution is only valid when the variance of the fluctuating component of the permittivity is much smaller than the mean permittivity. This condition cannot be satisfied for soil media, in general, because of the large difference between the dielectic constant of air $\epsilon_a = 1$ and the dielectric constant of solid material $\epsilon_{ss} = 4.7$.

The radiative transfer theory on the other hand does not start with Maxwell's equations. It assumes rather that there is no correlation between fields scattered from different particles within the medium and therefore it deals directly with the transfer of energy through the random medium in which the addition of power rather than the addition of fields hold. The development of the theory is heuristic and lacks the mathematical rigor of the analytic wave theory but includes the diffraction and interference effects [60]. However, it is easier to implement and has been used suc-

cessfully in modeling volume scattering from vegetation and meteorological targets at both centimeter and millimeter wavelengths [58],[59],[70], [26]. The radiative transfer theory will be further discussed in the next section.

Recently, a new equation called the dense medium radiative transfer equation (DMRT) was introduced [53]. The DMRT equation was derived from the wave theory for electromagnetic wave propagation and scattering in dense media. In its derivation, the correlation between the fields internal to the scattering particles was taken into account by computing the mean field and the effective propagation constant of a dense random medium of discrete scatterers using the quasicrystalline approximation with coherent potential (QCA-CP). By assuming that the scattering particles are much smaller than a wavelength, the derivation simplifies and the DMRT equation is obtained. The DMRT equation takes a form similar to the conventional radiative transfer equation (CRT). Hence, all existing techniques that were developed in order to solve the CRT equation can be readily applied to the solution of the DMRT equation.

In this chapter, DMRT equation will not used in computing the volume scattering contribution from dry soil surfaces at millimeter-wave frequencies. This decision is based on two reasons: (1) the scattering particles in the dry soil medium can be of appreciable size compared to wavelength, and (2) the range of validity of the QCA-CP approximation is known yet. In fact, it will be shown experimentally in Chapter VII that for dense random media with fractional volumes higher than 15%, the QCA-CP approximation can underestimate the amount of scattering and extinction in a dense random medium. In this chapter, the conventional radiative transfer theory, discussed further in the next section, will be used to compute the volume scattering contribution from dry soil surfaces at millimeter-wave frequencies.

4.4 Vector Radiative Transfer Theory

Vector radiative transfer theory is concerned with the propagation and scattering of the vector specific intensity $\mathbf{I}(\bar{r}, \hat{s})$ within a medium of randomly located and oriented discrete scatterers. The vector specific intensity is a function of both position $\bar{r}$ and direction of propagation $\hat{s}$. The Stokes vector representation usually is chosen for representing $\mathbf{I}(\bar{r}, \hat{s})$ in order to incorporate the polarization state of the propagation wave. The propagation of the specific intensity is governed by the vector radiative transfer equation

$$\frac{d\mathbf{I}(\bar{r}, \hat{s})}{ds} = -\bar{\bar{\kappa}}_{\mathbf{e}}\, \mathbf{I}(\bar{r}, \hat{s}) - \kappa_{ag}\, \mathbf{I}(\bar{r}, \hat{s}) + \int_{4\pi} d\omega'\, \bar{\bar{\mathbf{P}}}(\hat{s}, \hat{s}')\, \mathbf{I}(\bar{r}, \hat{s}') \tag{4.1}$$

where $\bar{\bar{\kappa}}_{\mathbf{e}}$ is a 4×4 extinction matrix, $\bar{\bar{\mathbf{P}}}(\bar{r}, \hat{s}, \hat{s}')$ is a 4×4 phase matrix and $\kappa_{\mathbf{ag}}$ is the absorption coefficient of the background medium. The phase and extinction matrices describe the scattering and extinction properties of the random medium. The phase matrix relates the intensity incident on a differential volume of the random medium to the scattered intensity while the extinction matrix describes the attenuation of the intensity due to absorption and scattering in the differential volume of scatterers. The phase matrix is computed by averaging the modified Stokes matrix of a single particle over the size and orientation distributions of particles in the random medium. The extinction matrix is computed similarly by averaging the scattering matrix of a single particle in the forward scattering direction over the size and orientation distributions. The first two terms on the right hand side of equation (4.1) represent the amount of extinction incurred on the specific intensity by the scattering particles and the background medium while the third term accounts for the increase in $\mathbf{I}(\bar{r}, \hat{s})$ due to scattering of specific intensities $\mathbf{I}(\bar{r}, \hat{s}')$ incident on the differential volume from all

other directions.

The Iterative method and the numerical method (the discrete ordinate-eigen analysis method) are two popular techniques for solving the above integro-differential equation. In the iterative method, scattering is treated as a small perturbation. The zeroth order solution is obtained by neglecting scattering, and is inserted back into the integro-differential equations as a source term to derive the first order solution. The above procedure is repeated iteratively to derive higher order solutions. The order of iteration is proportional to the order of multiple scattering considered in the solution. The iterative method is mathematically simple and when the albedo is small, the iterative solution converges quickly. This is particularly usefull since closed-form solutions are available for the first and second iterative solutions. For general values of the albedo, the integro-differential equation is best solved numerically using the discrete ordinate-eigen analysis method. The discrete ordinate-eigen analysis method can be used to calculate the exact solution of the radiative transfer equation for the specific intensity in the scattering medium such that all orders of multiple scattering are included in the solution. In this method, Fourier series expansion of the RT equation in the azimuthal directions is first applied to the RT equation resulting in a set of RT equations with no azimuthal dependence. For each Fourier component, the resulting integro-differential equation is solved using the method of Gaussian quadrature. The integrals in the RT equations, which are functions of the elevation angle θ, are approximated by an appropriate weighted sum resulting in a set of first order equations with constant coefficients which are solved by enforcing the boundary conditions and computing the eigenvalues and eignvectors. Once the RT equation is solved for any scattered direction, the backscattering coefficients are easily computed. The details of this method can be found in [60], [21].

4.5 Volume Scattering from an Undulating Soil Surface

To compute the volume scattering contribution, we propose to use radiative transfer (RT) theory. As was noted earlier, the moisture content of the wet soils was essentially uniform with depth over the top four centimeters, but for the dry soils, the top surface layer, which was on the order of 1-3 cm thick, was very dry and the soil layer underneath it was generally fairly wet. Hence, we decided to model the soil medium as a thin layer of thickness h overlying a wet-soil half space. The thin layer, which is bounded by gently undulating random surfaces from above and below as depicted in Fig. 4.2, contains air voids (scatterers) embedded in the soil background.

One approach for computing volume scattering from a layer of random medium with irregular interfaces is to solve the integro-differential equation of radiative transfer while simultaneously satisfying the boundary conditions imposed by the irregular surfaces [62], [25]. However, in this approach the scatterers are required to be far away from either interface [35]. This requirement cannot be satisfied in case of thin layer of dry soil.

In this chapter, we propose an alternative approach where the total volume scattering contributed by the layer is obtained by performing an incoherent addition of the volume scattering contributions emerging from all points on the surface, realized by weighing the contributions in accordance with the probability density function of angles θ_t and ϕ_t that define the unit vector $\hat{n}$ normal to the surface (see Fig 4.2). This approach is similar to that reported in [62] for computing surface scattering from tilted perturbed planes. The volume contribution emerging from any point on the surface is obtained by solving the radiative transfer equation for a layer of random

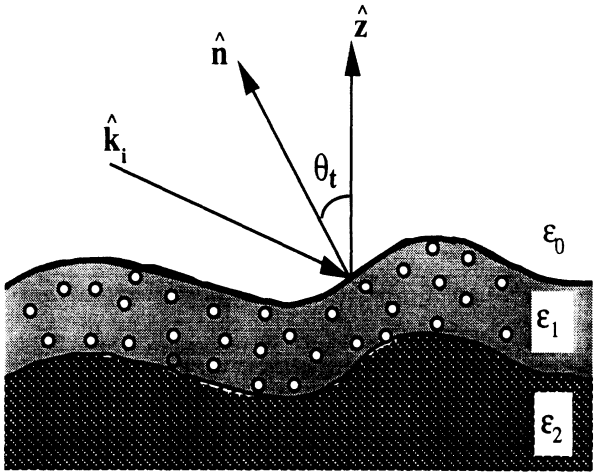

Figure 4.2: Proposed model for the dry soil medium.

medium with plane parallel interfaces. The proposed technique is based on two assumptions. The first is that in a thin layer scattering is essentially a local process and multiple scattering can occur only between neighboring voids. Hence, the backscattered intensities emerging from different points on the surface are uncorrelated. The second assumption is that the radius of curvature of the gently undulating air-soil interface is large compared to wavelength so that the boundaries of the thin layer can be approximated locally by plane parallel interfaces.

4.5.1 Volume Scattering from Plane Parallel Random Media

In this section, we consider the solution of the radiative transfer equation for a plane parallel random medium containing spherical scatterers [25], [21], [60]. In this solution we assume that, similar to dry soils, the scattering layer has a background permittivity that is different from air. In this case the incident specific intensity undergoes multiple reflections between the parallel interfaces and suffers from extinction due to absorption and scattering as it propagates inside the scattering layer. To solve

the RT equation, we start by separating the specific intensity into a reduced incident intensity and a diffuse or incoherent intensity. The radiative transfer equation can be then written in terms of the diffuse specific intensity with the reduced incident intensity acting as a source term. The radiative transfer equation of the diffuse specific intensity is solved numerically using the discrete ordinate-eigen analysis technique described earlier. Details of the mathematical formulation can be found in the paper by Wen *et al.* [68].

The scattered specific intensity $\mathbf{I}^s$, which is the solution for the radiative transfer equation, is related to the incident specific intensity through the modified Mueller matrix $\bar{\bar{\mathbf{M}}}$ [60]

$$\mathbf{I}^s = \frac{1}{A\ cos\,\theta_l}\ \bar{\bar{\mathbf{M}}}\ \mathbf{I}^i \tag{4.2}$$

where A is the illuminated area and θ_l is the angle subtended between the direction of propagation of the scattered field and the unit vector normal to the surface of the plane parallel medium. Although $\bar{\bar{\mathbf{M}}}$ which characterizes scattering from the random medium is not explicitly known, it can be determined by computing $\mathbf{I}^s$ for a linearly independent set of incident polarizations such as vertical, horizontal, 45° linear, and left hand circular polarizations. The incident specific intensities that correspond to these polarizations are

$$\mathbf{I}^i_v = \begin{bmatrix} 1 \\ 0 \\ 0 \\ 0 \end{bmatrix},\quad \mathbf{I}^i_h = \begin{bmatrix} 0 \\ 1 \\ 0 \\ 0 \end{bmatrix},\quad \mathbf{I}^i_{45} = \begin{bmatrix} \frac{1}{2} \\ \frac{1}{2} \\ 1 \\ 0 \end{bmatrix},\quad \mathbf{I}^i_{lhc} = \begin{bmatrix} \frac{1}{2} \\ \frac{1}{2} \\ 0 \\ 1 \end{bmatrix} \tag{4.3}$$

In general,the columns of the modified Mueller matrix, $\bar{\bar{\mathbf{M}}}_j$, can be computed from

the scattered specific intensities ($\mathbf{I}^s_v$, $\mathbf{I}^s_h$, $\mathbf{I}^s_{45}$, and $\mathbf{I}^s_{lhc}$) as follows:

$$\begin{aligned}
\bar{\bar{\mathbf{M}}}_1 &= A\, cos\theta_l\, \mathbf{I}^s_v \\
\bar{\bar{\mathbf{M}}}_2 &= A\, cos\theta_l\, \mathbf{I}^s_h \\
\bar{\bar{\mathbf{M}}}_3 &= A\, cos\theta_l \left(\mathbf{I}^s_{45} - \frac{1}{2}\left[\mathbf{I}^s_v + \mathbf{I}^s_h\right]\right) \\
\bar{\bar{\mathbf{M}}}_4 &= A\, cos\theta_l \left(\mathbf{I}^s_{lhc} - \frac{1}{2}\left[\mathbf{I}^s_v + \mathbf{I}^s_h\right]\right)
\end{aligned} \tag{4.4}$$

In backscatter, the modified Mueller matrix for an azimuthally symmetric random medium is given by

$$\bar{\bar{\mathbf{M}}} = \begin{bmatrix}
< |s'_{vv}|^2 > & < |s'_{hv}|^2 > & & \\
< |s'_{hv}|^2 > & < |s'_{hh}|^2 > & \bullet\bullet\bullet & \\
0 & 0 & & \\
0 & 0 & &
\end{bmatrix}$$

$$\begin{bmatrix}
0 & 0 \\
0 & 0 \\
\bullet\bullet\bullet & \\
< Re(s'_{vv}s'^{*}_{hh}) + |s'_{hv}|^2 > & - < Im(s'_{vv}s'^{*}_{hh}) > \\
< Im(s'_{vv}s'^{*}_{hh}) > & < Re(s'_{vv}s'^{*}_{hh}) - |s'_{hv}|^2 >
\end{bmatrix} \tag{4.5}$$

where s'_{ij} $(i,j = v,h)$ are the backscattering amplitudes [44]. Although the backscattering amplitudes cannot be computed using the radiative transfer equation, they are introduced here for the mathematical convenience they provide. The elements of the forth column of the modified Mueller matrix can be expressed in terms of the elements of the three other columns: $M_{34} = -M_{43}$ and $M_{44} = M_{33} - 2M_{21}$. In this case, only the first three columns of the modified Mueller matrix need to be computed. Hence, the radiative transfer equation is solved numerically for only $\mathbf{I}^s_v$, $\mathbf{I}^s_h$, and $\mathbf{I}^s_{45}$.

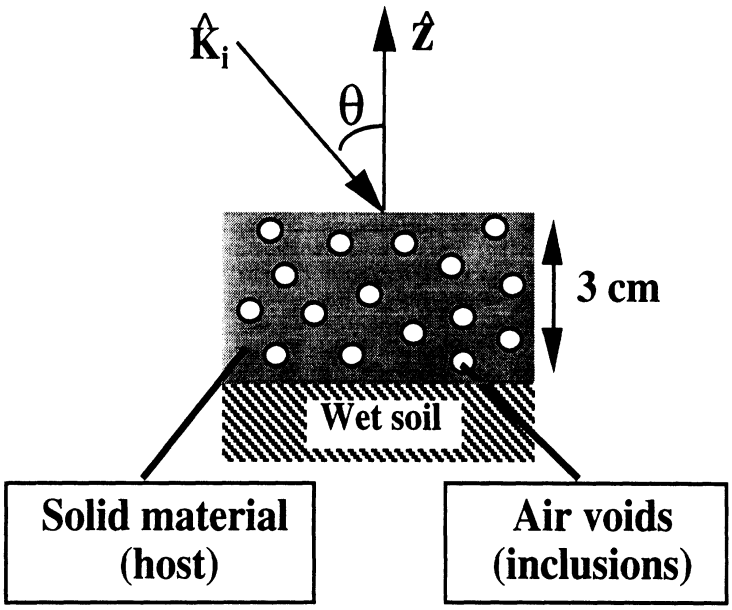

Figure 4.3: A Scattering layer overlying a homogeneous half space dielectric with planar interfaces.

The elements of covariance matrix $\bar{\bar{\mathbf{W}}}'$, which will be used in the next section, can be expressed in terms of the elements of the modified Mueller matrix following few simple algabraic manipulations. An explicit expression for the covariance matrix in terms of the scattering amplitudes is

$$\bar{\bar{\mathbf{W}}}' = \begin{bmatrix} < |s'_{vv}|^2 > & 0 & < s'_{vv} s'^{*}_{hh} > \\ 0 & < |s'_{hv}|^2 > & 0 \\ < s'_{hh} s'^{*}_{vv} > & 0 & < |s'_{hh}|^2 > \end{bmatrix} \tag{4.6}$$

4.5.2 Incoherent Averaging of Scattered Power from an Undulating Surface

The incoherent averaging process starts by computing first the local angle of incidence θ_l for every point on the surface using the relation $cos\theta_l = -\hat{k}_i.\hat{n}$. Here, $\hat{k}_i$ defines the direction of propagation of the incident field in the global frame of reference (see Fig. 4.4) and $\hat{n}$ represents the unit vector normal to the random surface and is given by

$$\hat{n} = \cos\phi_t \sin\theta_t \hat{x} + \sin\phi_t \sin\theta_t \hat{y} + \cos\theta_t \hat{z} \tag{4.7}$$

with angles θ_t and ϕ_t as defined in Fig. 4.4. In effect, θ_l is a function of the angles of incidence, θ_i and ϕ_i, and the angles, θ_t and ϕ_t, defining the surface normal.

The technique described in the previous section is then used to compute the covariance matrix $\bar{\bar{\mathbf{W}}}'$ for a plane parallel random medium for a particular local angle of incidence θ_l. By performing simple coordinate tranformations on $\bar{\bar{\mathbf{W}}}'$, another matrix $\bar{\bar{\mathbf{W}}}$ is obtained for the same plane parallel random medium. However, $\bar{\bar{\mathbf{W}}}$ is defined in this case in the global frame of reference. The average covariance matrix $\bar{\bar{\mathbf{W}}}_\mathbf{a}$ of the thin undulating layer is computed by averaging $\bar{\bar{\mathbf{W}}}$ over all the points on the surface, each weighed by the probability density function of the angles defining the surface normal, namely,

$$\bar{\bar{\mathbf{W}}}_\mathbf{a} = \int_0^{\pi/2} \int_0^{2\pi} p_{\theta_t,\phi_t}(\theta_t, \phi_t)\, \bar{\bar{\mathbf{T}}}\, \bar{\bar{\mathbf{W}}}'\, \bar{\bar{\mathbf{T}}}^{*\mathbf{t}}\, d\phi_t\, d\theta_t \tag{4.8}$$

where $p_{\theta_t,\phi_t}(\theta_t, \phi_t)$ is the joint probability density function of the angles (θ_t, ϕ_t) derived in Appendix A. Futhermore, the average covariance matrix $\bar{\bar{\mathbf{W}}}_\mathbf{a}$ can be expressed in

terms of the averaged scattering amplitudes as follows:

$$\bar{\bar{\mathbf{W}}}_{\mathbf{a}} = \begin{bmatrix} < |s^a_{vv}|^2 > & 0 & < s^a_{vv} s^{a*}_{hh} > \\ 0 & < |s^a_{hv}|^2 > & 0 \\ < s^a_{hh} s^{a*}_{vv} > & 0 & < |s^a_{hh}|^2 > \end{bmatrix} \tag{4.9}$$

The volume-scattering coefficients σ^v_{ij} $(i\ , j = v\, or\, h)$ can be obtained directly from (4.9) by multiplying the appropriate elements with $4\pi/A$.

It should be noted that:

1. The elements of matrix $\bar{\bar{\mathbf{W}}}'$ need to be computed for only a finite set of local angles of incidence θ_l. By fitting these elements to polynomials using the standard Least Square error procedure [38], matrix $\bar{\bar{\mathbf{W}}}_{\mathbf{a}}$ can be easily computed for all combinations of θ_t and ϕ_t.

2. When $\theta_l > 90^o$ (for a shadowed point on the surface), the covariance matrix $\bar{\bar{\mathbf{W}}}'$ is set to zero.

In the remaining part of this section, the details of the coordinate transformations incorporated in the averaging process, are described. We start by defining a new column vector $\bar{\mathbf{S}}' = [s'_{vv}, s'_{hv}, s'_{hh}]^t$ where s'_{ij} $(i, j = v, h)$ are the scattering amplitudes of the plane parallel random medium evaluated in the local frame of reference. In backscatter, the covariance matrix can be expressed in terms of vector $\bar{\mathbf{S}}'$

$$\bar{\bar{\mathbf{W}}}' = < \bar{\mathbf{S}}' \bar{\mathbf{S}}'^{*\mathbf{t}} > \tag{4.10}$$

Vector $\bar{\mathbf{S}}'$ can be transformed to the global frame of reference through the coordinate

transformation matrix, $\bar{\bar{\mathbf{T}}}$,

$$\bar{\mathbf{S}} = \bar{\bar{\mathbf{T}}}\ \bar{\mathbf{S}}' \tag{4.11}$$

Here $\bar{\mathbf{S}} = [s_{vv}, s_{hv}, s_{hh}]^t$, and s_{ij} $(i,j = v,h)$ are the scattering amplitudes of the same plane parallel random medium evaluated in the global frame of reference. The coordinate transformation matrix is given by

$$\bar{\bar{\mathbf{T}}} = \begin{bmatrix} (\hat{v}_s.\hat{v'}_s)^2 & 2\,(\hat{v}_s.\hat{v'}_s)(\hat{v}_s.\hat{h'}_s) & (\hat{v}_s.\hat{h'}_s)^2 \\ (\hat{v}_s.\hat{v'}_s)(\hat{v'}_s.\hat{h}_s) & (\hat{v}_s.\hat{v'}_s)(\hat{h}_s.\hat{h'}_s) + (\hat{v}_s.\hat{h'}_s)(\hat{h}_s.\hat{v'}_s) & (\hat{h}_s.\hat{h'}_s)(\hat{v}_s.\hat{h'}_s) \\ (\hat{h}_s.\hat{v'}_s)^2 & 2\,(\hat{h}_s.\hat{h'}_s)(\hat{h}_s.\hat{v'}_s) & (\hat{h}_s.\hat{h'}_s)^2 \end{bmatrix} \tag{4.12}$$

where $(\hat{v}_s,\ \hat{h}_s)$ and $(\hat{v'}_s,\ \hat{h'}_s)$ are the unit polarization vectors of the field propagating along direction $\hat{k}_s$ and are defined in the global and local frames of reference respectively. Note that in backscatter $\hat{k}_i = \hat{k}_s$ $(\theta_s = \pi - \theta_i$ and $\phi_s = \pi + \phi_i)$. Unit vectors $\hat{v}_s$, $\hat{h}_s$, $\hat{k}_s$, $\hat{v'}_s$, and $\hat{h'}_s$ are given by

$$\begin{aligned} \hat{k}_s &= -[\cos\phi_s \sin\theta_s\, \hat{x} + \sin\phi_s \sin\theta_s\, \hat{y} + \cos\theta_s\, \hat{z}] \\ \hat{h}_s &= \frac{\hat{z} \times \hat{k}_s}{|\hat{z} \times \hat{k}_s|} \\ \hat{v}_s &= \hat{h}_s \times \hat{k}_s \end{aligned} \tag{4.13}$$

$$\begin{aligned} \hat{h'}_s &= \frac{\hat{k}_s \times \hat{n}}{|\hat{k}_s \times \hat{n}|} \\ \hat{v'}_s &= \hat{k}_s \times \hat{h'}_s \end{aligned} \tag{4.14}$$

After few simple algabraic manipulations, the covariance matrix $\bar{\bar{\mathbf{W}}} = <\bar{\mathbf{S}}\ \bar{\mathbf{S}}^{*\mathbf{t}}>$

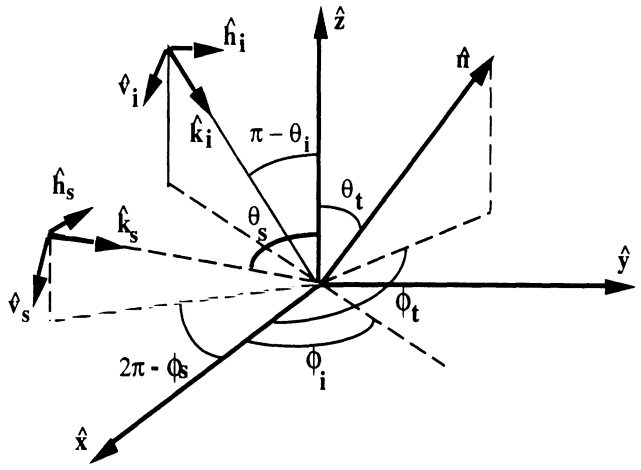

Figure 4.4: Backscattering alignment (BSA) convention.

of the plane parallel random medium in the global frame of reference can be related to $\bar{\bar{\mathbf{W}}}'$ through the following relation

$$\bar{\bar{\mathbf{W}}} = \bar{\bar{\mathbf{T}}}\, \bar{\bar{\mathbf{W}}}'\, \bar{\bar{\mathbf{T}}}^{*t} \tag{4.15}$$

4.6 Application of the Proposed Model to Measured Soil Surfaces

Solution of the radiative transfer equations requires knowledge of the void's shapes, sizes, volume fraction and relative dielectric constant, in addition to the relative dielectric constants of both the background solid soil material and the wet soil half space. In this chapter, we have assumed that the air voids are spherical in shape with a relative dielectric constant $\epsilon_a = 1.0 + j0.0$. The void-size distribution function shown in Fig. 3.7a was used in the solution of the RT equations for surfaces S1 and S2, and that corresponding to S3 shown in Fig. 3.7b was used for the third surface. The relative dielectric constant of the background solid soil material was taken as

$\epsilon_{ss} = 4.7$, based on the empirical formula $\epsilon_{ss} = (1.01 + 0.44\rho_{ss})^2 - 0.062$ reported in [14], where $\rho_{ss} = 2.65$ g/cm^3 is the measured solid soil density (which agrees well with ρ_{ss} of sandy soils [62], [14]). The effective dielectric for the wet soil half space was assumed to be $\epsilon_2 = 7.0 + j4.0$ at 35 GHz and $\epsilon_2 = 5.0 + j2.5$ at 94 GHz. The voids volume fractions given in Table 3.2 were calculated on the basis of the measured bulk densities and solid soil density, $\nu_a = 1 - \rho_b/\rho_{ss}$.

The results of this approach for computing the volume backscattering contribution σ^v are summarized in the next section. By way of examining the relative importance of volume scattering, however, we calculated σ^v at 94 GHz for an upper layer containing air voids of uniform diameter, d_v. The results are shown in Fig. 4.5 , which shows σ^v as a function of d_v for a thickness $h = 3$ cm, and as a function of h for a void diameter $d_v = 0.1$ mm. The responses to h (Fig. 4.5b) indicate that the thin surface layer "appears" semi-infinite in depth once its actual depth h exceeds about 3 cm. The variations of σ^v with d_v displayed in Fig. 4.5a, which include both the Rayleigh and Mie regions, reaches saturation levels of about -4 dB for σ^v_{vv} and -7 dB for σ^v_{hv}. The saturation level for σ^v_{vv} is certainly comparable with or greater than the values measured for the wet soil surfaces at the same incidence angle and frequency, and for σ^v_{hv}, the saturation level is higher than all the wet-soil values of σ^v_{hv} displayed in Figs. 3.9, 3.14, and 3.15. Thus, the volume scattering contribution may indeed be a significant, or even the dominant, contribution depending on the void-size distribution. The volume scattering coefficients plotted in Fig. 4.5a approach the saturation stage when d_v exceeds 0.5 mm, which corresponds to $kr_v = kd_v/2 = \pi d_v\sqrt{\epsilon_r}/\lambda_o \simeq 0.86$, where λ_o is the free space wavelength ($\lambda_o = 3.2$ mm at 94 GHz) and $\epsilon_r = 3.1$ is the effective dielectric constant of the dry soil background. The soils investigated in this study had void size distributions extending between 0.02 mm and about 0.4 mm, with the

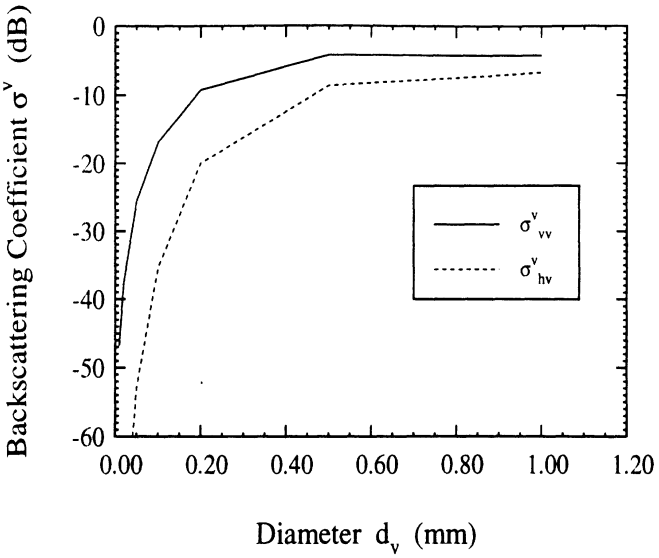

(a)

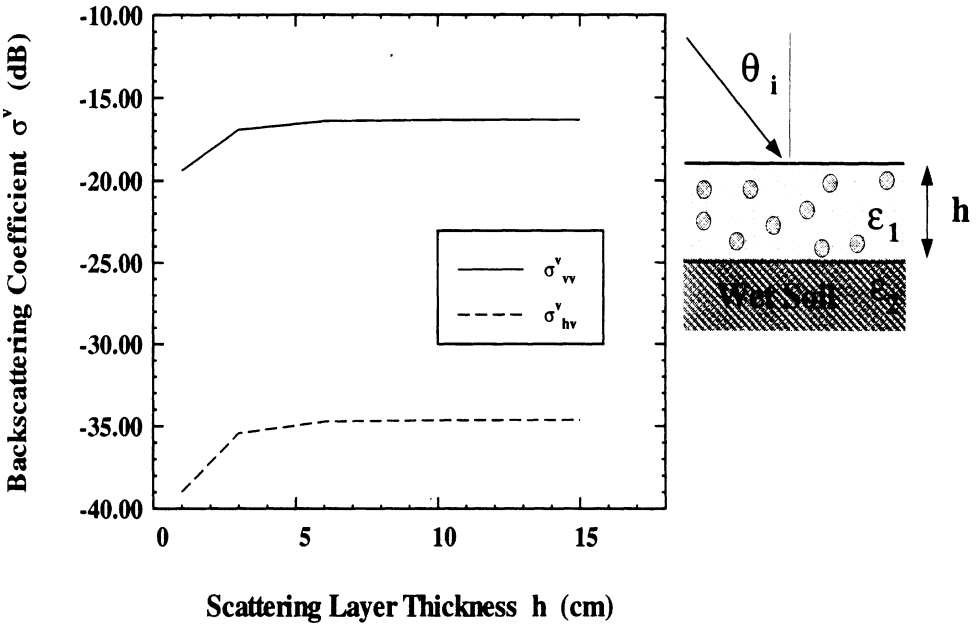

(b)

Figure 4.5: Computed sensitivity of σ^v to (a) particle diameter (for layer thinkness h = 3 cm), and (b) scattering layer thickness (for particle diameter d_v = 0.1 mm). The computations were conducted at 94 GHz for an incidence angle $\theta = 20^o$ and void volume fraction $\nu_a = 0.36$.

bulk of the voids having diameters smaller than 0.2 mm (see Fig. 3.7a).

4.6.1 Results

For the dry soil surfaces, the total backscattering coefficients σ^o_{ij} ($i, j = v$ or h) were computed according to (3.1) by adding incoherently the volume scattering contribution σ^v_{ij}, computed using the RT technique, to the surface scattering contribution σ^s_{ij}, calculated according to the empirical model described in the preceding chapter (equations (3.2)-(3.7)). Good overall agreement is observed between the computed values of σ^o_{ij} and the measured radar responses for all surfaces at both frequencies, as can be seen in Figures 4.6 through 4.8. In all cases, the thickness of the top dry soil surface layer was taken as 3-cm.

It must be pointed out that at 35 GHz, σ^o_{ij} is dominated by surface scattering with minimal contribution provided by volume scattering (σ^s_{ij} is typically larger than σ^v_{ij} by 10 dB). However, at 94 GHz the volume scattering component is comparable to the surface scattering component for the co-polarized scattering coefficients, as can be seen in Fig. 4.9a, and for cross-polarization, σ^o_{hv} is dominated by the volume contribution (Fig. 4.9b).

4.6.2 Soil Moisture Dependence

The cases considered in this chapter fall into two groups: (a) wet soils, which may be defined as those with moisture contents exceeding 0.12 g/cm^3 in the top 1-cm layer, and (b) dry soils, for which $m_v < 0.04$ g/cm^3 in the top 1-cm layer (see Table 3.2). For the wet-soil group, our analysis shows that the volume-scattering contribution may be ignored and that the total backscatter is dominated by the surface-scattering component. The volume-scattering contribution is very small because at millimeter

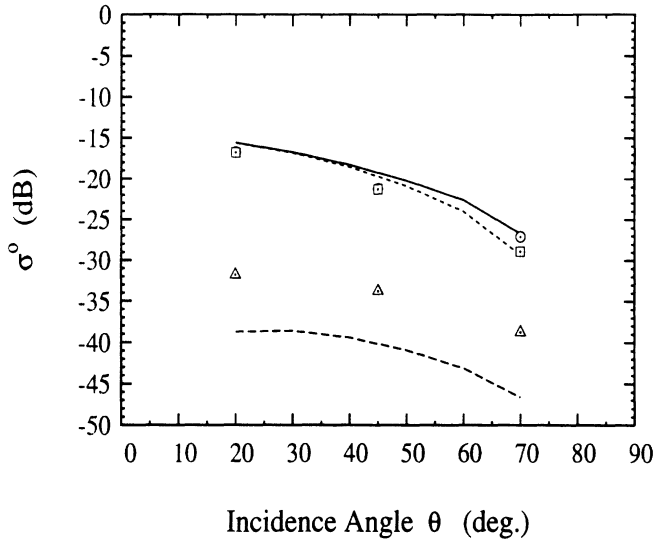

(a)

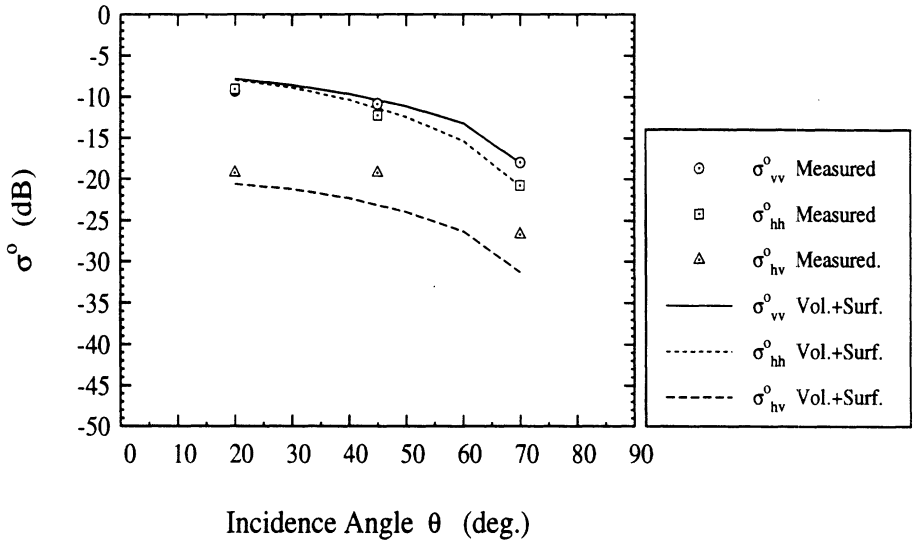

(b)

Figure 4.6: Comparison between the measured backscattering coefficient and the total backscattering coefficient σ^o predicted by the sum of surface and volume scattering contributions for surface S1 at (a) 35 GHz and (b) 94 GHz.

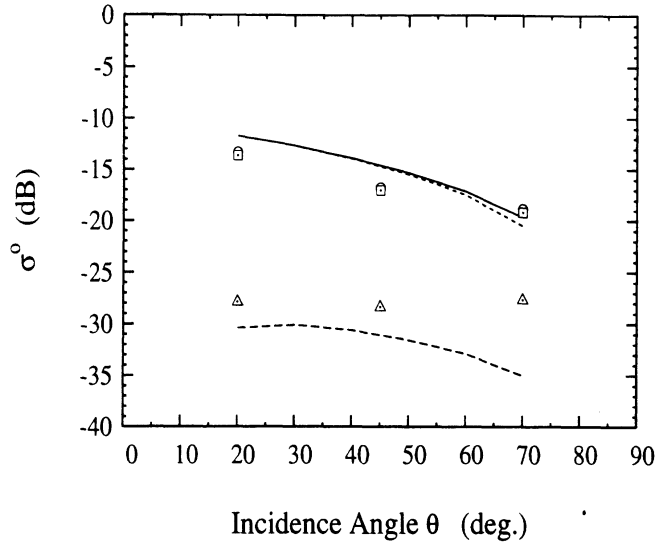

(a)

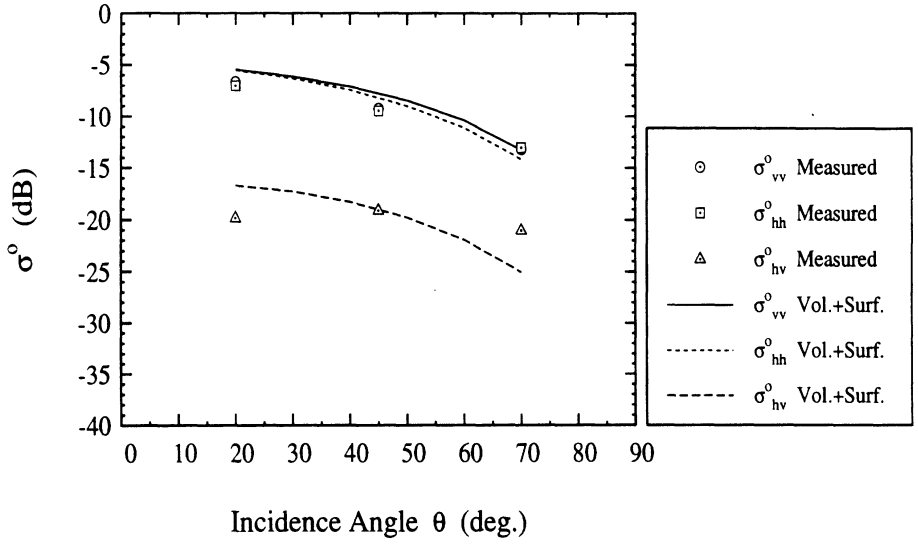

(b)

Figure 4.7: Comparison between the measured backscattering coefficient and the total backscattering coefficient σ^o predicted by the sum of surface and volume scattering contributions for surface S2 at (a) 35 GHz and (b) 94 GHz.

wavelengths the penetration depth is on the order of a few millimeters when $m_v >$ 0.1 g/cm^3.

For the dry-soils group, the volume-scattering contribution was computed by assuming the top surface layer to be 3 cm in thickness and totally dry. Although the measured values of m_v were very small, they were not exactly zero over the top 3-cm layer (Table 2). Nevertheless, they were assumed to be zero to simplify the calculation. A possible approach for modeling the dependence on moisture content is to treat the soil as a perfectly dry top surface layer of thickness h, overlying a very wet half-space, just as we have done in calculating the volume-scattering contributions for the dry soils examined in this study, but to also relate h to the average dielectric constant or moisture content of the upper 3-cm layer. Thus, h would vary from 3-cm for $m_v = 0$ down to zero thickness for $m_v = 0.15$ g/cm^3. These figures apply to 94 GHz and are at best a rough estimate based on radiative-transfer model calculations. Had we applied this approach to the calculations performed in connection with the dry soils, h would have been reduced from 3-cm down to about 2-cm, resulting in a change of about 1-2 dB in σ^v. Thus, verification of the applicability of such a model will have to await until further experimental investigations are performed for soils with moisture contents in the 0.04 to 0.15 g/cm^3 range.

4.7 Conclusions

Analysis of the measured radar data indicates that in general both surface and volume scattering contributions are present at MMW frequencies. For wet soil conditions, surface scattering is the dominant contribution and it can be modeled using a set of semi-empirical expressions. The volume contribution is important when the

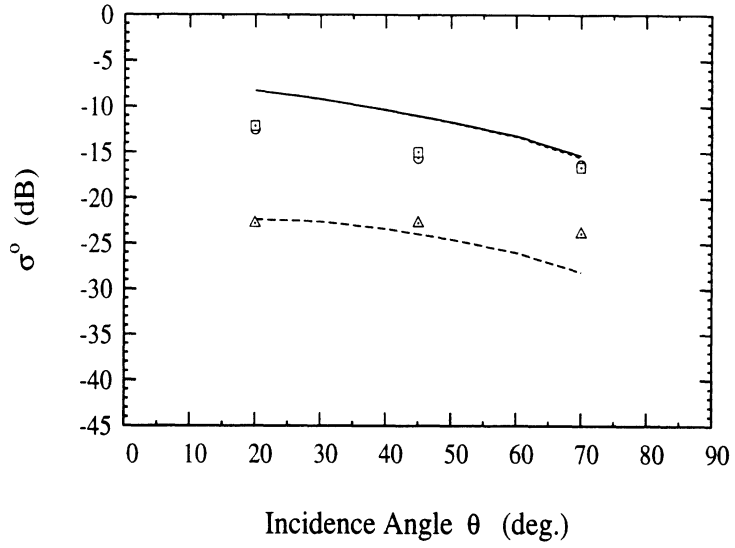

(a)

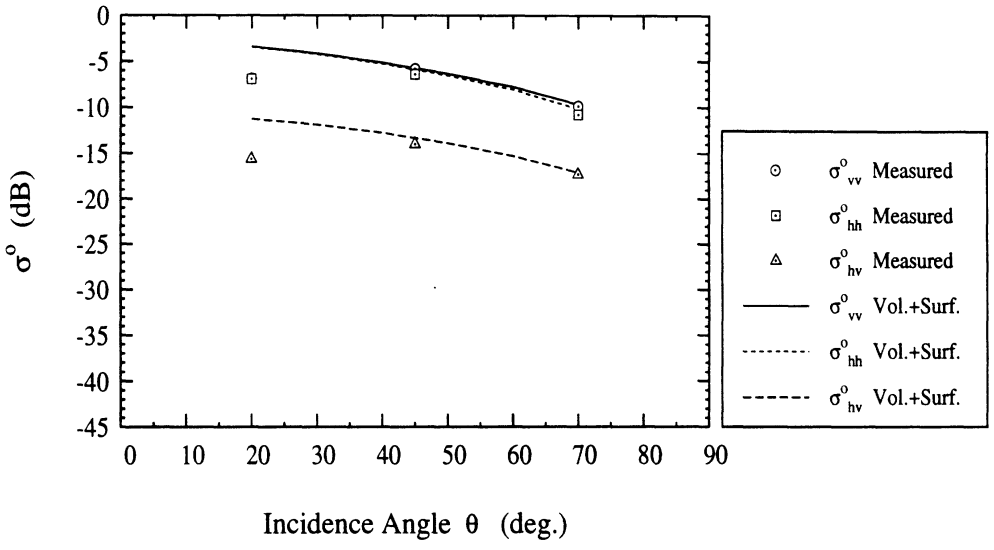

(b)

Figure 4.8: Comparison between the measured backscattering coefficient and the total backscattering coefficient σ^o predicted by the sum of surface and volume scattering contributions for surface S3 at (a) 35 GHz and (b) 94 GHz.

soil surface is dry, particularly at 94 GHz. Using radiative transfer theory, the volume scattering contribution from a thin dry-soil layer was calculated by treating the soil medium as comprised of air voids imbedded in a soil background. This approach, which led to good agreement with the experimental observations, indicates that at 94 GHz, for example, the surface and volume scattering components are of comparable magnitude for σ^o_{vv} and σ^o_{hh}, but for the cross-polarized σ^o_{hv}, volume scattering is the dominant contribution.

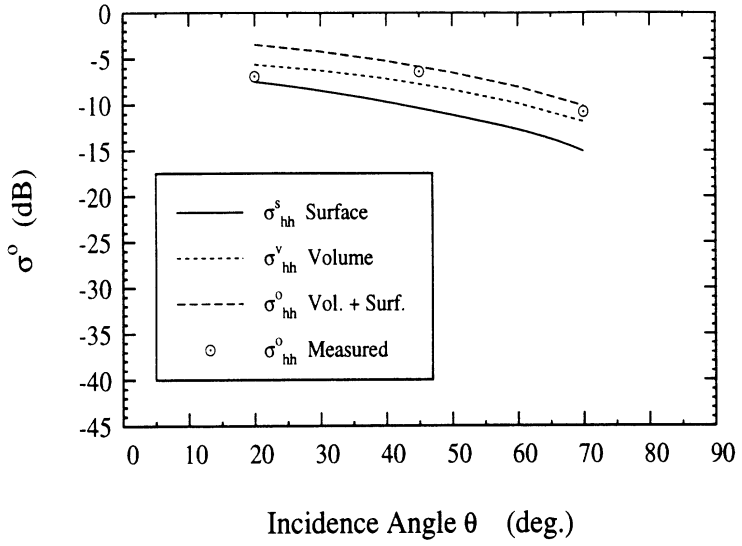

(a)

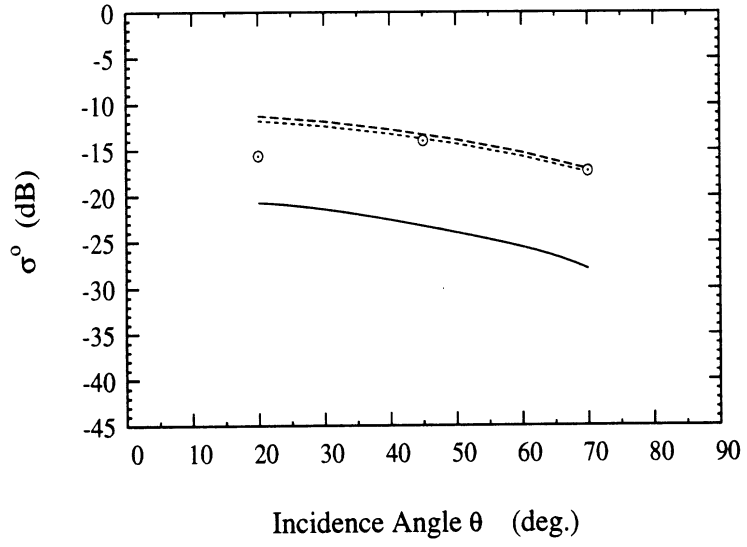

(b)

Figure 4.9: Contributions of the surface-scattering component alone, the volume-scattering component alone, and the sum of both components for surface S3 at 94 GHz: (a) σ^o_{hh} (b) σ^o_{hv}.

CHAPTER V

A NOVEL BISTATIC SCATTERING MATRIX MEASUREMENT TECHNIQUE USING A MONOSTATIC RADAR

As mentioned previously (in chapter I), existing theoretical models for random media may be categorized into two groups: (1) continuous media perturbation approaches such as the Born approximation, and (2) discrete scatterer approaches such as radiative transfer. In either of these two approaches, characterization of the propagation constant of the mean-field in the random medium is of great importance. The effective propagation constant, denoted here by $K = K_r + jK_i$, specifies how the mean-field propagates in a scattering medium. Here, K_r and K_i are respectively proportional to the phase velocity and the attenuation rate caused by absorption and scattering in the medium. For dense random media, analytical models, such as the effective field approximation (EFA) and the quasicrystalline approximation with coherent potential (QCA-CP), are widely used to compute the effective propagation constant. For example, the QCA-CP model which includes in its derivation the effects of multiple scattering between particles has been used in the developement of the dense medium radiative transfer theory (DMRT) [53]. In turn, the DMRT has

been used to model the backscattering response from layered dense random media [68],[69]. The applicability of these models depends in part on the range of validity of the QCA-CP model which has not been determined yet. Accurate measurements of the effective propagation constant (K) can be used for establishing the range of validity of the existing analytical models. Direct measurements can also be used in the developement of empirical models for the effective propagation constant. The aim of the second half of this thesis is to answer experimentally the following question: What is the range of validity of the existing analytical models, such as EFA and QCA-CP?

The standard approach to measure the effective propagation constant of dense random media is the free space transmission measurement technique (FSTM) [27], [17]. In this technique, a slab of the dense random medium is positioned between two antennas and the transmission coefficient is measured coherently. Then by moving the slab and measuring the transmission coefficient repeatedly, the mean transmission coefficient is computed from which the effective propagation constant of the random medium is calculated. The accuracy of the FSTM technique is limited primarily by three practical difficulties: (a) difficulty in maintaining phase coherency between the receiver and transmitter, (b) difficulty in generating many independent samples of the random medium, and (c) difficulty in minimizing the effects of systematic errors since K is computed from a single measured parameter, namely, the mean transmission coefficients.

Motivated by the need for an experimental procedure for the measurement of the effective propagation constant of dense random media, a new technique that overcomes the difficulties associated with the FSTM technique is considered. The new proposed technique will be refered to as: the *coherent bistatic scattering measurement*

technique (CBSM). In the CBSM technique, the bistatic scattering from a cluster of constituent particles of a random medium confined in a spherical volume will be measured. The coherent and incoherent components of the scattered fields can be separated using many independent measurements of the cluster for given incident and bistatic directions. Independent radar measurements are obtained by rotating the cluster of particles around its axis of symmetry, perpendicular to the direction of propagation, and/or randomizing the particles within the confining volume. The coherent scattered wave (mean field) is proportional to the effective dielectric constant (or equivalently the effective propagation constant) of the medium and the incoherent scattered power is proportional to the phase function of the random medium.

In the proposed CBSM technique, bistatic scattering measurements of a point target (the cluster of constituent particles) is required. Traditionally, polarimetric bistatic radar cross section (RCS) measurements of point targets have been conducted using two disjoint dual-polarized antennas [10]. In this method, the transmitter and the target are often kept fixed and the receiver is moved on the surface of a sphere, having the target at its center, in order to measure the bistatic RCS at different bistatic angles (see Fig. 5.1). The difficulties associated with the traditional bistatic measurement technique can be categorized into three groups: (1) a complicated experimental setup is required, in which the scattered wave from the supporting structure must be minimized, (2) phase coherence between the transmitter and the receiver must be maintained as the microwave cables move with the receiving antenna, and (3) a complicated calibration procedure is needed to keep track of the orientation of the antennas with respect to the target.

To circumvent the problems associated with the traditional bistatic measurement technique, a new technique is proposed in which bistatic measurements are performed

on a point target using a wideband, polarimetric, monostatic radar in conjunction with a rotatable ground plane positioned behind the target. The new bistatic measurement technique can be applied to a wide range of problems. For example, it can be used as part of the CBSM technique to measure the effective propagation constant of dense random media. It can also be used to measure the bistatic scattering characteristics of individual scatterers of a tenuous random medium where the radiative transfer theory has been widely used. These bistatic scattering characteristics essential for estimating the extinction and phase function of the random media directly. In addition, the new bistatic measurement technique can be used to verify the proposed theoretical models for individual scatterers [49]-[43].

The coherent bistatic scattering measurement technique (CBSM) will be described in detail in chapter VI. In addition, it will be shown that the effective propagation constant of dense random media can be measured very accurately over a wide range of volume fractions. In chapter VII, measurements of the effective propagation constant of dense random media of different volume fractions, particle sizes, and permittivities will be presented and compared with existing analytical models.

The following section will be devoted to describing the new approach for measuring the bistatic scattering matrix of point targets. In this technique, a polarimetric monostatic radar in conjunction with a ground plane are used for the bistatic measurements and it is shown that the new technique circumvents the drawbacks of the traditional measurement technique. In Section 5.2, a system distortion model and an appropriate calibration procedure are developed for the proposed measurement setup. In order to fully characterize the bistatic scattering matrix, that is, to resolve the cross-polarized components, radar measurements must be repeated after loading the ground plane with an anisotropic layer. Two methods for designing the

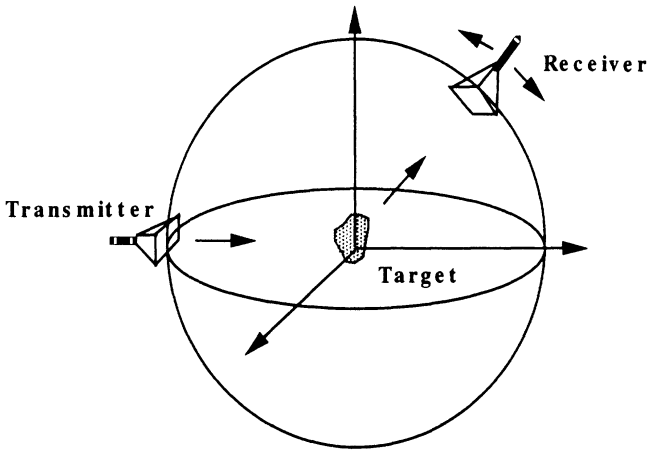

Figure 5.1: Experimental setup for the traditional bistatic scattering matrix measurement technique.

anisotropic dielectric layer required for loading the ground plane are discussed in Section 5.3. In Section 5.4, experimental data for canonical targets are presented to verify the accuracy of the new bistatic scattering matrix measurement technique.

5.1 Bistatic Scattering Measurement Technique

In this technique, a wideband, polarimetric, monostatic radar in conjunction with a rotatable perfectly conducting plane are used to measure the bistatic scattering matrix of a target. The simplified bistatic RCS measurement setup is shown in Fig 5.2. In this measurement configuration, the bistatic measurement can be performed in one scattering plane at a time. To change the scattering plane, the orientation of the target with respect to the radar system can be adjusted appropriately. In this method, the role of the ground plane is to excite the image wave (see Fig. 5.3) whose interactions with the target and its image produce the desired bistatic term. Primar-

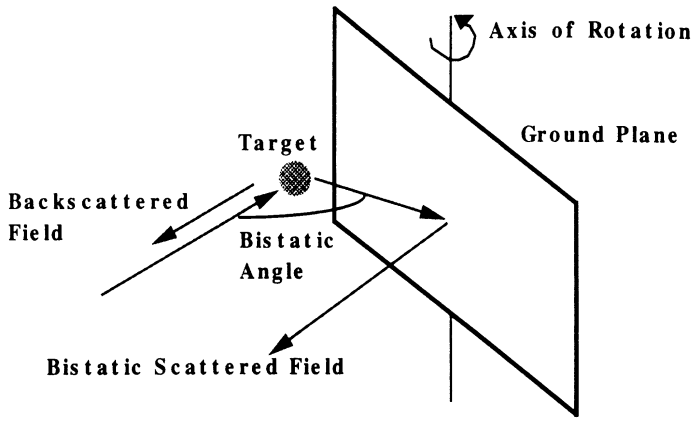

Figure 5.2: Experimental setup for the new bistatic scattering matrix measurement technique.

ily, there are three major scattering components that contribute to the signal received by the radar. However, their responses arrive at the antenna at different times. The first component is due to the direct backscatter from the target which arrives at the antenna with a delay time of $2r_1/c$, where c is the speed of light (see Fig. 5.3a). The second component, which in turn is comprised of two sub-components, is due to the bistatic scattering from the target being illuminated by the image wave (the long-dotted line in Fig. 5.3b) and its complementary which is the bistatic scattering from the image target illuminated by the image wave (the short-dotted line in Fig. 5.3b). These two sub-components arrive at the antenna with a delay time of $(r_1 + r_2 + r_3)/c$. The third component is due to the reflected backscattering of the image wave from the target through the ground plane which arrives at the antenna with a delay time of $2(r_2 + r_3)/c$. There are many higher order scattering terms which are the result of multiple scattering between the target and its image. The contribution of these terms to the overall backscattered signal is negligible if the distance

between the target and the ground plane, d_t, is much larger than the wavelength [37]. Experimentally, the effect of these terms can be reduced even further by placing an absorber on the ground plane between the target and its image, as illustrated in Fig. 5.3c. By choosing the distance between the target and the ground plane to be larger than the radar resolution, all components of the measured backscattered signal can be resolved and collected separately. For example, the magnitude of the total backscattered response from a sphere, measured in an anechoic chamber using a Network Analyzer-based monostatic radar, is plotted as a function of time and shown in Fig. 5.4a. In order to eliminate the undesired backscatter from the edges of the ground plane, the backscatter response of the ground plane alone (without the target) was subtracted coherently from the backscatter response of the ground plane and the target. The first peak in Fig. 5.4a corresponds to the direct backscatter component (DB) while the second peak corresponds to the total bistatic component (BIS) (the two complementary sub-components) and the third peak corresponds to the indirect backscatter component (IB). Since the three components of the backscatter response arrive at the antenna at different times, the BIS component can be isolated from the others using the range gating capability of the Network Analyzer. The gated bistatic response is shown in Fig. 5.4b.

The second component of the scattered signal contains the desired bistatic scattering response of the target. By defining a set of orthogonal directions ($\hat{v}$, $\hat{h}$) in a plane perpendicular to the direction of propagation, the bistatic scattered signal $\bar{\mathbf{E}}_\mathbf{b}$ can be related to the incident signal through the total measured bistatic scattering matrix, i.e.

$$\bar{\mathbf{E}}_\mathbf{b} = \frac{e^{-i\,k_o\,r_o}}{r_o} \quad \bar{\bar{\mathbf{S}}}_\mathbf{b} \quad \bar{\mathbf{E}}_\mathbf{i} \tag{5.1}$$

where k_o is the free space propagation constant and $\bar{\bar{\mathbf{S}}}_\mathbf{b}$ is the total measured bistatic

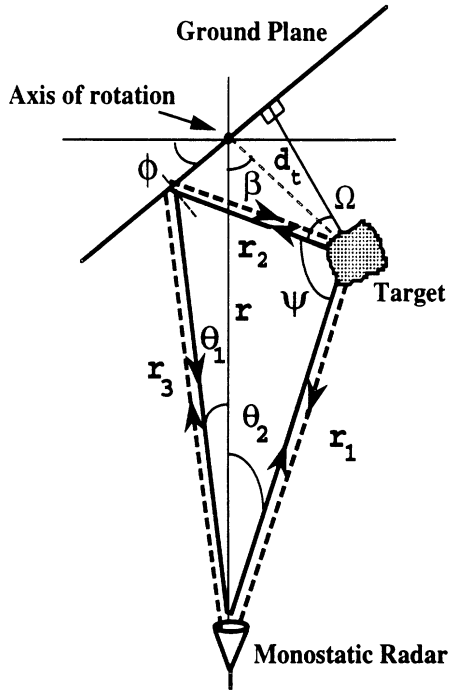

(a)

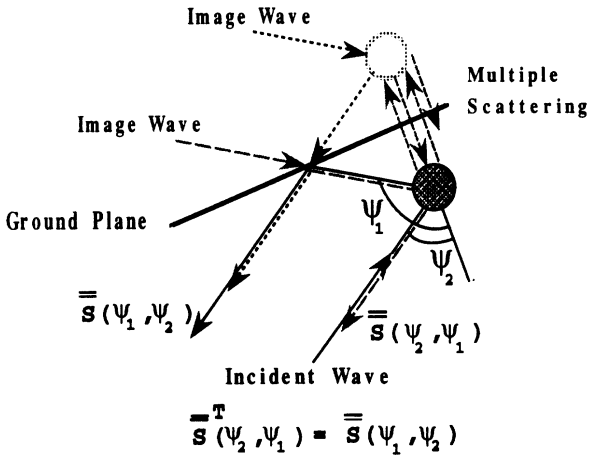

(b)

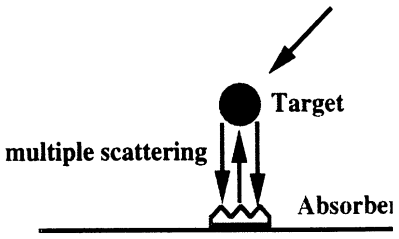

(c)

Figure 5.3: Scattering configuration in the presence of a ground plane, the new experimental setup illustrating (a) top view of the measurement setup, (b) the interactions of the image waves with the target and its image, and (c) application of a radar absorber to minimize the effect of multiple scattering between the target and its image.

scattering matrix. The total bistatic scattering matrix is a function of the desired scattering matrices of the two complementary sub-components, $\bar{\bar{\mathbf{S}}}(\Psi_1,\ \Psi_2)$ and $\bar{\bar{\mathbf{S}}}(\Psi_2,\ \Psi_1)$, and the reflectivity matrix of the ground plane ($\bar{\bar{\Gamma}}$) as shown in Fig. 5.5. In the most general case, corresponding to an anisotropic surface, $\bar{\bar{\Gamma}}$ is a 2×2 matrix whose entries are the reflection coefficients of the ground plane. Since the two sub-components (bistatic terms) arrive at the same time, they cannot be resolved in the time domain and the target's bistatic scattering matrices $\bar{\bar{\mathbf{S}}}(\Psi_1,\ \Psi_2)$ and $\bar{\bar{\mathbf{S}}}(\Psi_2,\ \Psi_1)$ cannot be uniquely determined. The reciprocity theorem mandates that $\bar{\bar{\mathbf{S}}}(\Psi_1,\ \Psi_2) = \bar{\bar{\mathbf{S}}}^{\mathbf{T}}(\Psi_2,\ \Psi_1)$ and $\bar{\bar{\Gamma}} = \bar{\bar{\Gamma}}^{\mathbf{T}}$. Thus, the total measured bistatic scattering matrix given by

$$\bar{\bar{\mathbf{S}}}_{\mathbf{b}} = \frac{e^{-ik_o r_o}}{r_o}\left(\bar{\bar{\Gamma}}\ \bar{\bar{\mathbf{S}}}(\Psi_1,\ \Psi_2) + [\ \bar{\bar{\Gamma}}\ \bar{\bar{\mathbf{S}}}(\Psi_1,\ \Psi_2)\ ]^{\mathbf{T}}\right) \tag{5.2}$$

is symmetric. This poses a difficulty in characterizing the desired bistatic scattering matrix $\bar{\bar{\mathbf{S}}}$ in that there are only three independent equations for the four unknown elements of the bistatic scattering matrix $\bar{\bar{\mathbf{S}}}$. To resolve this ambiguity, an additional measurement is needed in which the target's orientation and position remain the same while the reflective property of the ground plane is changed. This is achieved by placing an anisotropic lossless layer over the perfectly conducting plane.

In summary, the measurement procedure involves three steps starting with positioning the point target in front of the ground plane at an appropriate distance. Then the ground plane is rotated to the desired bistatic angle and the second component of the backscattered signal is measured. Finally, the second step is repeated for the same bistatic angles after attaching the anisotropic slab to the ground plane.

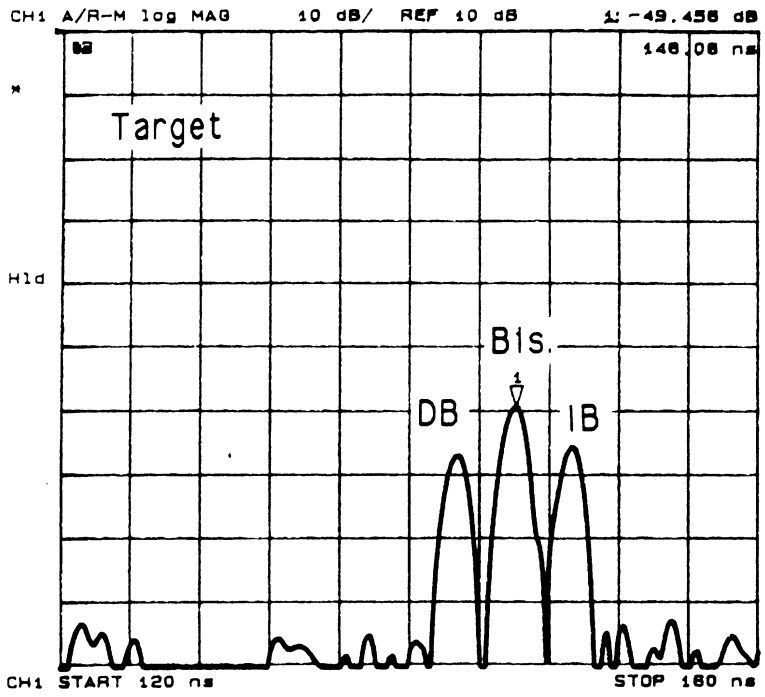

(a)

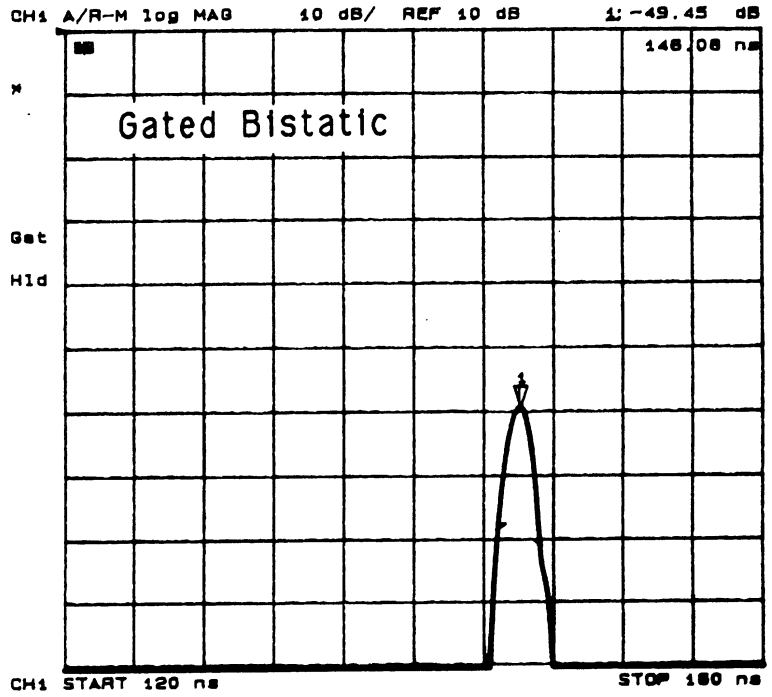

(b)

Figure 5.4: A time domain response of a target in the presence of a ground plane (a) the three major components of the measured signal, (b) the gated bistatic component.

5.2 Calibration Technique

Characterization of measurement accuracy and precision are the critical elements of any meaningful measurement procedure. Imperfections in the radar system components, such as antenna polarization contamination (coupling between the orthogonal polarization ports of the antenna) and channel imbalances (variations in magnitude and phase of the system transfer function for different ports of the receiver) can lead to serious errors in the measured scattering matrix. The role of a calibration procedure is then to remove the systematic errors from the measured target response. In this section, the imperfections of the monostatic radar system is modelled mathematically and a procedure for determining the system distortion parameters is outlined. In this technique, a metallic sphere is used as the external calibration target and the radar distortions are obtained using a mathematical model.

5.2.1 System Distortion Model

Depending on the distance between the target and the radar, the direction of the transmitted and received rays with respect to the antenna's boresight can be quite different. The complementary bistatic terms propagate along directions defined by angles θ_1 and θ_2, as shown in Fig. 5.3a. These rays experience different transfer functions since the systematic errors vary over the mainlobe of the antenna. Thus, it is important to: first, characterize the systematic errors of the radar antenna over its mainlobe and construct a system distortion model; and second, remove these errors from the measured bistatic response using an appropriate calibration procedure. The proposed system distortion model is an extension of the model developed for single-antenna polarimetric radars [40]. In this paper [40], it is shown that the measured

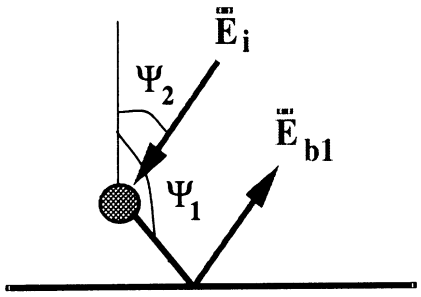

$$\bar{\bar{E}}_{b1} = \frac{e^{-i\,k_o r_o}}{r_o}\ \bar{\bar{\Gamma}}\ \bar{\bar{S}}\ (\Psi_1, \Psi_2)\ \bar{\bar{E}}_i$$

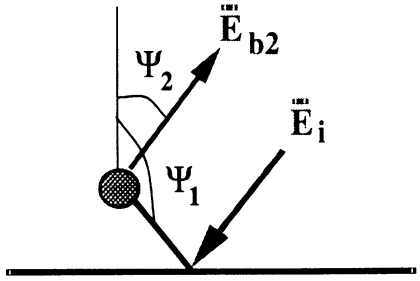

$$\bar{\bar{E}}_{b2} = \frac{e^{-i\,k_o r_o}}{r_o}\ \bar{\bar{S}}\ (\Psi_2, \Psi_1)\ \bar{\bar{\Gamma}}^T\ \bar{\bar{E}}_i$$

Figure 5.5: The two complementary sub-components of the bistatic response.

scattering matrix ($\bar{\bar{\mathbf{M}}}$) of a point target in terms of the actual scattering matrix and the radar distortions can be obtained from

$$\bar{\bar{\mathbf{M}}} = \frac{e^{-2ikr}}{r^2} \; \bar{\bar{\mathbf{R}}} \;\; \bar{\bar{\mathbf{D}}}(\theta_o) \;\; \bar{\bar{\mathbf{C}}}(\theta_o) \;\; \bar{\bar{\mathbf{S}}} \;\; \bar{\bar{\mathbf{C}}}(\theta_o) \;\; \bar{\bar{\mathbf{D}}}(\theta_o) \;\; \bar{\bar{\mathbf{T}}} \,, \tag{5.3}$$

where θ_o is an angle representing the position of the target with respect to the antenna. In (5.3), $\bar{\bar{\mathbf{R}}}$, $\bar{\bar{\mathbf{T}}}$, $\bar{\bar{\mathbf{C}}}$, and $\bar{\bar{\mathbf{D}}}$ are 2×2 matrices representing the radar distortions and are given by

$$\bar{\bar{\mathbf{R}}} = \begin{bmatrix} R_v & 0 \\ 0 & R_h \end{bmatrix}, \quad \bar{\bar{\mathbf{T}}} = \begin{bmatrix} T_v & 0 \\ 0 & T_h \end{bmatrix}$$

$$\bar{\bar{\mathbf{C}}} = \begin{bmatrix} 1 & c \\ c & 1 \end{bmatrix}, \quad \bar{\bar{\mathbf{D}}} = \begin{bmatrix} d_1 & 0 \\ 0 & d_2 \end{bmatrix} \quad .$$

Here the parameters (T_v, T_h) and (R_v, R_h) are the channel imbalances due to the active components in the transmit and receive branches of the radar respectively, $c(\theta_o)$ is the antenna cross-talk factor, and $(d_1(\theta_o), d_2(\theta_o))$ are the channel imbalances of the antenna system. It should be noted that the channel imbalance parameters are independent of the target angle θ_o. As mentioned before, the measured bistatic scattering matrix is comprised of two complementary components that arrive at the radar simultaneously and thus are inseparable in the time domain. These components are designated by the solid and dotted lines in Fig. 5.3a. The system distortion model described in (5.3) is modified to include the possible differences in the radar distortion parameters for the transmit and receive rays. Thus, the distortion model for the

second component of the measured radar response is given by:

$$\bar{\bar{\mathbf{M}}} = \frac{e^{-ik(r_1+r_2+r_3)}}{r_1(r_2+r_3)} \bar{\bar{\mathbf{R}}} \left\{ \bar{\bar{\mathbf{D}}}(\theta_2) \;\; \bar{\bar{\mathbf{C}}}(\theta_2) \;\; \bar{\bar{\mathbf{S}}}^{\mathbf{T}}(\psi_1,\psi_2) \;\; \bar{\bar{\Gamma}}^{\mathbf{T}} \;\; \bar{\bar{\mathbf{C}}}(\theta_1) \;\; \bar{\bar{\mathbf{D}}}(\theta_1) \right.$$
$$\left. + \bar{\bar{\mathbf{D}}}(\theta_1) \;\; \bar{\bar{\mathbf{C}}}(\theta_1) \;\; \bar{\bar{\Gamma}} \;\; \bar{\bar{\mathbf{S}}}(\psi_1,\psi_2) \;\; \bar{\bar{\mathbf{C}}}(\theta_2) \;\; \bar{\bar{\mathbf{D}}}(\theta_2) \right\} \bar{\bar{\mathbf{T}}} \quad (5.4)$$

The first term in the bracket corresponds to the bistatic scattering of the target when illuminated by the image wave and the second term corresponds to the bistatic scattering of the image target when illuminated by the image wave. It should be noted that in the derivation of equation (5.4), the reciprocity theorem has been used to express the bistatic scattering matrix of the target when illuminated by the image wave $\bar{\bar{\mathbf{S}}}(\psi_2,\psi_1)$ in terms of the scattering matrix of the target when illuminated by the incident wave $\bar{\bar{\mathbf{S}}}(\psi_1,\psi_2)$ ($\bar{\bar{\mathbf{S}}}(\psi_2,\psi_1) = \bar{\bar{\mathbf{S}}}^{T}(\psi_1,\psi_2)$). Once the radar distortion parameters are determined, the elements of the bistatic scattering matrix $\bar{\bar{\mathbf{S}}}$ can be computed by inverting equation (5.4). These unknown terms can be determined by measuring the polarimetric response of a metallic sphere in the backscattering configuration over the entire mainlobe of the antenna (no ground plane). By applying the single target calibration technique (STCT) [40], the cross-talk factors and channel imbalances can be determined from the polarimetric sphere measurements ($\bar{\bar{\mathbf{M}}}^{s}$) and are given by

$$c(\theta_o) = \pm\frac{1}{\sqrt{a}}\,(1-\sqrt{1-a}), \qquad a = \frac{m^s_{vh}\, m^s_{hv}}{m^s_{vv}\, m^s_{hh}}$$

$$\sqrt{R_v\, T_v}\, d_1(\theta_o) = r_s\, e^{ikr_s} \sqrt{\frac{m^s_{vv}/s_o}{1+c^2(\theta_o)}}$$

$$\sqrt{R_h\, T_h}\, d_2(\theta_o) = r_s\, e^{ikr_s} \sqrt{\frac{m^s_{hh}/s_o}{1+c^2(\theta_o)}}$$

$$\sqrt{\frac{R_v T_h}{R_h T_v}} = \sqrt{\frac{m^s_{vh}}{m^s_{hv}}} \tag{5.5}$$

In (5.5), the superscript s refers to the measured sphere response, s_o is the theoretical backscattering amplitude of the metallic sphere, and θ_o can be either θ_1 or θ_2. It should be noted that the antenna's distortion parameters (c, d_1, and d_2) are time invariant and therefore the elaborate backscatter measurement of the metallic sphere over the entire mainlobe of the antenna must be performed only once. However, elements of $\bar{\bar{\mathbf{R}}}$ and $\bar{\bar{\mathbf{T}}}$ which are influenced by the active elements of the radar must be characterized often. This can be done by measuring a sphere positioned at the boresight of the antenna noting that the elements of $\bar{\bar{\mathbf{R}}}$ and $\bar{\bar{\mathbf{T}}}$ are independent of the target angle θ_o. Once the distortion parameters at boresight are determined, the expressions given by (5.5) must be modified by the following factors in order to update the distortion parameters over the entire mainlobe

$$\alpha_1 = \frac{\left(\sqrt{R'_v\, T'_v}\; d_1(0^o)\right)}{\left(\sqrt{R_v\, T_v}\; d_1(0^o)\right)}, \qquad \alpha_2 = \frac{\left(\sqrt{R'_h\, T'_h}\; d_2(0^o)\right)}{\left(\sqrt{R_h\, T_h}\; d_2(0^o)\right)}, \qquad \alpha_3 = \sqrt{\frac{R'_v\, T'_h}{R'_h\, T'_v}} \;/\; \sqrt{\frac{R_v\, T_h}{R_h\, T_v}}$$

where the primed parameters (R'_v, R'_h, T'_v, T'_h) correspond to the last sphere measurement at boresight.

For the sake of completeness, expressions for r_1, r_2, r_3, θ_1, θ_2, and Ψ in terms of the physical setup parameters r, β, d_t, and ϕ, as defined in Fig. 5.3a, are provided below

$$r_1 = \sqrt{d_t^2 + r^2 - 2\, d_t\, r\, \cos\beta},$$

$$
\begin{aligned}
\theta_2 &= \sin^{-1}\left[\frac{d_t}{r_1}\sin\beta\right], \\
(r_2+r_3) &= \sqrt{(2x)^2 + r_1^2 - 4\,x\,r_1\,\cos(\pi-\theta_2-\phi)} \\
\theta_1 &= -\theta_2 + \sin^{-1}\left[\frac{2x}{(r_2+r_3)}\sin(\pi-\theta_2-\phi)\right] \\
\Omega &= \sin^{-1}\left[\frac{r_1}{(r_2+r_3)}\sin(\pi-\theta_2-\phi)\right] \\
r_2 &= \frac{x}{\cos\Omega} \\
\Psi &= \pi - (\theta_1+\theta_2) - 2\,\Omega
\end{aligned}
$$

where $x = d_t\,\cos(\phi-\beta)$. Refering to Fig. 5.3a, r is the distance between the antenna and the axis of rotation of the ground plane, ϕ denotes the rotation angle of the ground plane, and β and d_t specify the target's position relative to the ground plane. It is noted that the bistatic angle (Ψ) and the direction of propagation of the bistatic response (θ_1) can be computed in terms of the rotation angle of the ground plane (ϕ).

5.2.2 Calibration Procedure

Following simple algabraic manipulations, equation (5.4) can be cast into a matrix equation of the following form

$$\bar{\bar{\mathbf{A}}}\,\bar{\mathbf{x}} = \bar{\mathbf{b}} \tag{5.6}$$

where $\bar{\mathbf{b}} = [\, m_{vv}, m_{hh}, m_{vh}, m_{hv}\,]^T$, $\bar{\mathbf{x}} = [\, S_{vv}, S_{hh}, S_{vh}, S_{hv}\,]^T$, and $\bar{\bar{\mathbf{A}}}$ is a 4×4 matrix whose elements are a function of the radar distortion parameters and the elements of $\bar{\bar{\Gamma}}$. Having determined the elements of $\bar{\bar{\mathbf{A}}}$ from the external calibration, it seems, the elements of the bistatic scattering matrix can be obtained by inverting (5.6). However, the last two rows of (5.6) are linearly dependent and in effect only three linearly independent equations are available. Therefore, one of the dependent equations in (5.6) must be replaced by another independent equation acquired by repeating the

experiment after loading the ground plane with an anisotropic dielectric layer. It should be noted that the second bistatic measurement (with loaded ground plane) is not necessary for targets that do not depolarize ($S_{vh} = S_{hv} = 0$) such as spheres and vertical and horizontal cylinders. In this case, the linear system of equations in (5.6) reduces to two independent equations for the two unknowns (S_{vv}, S_{hh}). After some algabraic manipulations, it can be shown that

$$\begin{aligned} S_{vv} &= \frac{z_{vv} - c(\theta_1)\, c(\theta_2)\, z_{hh}}{\Gamma_v\, (1 - c^2(\theta_1)\, c^2(\theta_2))} \\ S_{hh} &= \frac{z_{hh} - c(\theta_1)\, c(\theta_2)\, z_{vv}}{\Gamma_h\, (1 - c^2(\theta_1)\, c^2(\theta_2))} \end{aligned} \tag{5.7}$$

where

$$\begin{aligned} z_{vv} &= \frac{e^{ik(r_1+r_2+r_3)}\, r_1\, (r_2 + r_3)}{2\, R_v\, T_v\, d_1(\theta_1)\, d_1(\theta_2)} \quad m_{vv} = \Gamma_v\, S_{vv} + \Gamma_h\, c(\theta_1)\, c(\theta_2)\, S_{hh} \\ z_{hh} &= \frac{e^{ik(r_1+r_2+r_3)}\, r_1\, (r_2 + r_3)}{2\, R_h\, T_h\, d_2(\theta_1)\, d_2(\theta_2)} \quad m_{hh} = \Gamma_h\, S_{hh} + \Gamma_v\, c(\theta_1)\, c(\theta_2)\, S_{vv} \end{aligned} \tag{5.8}$$

5.3 Design of an Anisotropic Surface

In order to acquire an additional independent measurement to resolve the ambiguity in the measurement of the cross-polarized components, use of an anisotropic dielectric slab to modify the reflection matrix $\bar{\bar{\Gamma}}$ is required. Since the magnitude of the second component of the received signal (the bistatic term) is proportional to the reflection coefficient, the magnitude of the reflection coefficient of the surface must

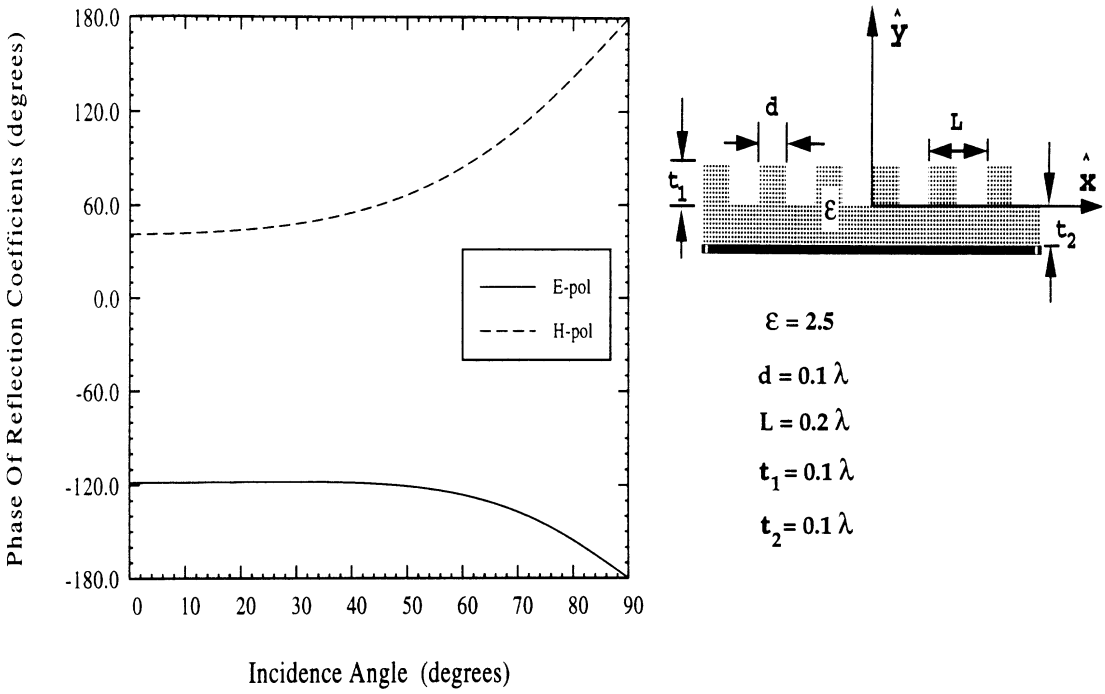

(a)

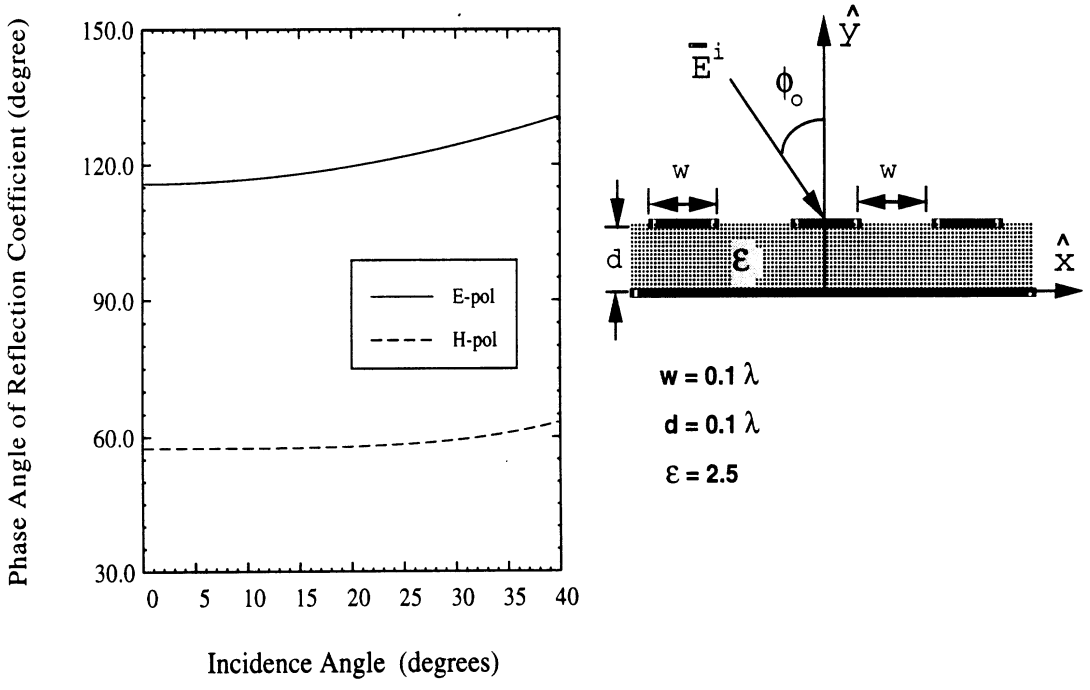

(b)

Figure 5.6: Phases of the reflection coefficients for periodic corrugated dielectric slab (a), and dielectric loaded periodic strips (b) as functions of the incidence angle.

be chosen as high as possible in order to retain the system sensitivity. Therefore, an anisotropic surface with reflection coefficients having magnitude of unity, similar to those of the perfectly conducting plane, and phases that are very different from those of the ground plane are of interest. Two types of surfaces are considered in this paper to accomplish this task: (1) loading the ground plane by a periodic corrugated dielectric slab, and (2) loading the ground plane by dielectric loaded periodic strips. If lossless dielectric materials are used, the magnitude of the reflection coefficients will be unity.

5.3.1 Periodic Corrugated Dielectric Slab

The proposed one-dimensional periodic surface is shown in Fig. 5.6a. It has been demonstrated that a periodic corrugated dielectric layer can be simulated by an anisotropic dielectric layer of equal thickness when the period is small compared to the wavelength [41]. The tensor elements of the equivalent anisotropic layer are given in terms of the permittivity (ϵ), the period of surface corrugation (L), and the width of the corrugation (d). In the low frequency regime, where $L < 0.2\lambda$, the tensor elements are given by

$$\begin{aligned} \epsilon_y &= \epsilon_z = 1 + (\epsilon - 1)\frac{d}{L} \\ \epsilon_x &= \frac{\epsilon}{\epsilon(1 - d/L) + d/L} \end{aligned} \tag{5.9}$$

The reflection coefficients of the stratified loaded ground plane can easily be computed [41]. The higher order Bragg modes decay exponentially away from the surface in the low frequency regime (L $< 0.5\lambda$), thus the target must be placed far enough from the surface to avoid coupling with the higher order Bragg modes. By appro-

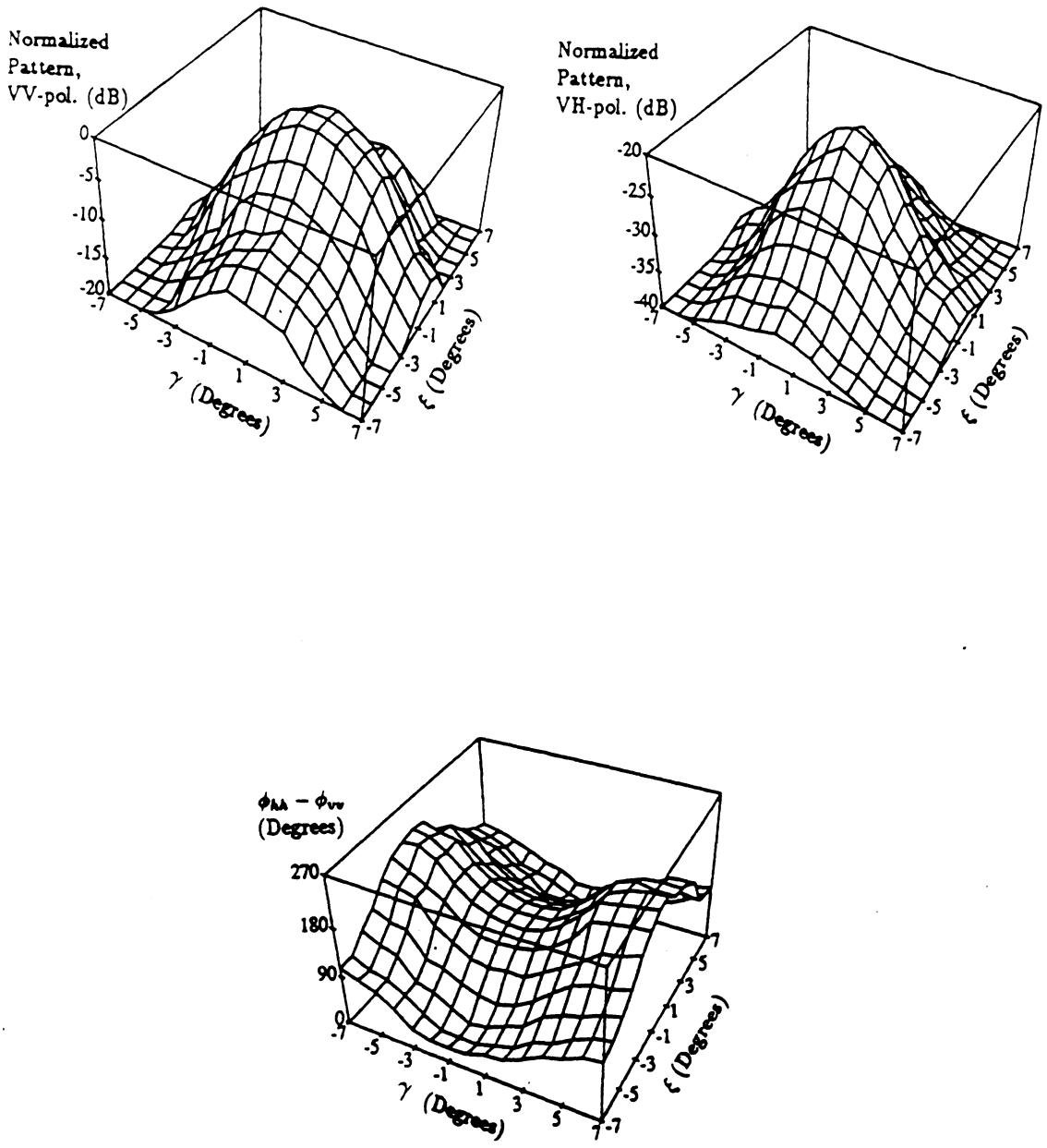

Figure 5.7: Measured backscattered response from a sphere over the entire mainlobe of the monstatic radar.

priately choosing the permittivity of the dielectric, the width, period, and depth of the corrugated layer, the desired phase-difference between the reflection coefficients can be achieved. For example, the phases of the reflection coefficients as functions of the incidence angle when $\epsilon = 2.5$, $d = 0.1\lambda$, $L = 0.2\lambda$, $t_1 = 0.1\lambda$, and $t_2 = 0.1\lambda$ at 9.5 GHz are shown in Fig. 5.6a.

5.3.2 Dielectric Loaded Periodic Strips

The surface with dielectric loaded periodic strips also behaves as an anisotropic layer and is shown in Fig. 5.6b. In this structure, perfectly conducting strips of width w are periodically aligned over a dielectric substrate with permittivity ϵ and thickness d backed by a ground plane. The scattered plane waves can be computed from

$$\bar{\mathbf{E}}^s(x,y) = \int_{-w/2}^{w/2} \bar{\bar{\mathbf{G}}}^p(x,x') \cdot \bar{\mathbf{J}}(x')\, dx' \tag{5.10}$$

where $\bar{\mathbf{J}}$ is the current distribution over a strip and $\bar{\bar{\mathbf{G}}}^p$ is the 2-D periodic dyadic Green's function. The details of deriving $\bar{\bar{\mathbf{G}}}^p$ can be found in [42]. By enforcing the boundary conditions on the surface of the strip, that is, $\hat{y}\times\left(\bar{\mathbf{E}}^i + \bar{\mathbf{E}}^r\right) = -\hat{y}\times\bar{\mathbf{E}}^s$, an integral equation for the unknown current distribution can be obtained. The electric field $\bar{\mathbf{E}}^i$ refers to the incident plane wave and $\bar{\mathbf{E}}^r$ refers to the field reflected from the stratified medium in the absence of the strips. The current can be computed by solving the integral equation using the method of moments. Once the surface current on the strip is determined, the scattered electric and magnetic fields, as well as the

reflection coefficients for TE and TM polarizations can be computed from

$$\Gamma_E = \frac{E_z^r + E_z^s}{E_z^i}, \qquad \Gamma_H = \frac{H_z^r + H_z^s}{H_z^i} \tag{5.11}$$

where Γ_E and Γ_H are the reflection coefficients for TM and TE polarizations, respectively. As before, when $w < 0.5\lambda$ only the zeroth order Bragg mode is propagating. The phases of Γ_E and Γ_H of the dielectric loaded periodic strips are shown in Fig. 5.6b at 9.5 GHz when $d = w = 0.1\,\lambda$ and $\epsilon = 2.5$.

5.4 Experimental Verification

To demonstrate the accuracy of the new bistatic measurement technique, the measured bistatic responses of three canonical targets (two metallic spheres with different diameters and a tilted metallic cylinder), are compared with their theoretical bistatic responses. A Network Analyzer-based, polarimetric, monostatic radar was used in these measurements [51]. The radar operates at 9.5 GHz with a 1.5 GHz bandwidth which corresponds to a spatial resolution of about 10 cm. A perfectly conducting circular disc with diameter 1.2 m was used as the ground plane. The ground plane was positioned inside an anechoic chamber at a distance $r = 15$ m away from the radar system and the target was located at $\beta = 45^o$ and $d_t = 0.6$ m with respect to the ground plane as depicted in Figs. 5.2 and 5.3. Precise rotation of the ground plane was facilitated using a computer-controlled stepper motor. To characterize the system distortion parameters of the radar system, polarimetric measurements of a metallic sphere (without a ground plane) were conducted over the entire main lobe of the antenna system. The measured backscatter response of the sphere for the X-band radar is shown in Fig. 5.7 in an azimuth-over-elevation coordinate system (γ, ξ).

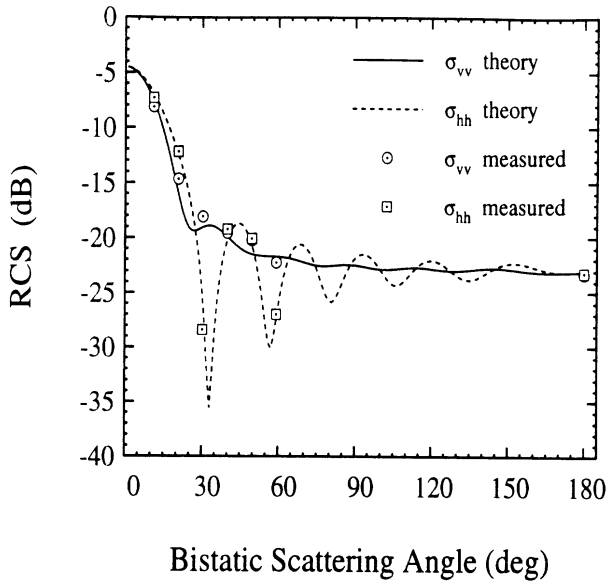

(a)

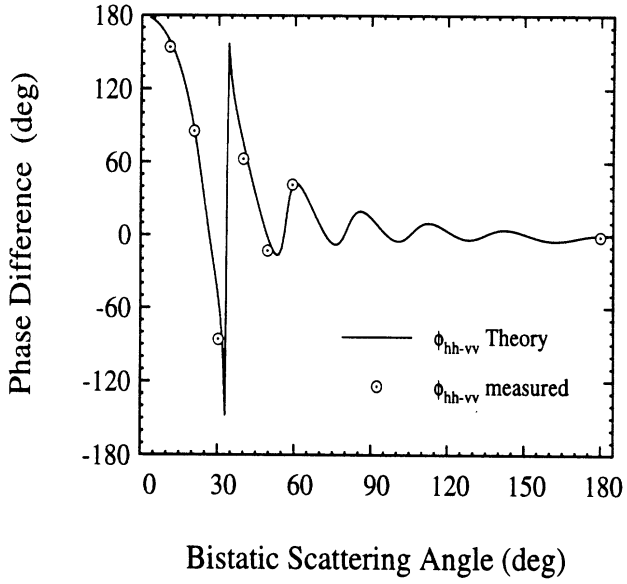

(b)

Figure 5.8: The magnitude (a) and phase-difference (b) of the bistatic scattering matrix elements of the 8.1 cm metallic sphere.

Two metallic spheres with diameters 4.45 cm and 8.1 cm were measured and compared with their theoretical responses over a number of bistatic angles including the backscatter direction in order to demonstrate the capability of the calibration technique in removing the systematic errors. As mentioned before, the spurious responses of the finite ground plane were removed by subtracting the backscatter response of the ground plane in the absence of the target from that of the combination of the target and the ground plane. Figures 5.8 and 5.9 show the measured and computed bistatic radar cross sections (σ_{vv} and σ_{hh}) and the co-polarized phase difference (ϕ_{hh-vv}) of the 4.45 cm and 8.1 cm spheres respectively. The measured bistatic radar cross sections and phase differences, for both spheres, were, respectively, within ± 0.5 dB and $\pm 5^{\circ}$ of the theoretical computations.

Spheres are nondepolarizing targets and in their measurments the anisotropic dielectric layer was not used. Next, the bistatic scattering matrix of a tilted metallic cylinder was measured to demonstrate the accuracy and feasibility of measuring the cross-polarized components of the scattering matrix. The length and diameter of the metallic cylinder were 15 cm and 1.5 cm respectively. The cylinder was positioned in a plane perpendicular to the direction of propagation of the incident wave with a tilt angle of 30° with respect to the vertical direction. A set of measurements were conducted first with the perfectly conducting plane as the reflecting surface. Then, the measurements were repeated after overlaying the dielectric loaded periodic strips slab (DLPS) on the ground plane. The DLPS slab was oriented so that its strips were aligned along the vertical direction. The phases of the reflection coefficients of the DLPS slab were computed from the method of moments solution and used in the calibration procedure. The method of moments phase calculation for the reflection coefficients was verified experimentally by measuring the phase difference between the

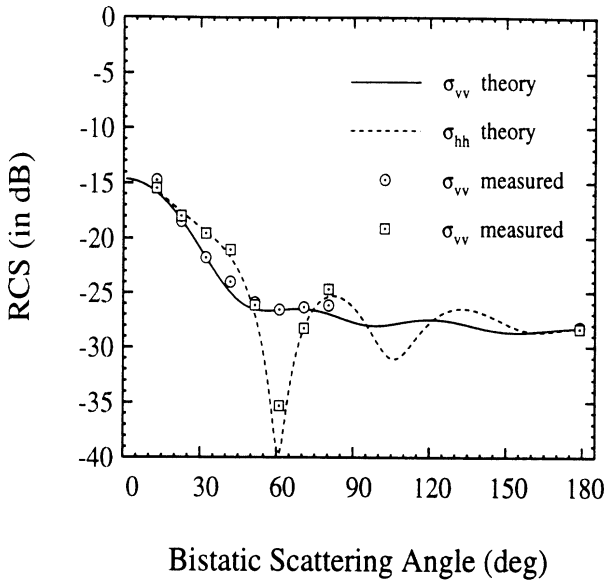

(a)

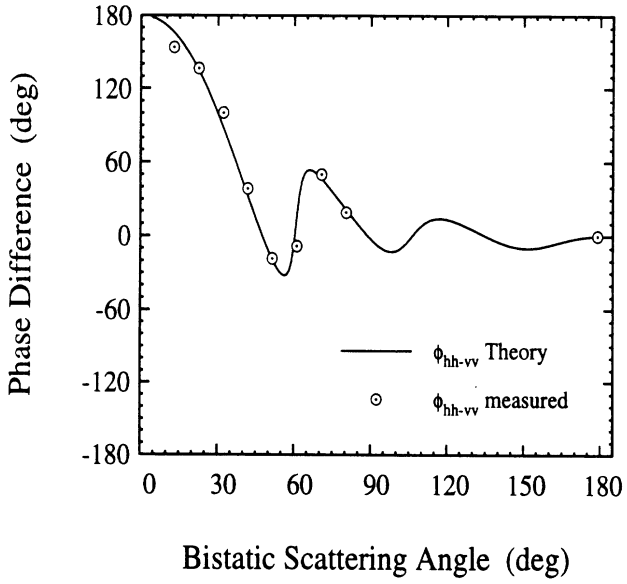

(b)

Figure 5.9: The magnitude (a) and phase-difference (b) of the bistatic scattering matrix elements of the 4.45 cm metallic sphere.

reflection coefficients of the vertical and horizontal polarizations at normal incidence. The bistatic scattering matrix of the tilted cylinder was computed numerically using the method of moments specialized for scatterers with axial symmetry (body of revolution) [28]. As shown in Fig. 5.10, excellent agreement was obtained between the theoretically computed and the measured bistatic cross sections (σ_{vv}, σ_{hh}, σ_{hv}, and σ_{vh}) and the co-polarized phase difference (ϕ_{hh-vv}) of the tilted cylinder.

5.5 Conclusions

A convenient technique for the bistatic scattering measurement of point targets was developed. In this technique, a monostatic radar with fine spatial resolution in conjunction with a rotatable ground plane were used to measure the bistatic scattering matrix. The new technique circumvents some limiting aspects of the traditional measurement technique. For example, since the transmitter, receiver, and the target are stationary, retaining the phase-coherence is no longer a problem (no moving cables) and a very accurate calibration can be performed. Also, construction of a complicated bistatic measurement setup for supporting and positioning the transmit and receive antennas with respect to the target is avoided. It was shown that for depolarizing targets, an independent radar measurement after loading the ground plane with a dielectric slab is required for determining the cross-polarized components of the bistatic scattering matrix. The accuracy of the new method was demonstrated by comparing the measured bistatic scattering matrices of cylinders and spheres with the theoretical ones over a wide range of scattering angles.

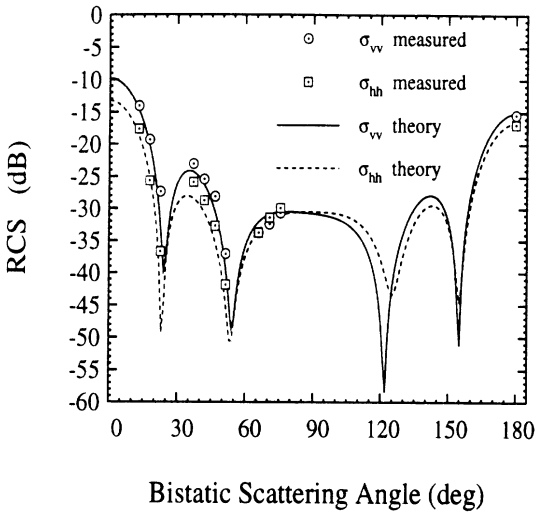

(a)

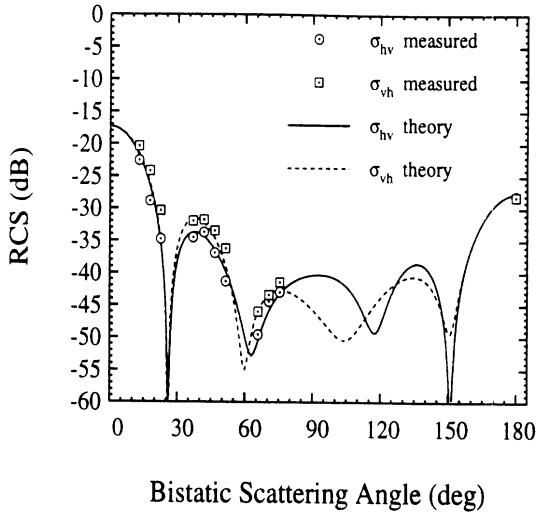

(b)

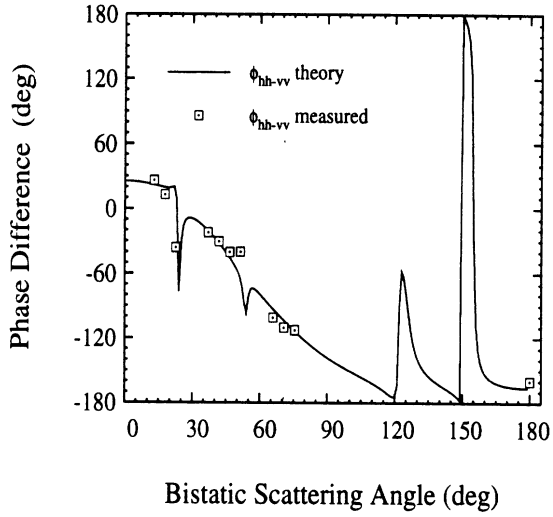

(c)

Figure 5.10: The magnitude (a, b) and phase-difference (c) of the bistatic scattering matrix elements of a tilted (30° from vertical) metallic cylinder with length 15 cm and diameter 1.5 cm .

CHAPTER VI

A NEW TECHNIQUE FOR MEASUREMENT OF EFFECTIVE PROPAGATION CONSTANT OF RANDOM MEDIA

We have developed in the previous chapter a new technique for measuring accurately the bistatic scattering matrix of a point target using a wide band, polarimetric, monostatic radar in conjunction with a rotatable ground plane positioned behind the point target.

In this chapter, our objective is to develop an accurate and convenient method to measure the effective propagation constant of a random media, thereby establishing a benchmark that can be used for characterization of the validity region of the existing analytical models. Besides the benchmarking purpose, the measurement technique may be used for the developement of empirical models for the effective propagation constant of random media of interest.

6.1 Introduction

The literature concerning experimental characterization of the effective propagation constant of random media is rather scarce. In general the measurement technique

can be categorized into low- and high-frequency approaches. In low frequencies when the particle dimensions are much smaller than the wavelength, standard dielectric measurement techniques can be used to measure K [20]-[31] . At high frequencies, the standard approach is the free space transmission measurement technique (FSTM) [27]-[17]. In this technique, a slab of the dense random medium is positioned between two antennas and the transmission coefficient is measured coherently (see Fig. 6.1). By moving the slab and measuring the transmission coefficient repeatedly, the mean transmission coefficient is computed from which the effective propagation constant of the random medium is calculated. Calculation of the effective propagation constant from the measured mean transmission coefficient is rather straightforward for random media with low fractional volume ($f \leq 0.10$) where diffuse boundaries for the slab can be assumed. However, at higher fractional volumes, the slab boundaries can no longer be assumed diffusive and multiple reflections of the mean-field between the slab boundaries must to be included in the analysis. Although the measurement of the effective propagation constant using the FSTM technique is simple in principle, the accuracy of the measurement technique is limited by a number of practical difficulties. One difficulty pertains to maintaining the phase coherency between the receiver and transmitter during the measurement. Since in this configuration the slab of the random media is positioned in the far field region of both transmitter and receiver, phase coherency must be maintained using a long microwave cable. Hence, any cable movement during measurements could result in loss of phase coherency. Furthermore, a large slab is required in order to minimize the undesirable scattering effects from the edges of a finite slab. This leads to difficulties in handling targets with high volume fractions (weight constraints), and in generating many independent samples of the random medium. Another drawback of the FSTM method stems from

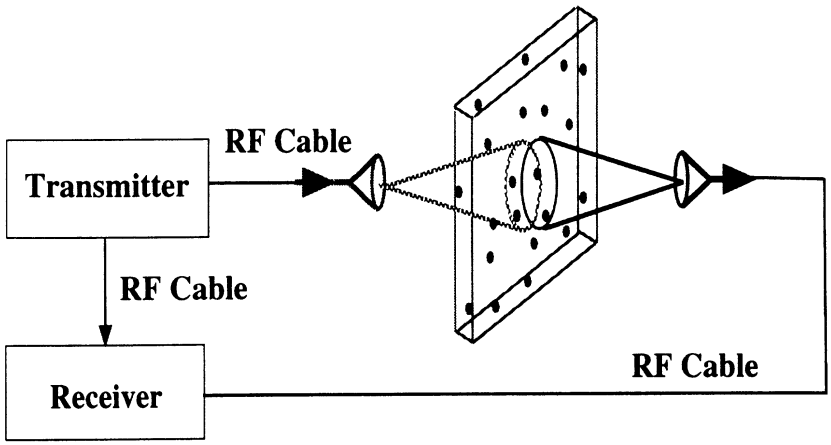

Figure 6.1: Simplified experimental setup using the free space transmission measurement system.

the fact that the effective propagation constant must be computed from a single measured parameter of the medium, namely, the mean transmission coefficient. Hence, the accuracy of the measurement of K is severely limited by the systematic errors. The accuracy in the evaluation of K using this method decreases for dense random media with significant extinction rate.

In this chapter we present the new approach for the measurement of the effective propagation constant of dense random media which circumvents most of the aforementioned difficulties of the standard FSTM approach. In the following section, the new measurement technique is described and practical issues such as measurement accuracy and sensitivity analysis are discussed. In Section 6.3, the validity of the measurement technique is demonstrated by performing experiments for random media for which the effective propagation constant is known.

6.2 Coherent Bistatic Scattering Measurement Technique (CBSM)

In this section, a new measurement technique for characterizing the effective propagation constant of a dense random medium is presented. First, a cluster of constituent particles of the random medium is confined in a rotationally symmetric geometry such as a sphere or cylinder. Then the co-polarized bistatic scattering amplitudes, S_{vv} and S_{hh}, of the cluster are measured over many bistatic scattering angles (θ) in a single scattering plane, as shown in Fig. 6.2a.. At each bistatic angle, the radar measurements are performed over many independent realizations of the random medium, from which the coherent and incoherent components of the scattered amplitudes are computed. Independent bistatic measurements for a given bistatic angle can be realized by simply rotating the cluster of the random medium about its axis of symmetry. To evaluate the effective propagation constant of the dense random medium, the measured mean bistatic scattering amplitudes are fitted to the bistatic scattering pattern of a homogeneous dielectric material having the same geometrical boundary. Towards this end, a constrained search routine, such as the FSQP optimization routine [74], can be used to minimize the difference between the measured and theoretical responses. With the real and imaginary parts of K acting as free parameters, the following error function is minimized

$$E = \sum_{l=1}^{M}\sum_{i=1}^{N}\left[\left|\frac{s_{vv}^{m}(i,l) - s_{vv}^{t}(i,l)}{s_{vv}^{m}(i,l)}\right|^2 + \left|\frac{s_{hh}^{m}(i,l)e^{j\left[\phi_{hh}^{m}(i,l)-\phi_{vv}^{m}(i,l)\right]} - s_{hh}^{t}(i,l)e^{j\left[\phi_{hh}^{t}(i,l)-\phi_{vv}^{t}(i,l)\right]}}{s_{hh}^{m}(i,l)e^{j\left[\phi_{hh}^{m}(i,l)-\phi_{vv}^{m}(i,l)\right]}}\right|^2\right] \tag{6.1}$$

where the superscripts m and t refer to the measured and theoretical responses, respectively, N refers to the total number of bistatic angles measured, and M refers to the total number of frequency points measured. Quantities s and ϕ refer to the magnitude and phase of the co-polarized mean bistatic scattering amplitudes respectively. The CBSM technique offers a number of advantages over the FSTM technique in that measurements need only be performed on a small volume of the random medium and that more than one measured parameter is used to characterize K. Basically, the scattering properties of a cluster of the random medium can be accurately characterized in an anechoic chamber environment. Basically it is rather convenient to position and orient a relatively small target (the cluster of the random medium) and therefore it becomes possible to measure many independent samples of the random media independent of their volume fractions. Moreover, since in characterization of the effective propagation constant, bistatic measurements at many bistatic angles are used the effect of systematic errors on the overall measurement accuracy is minimized.

It should be noted here that phase-coherent polarimetric bistatic scattering measurement is a difficult task, since in moving the receiving antenna the phase coherence and the polarization reference coordinate may be perturbed. To avoid these problems, the co-polarized bistatic scattering amplitudes of the cluster of constituent particles are measured using the bistatic measurement technique described in Chapter V.

In principle, a cluster of particles confined in any geometry of arbitrary boundary can be used so long as the bistatic scattering response of an equivalent homogeneous dielectric material having the same boundary can be evaluated. The effective dielectric constant ($\epsilon_{eff} = \epsilon' + j\epsilon''$) or the effective index of refraction ($n_{eff} = n' + jn''$) can be equivalently used for a random media with the effective propagation constant $K = K' + jK''$ where the equivalent relation is given by: $K = k_o n_{eff}$, $K = k_o\sqrt{\epsilon_{eff}}$.

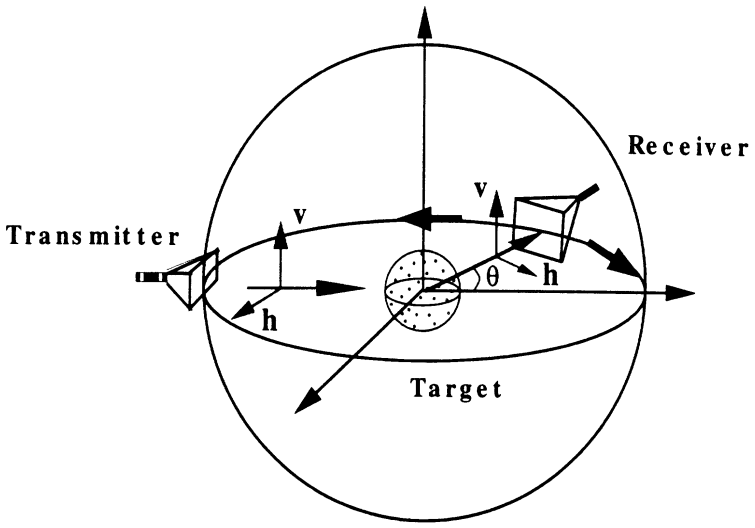

(a)

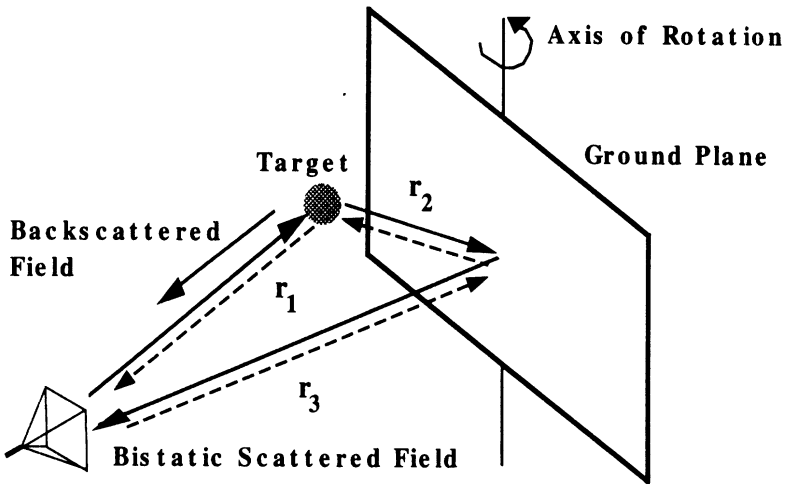

(b)

Figure 6.2: The proposed measurement setup,(a) a bistatic radar measuring a cluster of a random medium, and (b) a monostatic radar in conjunction with a rotatable ground plane measuring the bistatic response of a cluster of a random medium.

The measured mean bistatic scattering response of the cluster is a function of the equivalent dielectric constant of the dense random medium and the shape and size of the enclosing volume. In this thesis, a spherical boundary is used since an exact solution (Mie solution) for the bistatic scattered fields of a homogeneous dielectric sphere of arbitrary size can easily be computed [60]-[3]. In addition, the symmetry in the spherical geometry eliminates errors due to target misalignment, and allows for collecting independent samples simply by rotating the spherical enclosure.

In summary, the measurement procedure involves three steps starting with positioning a cluster of constituent particles of a random medium confined in a spherical volume in front of the ground plane at an appropriate distance. Then, the ground plane is rotated to the desired bistatic angle and the bistatic component of the backscattered signal is gated and measured. Then, the coherent and incoherent components of the scattered fields are separated using many independent measurements of the cluster for given incident and bistatic directions. These independent radar measurements are obtained by rotating the cluster of particles around its axis of symmetry and/or randomizing the particles within the spherical enclosure.

6.2.1 Remarks on the Size of Spherical Enclosure

As it was mentioned before, measuring the scattering properties of the random medium can be conducted much easier when a sample of the random medium is confined into a relatively small spherical geometry. However, for accurate measurements of K, the size of the enclosing sphere must be chosen so that the confined cluster of parti s preserves the scattering statistics of the infinite random medium. There are a number of conflicting criteria that need be considered in choosing the size of the enclosure. For example, the cluster must include many particles of the random medium

so that the effect of multiple scattering between particles is preserved. Furthermore, the cluster must be larger than many field correlation distances in the random medium so that the statistics of the scattered field is preserved. Based on numerical simulations of bistatic scattering from 2-D random media, Sarabandi and Siqueira [48] found that a cluster size as small as one wavelength is enough to obtain the correct estimate of the effective propagation constant when particle sizes are on the order of $\lambda/10$. On the other hand, a cluster of many wavelengths in size would have a mean bistatic response that would vary rapidly as a function of the bistatic scattering angle (multiple nulls in the pattern). Hence, the measured bistatic response from a large cluster is prone to errors in the rotation angle of the ground plane. Furthermore, Sarabandi and Siqueira [48], found that in the backscattering direction, the standard deviation of the magnitude of the scattered field increased with increasing the size of the cluster. In this case, a large number of independent measurements of the cluster is needed for accurate estimation of the mean backscatter field.

6.2.2 Sensitivity Analysis

Scattering from a homogeneous dielectric sphere is a function of two parameters, namely, the index of refraction ($n = n' + jn''$) and the normalized radius r/λ_o, where r is the radius of the sphere and λ_o is the wavelength in free space. In what follows, the sensitivity of the bistatic scattered field of a homogeneous sphere to these two parameters is studied. This sensitivity analysis reveals the accuracy with which the effective index of refraction of random media can be measured.

As mentioned, one of the influential parameters in the bistatic response of a dielectric sphere is the radius normalized to wavelength. As an example, Fig. 6.3a shows the bistatic responses of two spheres with $r/\lambda_o = 1$ and $r/\lambda_o = 2$, and an

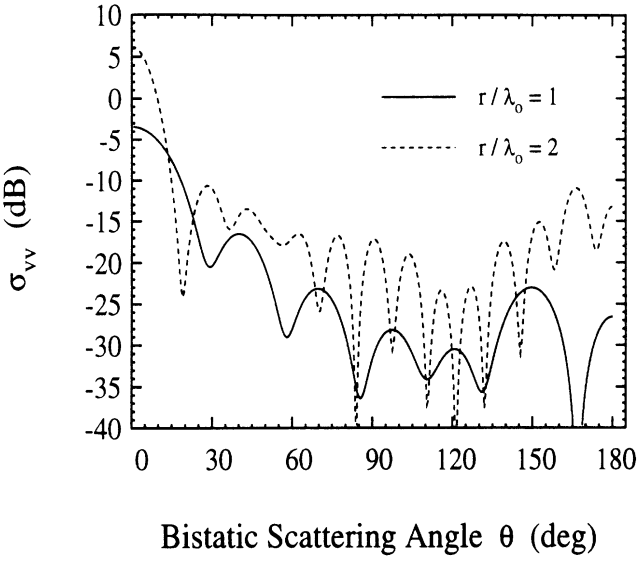

(a)

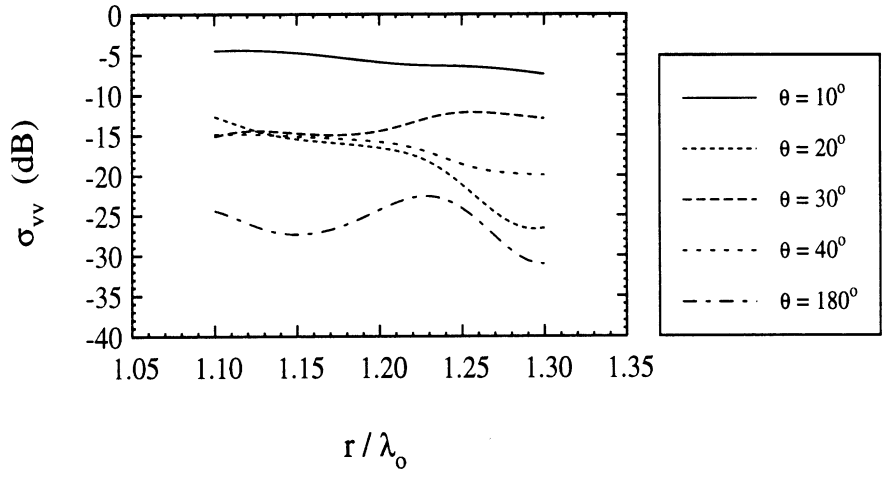

(b)

Figure 6.3: Computed bistatic scattering response of (a) two spheres with $r/\lambda_o = 1$ and $r/\lambda_o = 2$ as function of bistatic scattering angle, and (b) a dielectric sphere as function of r/λ_o. $n = 1.4 + j0.0$ was used in these computations.

index of refraction of $n = 1.4 + j0.0$ (a typical value for dry snow). It is shown that the overall scattering amplitudes and the number of nulls in the scattering pattern increase with increasing r/λ_o. This sensitivity to normalized radius suggests that if the bistatic scattering measurements were to be conducted for spheres with different radii, a much larger set of independent data would be available for the inversion of the index of refraction. Instead of varying the radius, the wavelength can be varied as long as the index of refraction remains constant. This is usually the case when a small bandwidth around the center frequency is used ($\Delta f/f_o < 10\%$). Figure 6.3b shows the sensitivity of the bistatic radar cross section of homogeneous spheres with $n = 1.4 + j0.0$ as a function of r/λ_o over a 15% bandwidth. This can be particularly useful in cases where the size of the spherical enclosure is on the order of many wavelengths and the bistatic response can be measured accurately at a limited number of bistatic angles close to forward scattering direction. In this investigation the frequency response of the bistatic scattering cross section of clusters of random media are measured and used in the inversion algorithm.

For most practical cases of interest, the imaginary part of K, which is proportional to the extinction in the random media, is much smaller than the real part. Hence, it is important to determine whether the measurement technique is accurate enough to detect small variations in the imaginary part of the effective index of refraction of the medium. In order to examine the sensitivity of the bistatic scattering radar cross section of a homogeneous sphere ($\sigma_{ii}(n', n'', \theta)$) to variations in the imaginary part of the index of refraction, let us define the normalized differential bistatic radar cross section by

$$\gamma_{ii}(\theta) = \frac{1}{\sigma_{ii}(n', n'', \theta)} \frac{\partial \sigma_{ii}(n', n'', \theta)}{\partial n''} \quad ; \qquad i = v \ \ or \ \ h \tag{6.2}$$

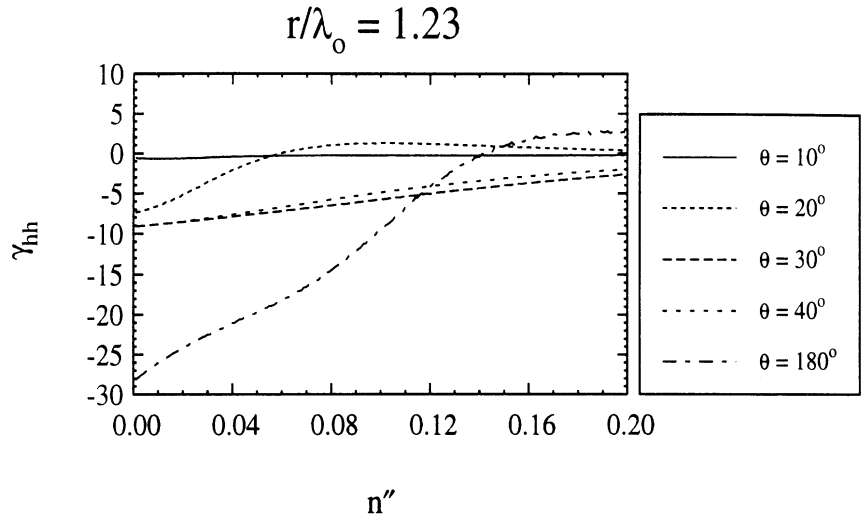

(a)

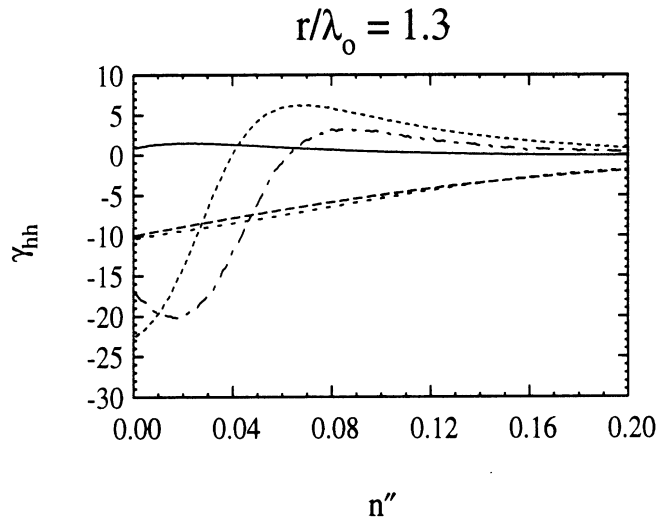

(b)

Figure 6.4: Computed normalized differential bistatic radar cross section defined by (6.2) as a function of n'' for dielectric spheres with $n' = 1.4$ (a) $r/\lambda_o = 1.23$, and (b) $r/\lambda_o = 1.3$.

The normalized differential bistatic radar cross section of two dielectric spheres with $n' = 1.4$ and $r/\lambda_o = 1.23$ and $r/\lambda_o = 1.3$ are shown in Fig. 6.4a and 6.4b as a function of n'' respectively. Figures 6.4a and 6.4b indicate that the bistatic scattering cross sections are sensitive to slight changes in n'' especially when n'' is small. It is also shown that the sensitivity to n'' depends on the normalized radius and the bistatic scattering angle. Therefore, a combination of bistatic scattering response in both frequency and scattering angle should drastically enhance the accuracy in measurement of n''.

6.3 Verification of the New Technique

In this section, the validity and accuracy of the proposed method in measuring the effective propagation constant of random media is examined by conducting numerical simulations and experiments in an anechoic chamber. For all measurements reported in this chapter, the same experimental setup described in section 5.4 was used.

To examine the accuracy in the measurement of the effective propagation constant of random media using the proposed method, a random medium with low fractional volume is considered. It is well known that the effective field approximation (EFA) method can accurately predict the effective propagation constant of random media in the limiting case of low volume fractions [27]. Since at low particle densities, the effect of multiple scattering between particles on the overall scattered field is negligible, a simple Monte Carlo simulation based on single scattering properties of the particles confined within the finite volume can be performed to demonstrate the feasibility of extracting the effective index of refraction from the mean bistatic pattern of the cluster of particles. In this thesis, a random medium with fractional volume

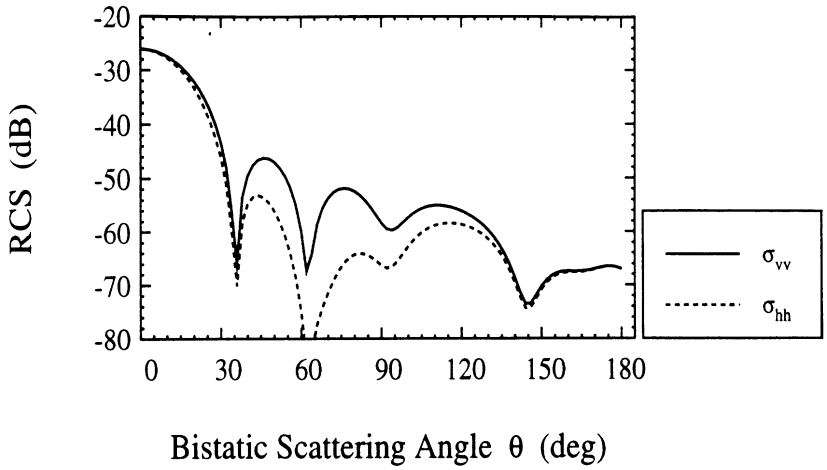

Figure 6.5: Mean bistatic scattering cross sections of the spherical cluster of the test medium (1% volume fraction) derived from the numerical simulation.

1% comprised of metallic spheres with diameter 6.35 mm was chosen as a test case. The metallic spheres (scatterers) were confined within a 7.62 cm spherical boundary ($\sim 2\lambda$ at 9.5 GHz). In such spherical enclosure, on average, only sixteen spheres can be enclosed for achieving 1% fractional volume. The positions of the scatterers inside the spherical enclosure were determined using a random number generator with a uniform distribution. The effective propagation constant of the test medium under the effective field approximation can be computed from [27]:

$$K_{EFA} = \left[k^2 + 4\pi\ n_o\ S_{vv}(\theta_i, \phi_i; \theta_i, \phi_i)\right]^{1/2} \tag{6.3}$$

where k is the wavenumber in the background medium, n_o is the number density of particles in the medium, and $S_{vv}(\theta_i, \phi_i; \theta_i, \phi_i)$ is the $\hat{v}\hat{v}$ polarized scattering amplitude of a sphere in the forward scattering direction. The effective propagation constant of the test medium under the effective field approximation is reported in Table 6.3.

First let us compare the results based on the Monte Carlo simulation with the EFA

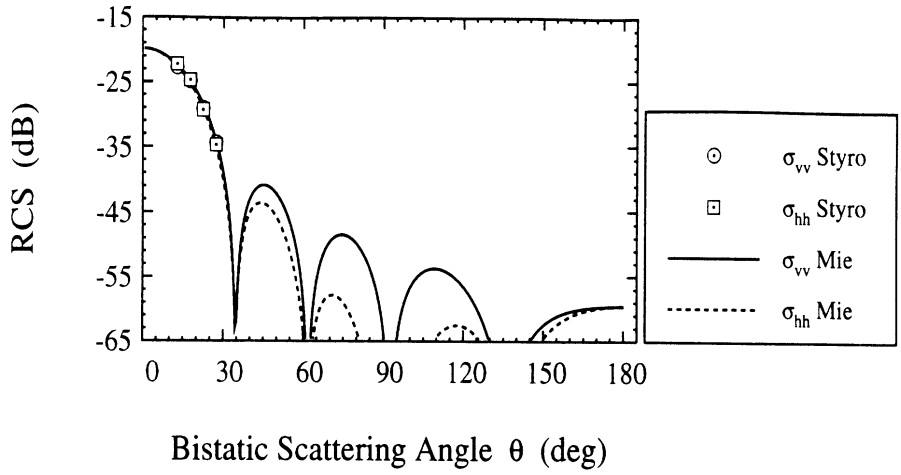

Figure 6.6: Comparison between the measured mean bistatic scattering radar cross section of a styrofoam sphere (7.62 cm in diameter) and the calculated bistatic scattering radar cross section of a homogeneous sphere with $\epsilon_{styro} = 1.0397 + j0.0198$.

results. The bistatic scattered field from a spherical cluster of the test medium was computed from coherent addition of scattering from individual particles within the cluster. Overall, the bistatic scattered fields from 1000 independent realizations of the spherical cluster of the test medium were computed in order to evaluate the desired statistics of the bistatic response. Figure 6.5 shows the mean bistatic scattering radar cross section of the spherical cluster derived from the coherent component of the bistatic scattered fields. Existence of deep nulls in the bistatic pattern whose locations are a function of the size of the spherical enclosure indicate the existence of an equivalent index of refraction for the medium. Using equation (6.1), the effective propagation constant of the test medium is calculated from the numerically generated bistatic response and is reported in Table 6.3. It is shown that the result based on the Monte Carlo simulation is in a very good agreement with EFA.

With the confidence on the feasibility of the procedure we proceeded with the experimental verification. For this purpose, ten different spherical clusters of the test medium were constructed where styrofoam spheres with diameter 7.62 cm were used

as hosts for the metallic spheres. The positions of the metallic spheres inside the styrofoam spheres were determined using the random number generator described before. In backscatter, the response from a styrofoam sphere is expected to be undetectable at X-band and that is the reason for using styrofoam pedestals as target supports. However, around the forward scattering direction, the bistatic response of styrofoam objects is significant and perhaps comparable to that of a sparse random medium. In fact the effective propagation constant of the test medium as predicted by EFA is smaller than that of a typical styrofoam. Thus, the effect of styrofoam scattering must be removed from the measured bistatic response of the spheres embedded in the styrofoam sphere. The mean bistatic scattering response from a pure styrofoam sphere identical to those used as hosts for the metallic spheres was measured using the proposed CBSM technique and is shown in Fig. 6.6. The measured effective propagation constant of styrofoam was found to be $K_{styro} = (1.0197 + j\ 0.0097)\ k_o$ which corresponds to $\epsilon_{styro} = 1.0397 + j\ 0.0198$. Then, bistatic measurements were conducted on each of the ten spherical clusters (styrofoam + metallic spheres). Additional independent measurements were obtained by rotating each spherical cluster 10 times. Overall, 100 independent measurements were collected at each bistatic angle. The measured average incoherent power of the bistatic scattered field is shown in Fig. 6.7 and compared with those obtained from the numerical simulation. Then, the bistatic scattered fields of the styrofoam sphere were subtracted coherently from the mean bistatic scattered fields of the sphere embedded styrofoam sphere (styrofoam + metallic spheres). The remainder represents the mean bistatic scattered fields of the test medium (metallic spheres). These quantities were then used in equation (6.1) to evaluate the effective propagation constant K_{measr} of the test medium. The measured effective propagation constant of the test medium is reported in Ta-

K_{EFA}/k_o	$1.0098 + j0.0033$
K_{num}/k_o	$1.0099 + j0.0028$
K_{measr}/k_o	$1.0099 + j0.003$

Table 6.1: Summary of the effective propagation constant of the random medium of 1% volume fraction derived from measurements, numerical simulations, and the EFA approximation.

ble 6.3 and shows a very good agreement with the effective propagation constant estimated by EFA. The bistatic scattered responses of the styrofoam sphere and the sphere-embedded styrofoam sphere and the subtracted bistatic response along with the best Mie solution fit are shown in Fig. 6.8 as function of the bistatic scattering angle.

6.4 Conclusions

A new technique for measuring the effective propagation constant of dense random media is presented. The proposed method is not restricted by the physical properties of the random medium such as particle size, shape and density. In this technique, the mean bistatic scattered fields of a cluster of random medium, confined in a known geometrical boundary, are measured using a monostatic radar and a rotatable ground plane. Then the measured mean bistatic scattered fields are fitted to the bistatic scattered fields of a homogeneous lossy material with the same geometrical boundary. The accuracy of the new technique in measuring the effective propagation constant of a dense random medium was verified both experimentally and numerically in the low volume fraction limiting case. The sensitivity analyses of the proposed measurement technique show a strong dependence of the measured quantities on slight variations in

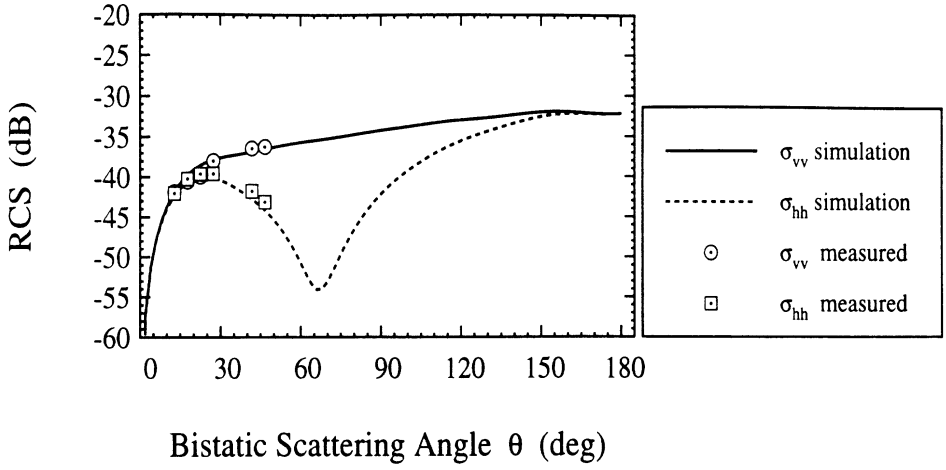

Figure 6.7: Comparison between the measured and simulated average incoherent bistatic radar cross section of the test medium.

the imaginary part of K. It is also shown that using this technique, the permittivity of low dielectric materials such as styrofoam can be measured very accurately.

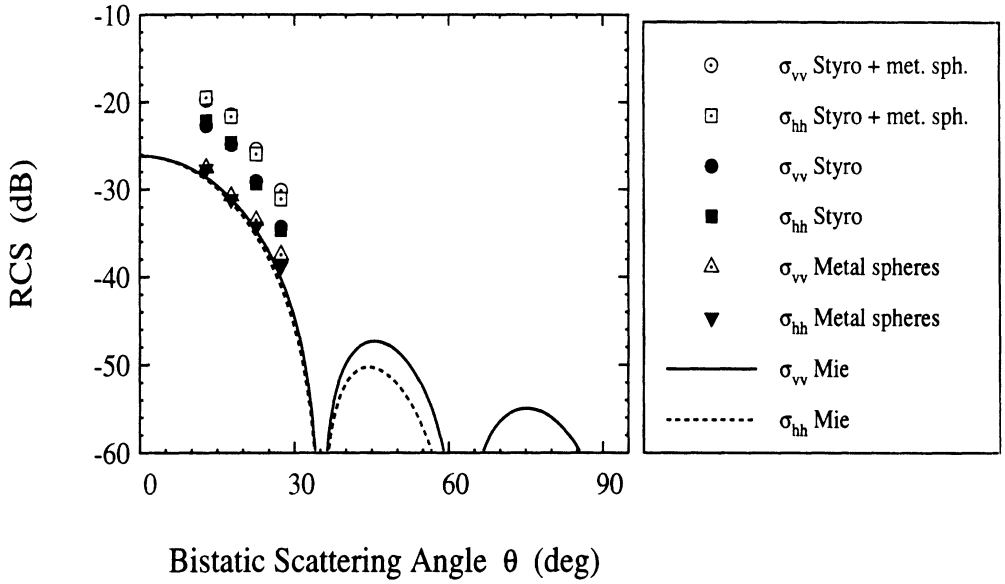

Figure 6.8: Comparison between the measured bistatic responses of the styrofoam sphere, the sphere embedded styrofoam sphere, and the coherently subtracted bistatic scattering response (metallic spheres) along with the best Mie solution fit.

CHAPTER VII

EXPERIMENTAL STUDY OF THE EFFECTIVE PROPAGATION CONSTANT OF DENSE RANDOM MEDIA

In the previous chapter, a new technique (CBSM) for the measurement of the effective propagation constant (K) of dense random media was developed. In addition, the validity of the new technique was demonstrated by performing experiments for random media for which the effective propagation constant is known. The CBSM technique is an accurate technique for measuring K of dense random media over a wide range of volume fractions.

The only reported experimental investigation aimed at determining the region of validity of exiting analytical models, such as EFA and QCA, was conducted by Mandt *et al.* [27]. In this investigation, the FSTM method was used to measure K of dense random media ($f \leq 0.1$) and the measured extinction coefficient was compared with those predicted by EFA and QCA. At these volume fractions, the analytical models were in good agreement with the measured extinctions. This is also confirmed by the results which will be reported in this chapter. However, due to the limitations inherent in the FSTM technique, it was difficult to measure the effective propagation

constant of dense media with higher volume fractions.

In this chapter, an experimental study of the effective propagation constant of dense random media aimed at establishing the region of validity of existing theoretical models is performed using the CBSM technique. In the following section, a brief introduction of the theoretical models to be used in this investigation is carried out. In Section 7.2, measurements of dense random media of different volume fractions are presented and compared with existing analytical models.

7.1 Theoretical Models For Computing K

There are a number of analytical models for the calculation of effective propagation constant in random media. Among these, the most widely used models are: the Polder-Van Santen mixing formula, the effective field approximation (EFA), the quasicrystalline approximation (QCA), and the quasicrystalline approximation with coherent potential (QCA-CP) .

7.1.1 Polder-Van Santen Mixing Formula

The Polder-Van Santen mixing formula is a low frequency approximation [62] where the effect of scattering in the calculation of propagation loss is ignored. In the case of a two-phase mixture consisting of spherical inclusions (ϵ_i) imbedded in a host medium (ϵ_h), the following expression can be used to compute the effective dielectric constant (ϵ_{eff}) of a random medium

$$\epsilon_{eff} = \epsilon_h + 3\, f\, \epsilon_{eff} \frac{(\epsilon_i - \epsilon_h)}{(\epsilon_i + \epsilon_h)} \tag{7.1}$$

where f is the fractional volume of the inclusions.

7.1.2 Effective Field Approximation

In the effective field approximation, the scattering particles of a random medium are assumed to be independent in position. This assumption is validy for random media with sparse concentration of scatterers ($f < 0.01$) that are uniformly distributed in space. In this case, single scattering is the primary scattering mechanism influencing wave propagation in random media.

For a sparse concentration of spherical scatterers, the effective propagation constant under the effective field approximation can be computed using the following equation [6], [27].

$$K_{EFA} = \left[k^2 + 4\pi n_o S_{vv}(\theta_i, \phi_i; \theta_i, \phi_i)\right]^{1/2} \tag{7.2}$$

where k is the wavenumber in the background medium, n_o is the number density of particles in the medium, and $S_{vv}(\theta_i, \phi_i; \theta_i, \phi_i)$ is the $\hat{v}\hat{v}$ polarized scattering amplitude from a sphere in the forward scattering direction.

7.1.3 Quasicrystalline Approximation (QCA)

In a dense random medium, the particles are no longer independent in position. In this case, multiple scattering between particles is significant. At the expense of much mathematical complexity, the QCA can be used for the estimation of the effective propagation constant of nontenuous random media by including the effect of multiple scattering between particles [52]. However, it should be noted that in the implementation of QCA only the correlation between two particles is permitted. Hence, positions of the first and third particles in, for example, the triple multiple scattering process

are assumed to be independent. The pair distribution function of the constituent particles is a statistical property of the random medium which characterizes the correlation between positions of any two particles. Accurate characterization of the pair distribution function for a random medium can be as difficult as the characterization of the effective propagation constant itself. The Percus-Yevick pair distribution function [52], originally developed for fluids is commonly used in application of QCA for most dense random media. A recent numerical investigation [50] has demonstrated that the pair distribution function of particles packed under the influence of gravitational forces could be substantially different from the Percus-Yevick pair distribution function, thereby adding an additional dimension of complexity in determining ϵ_{eff} *via* QCA.

For small scatterers ($ka << 1$), a closed form expression for K of a dense random medium consisting of a collection of spherical particles of fixed size has been derived using QCA and Percus-Yevick pair distribution function [52].

$$K_{QCA}^2 = k^2 + \frac{3 f k^2 y}{1 - fy} \left[1 - i \frac{2}{3} \frac{(ka)^3 y}{1 - fy} \frac{(1-f)^4}{(1+2f)^2} \right] \tag{7.3}$$

and

$$y = \frac{\epsilon_s - \epsilon}{\epsilon_s + 2\epsilon}$$

Here, ϵ_s and ϵ are the permittivities of the scatterers and the background medium respectively, and, a, is the radius of the spherical particles.

7.1.4 Quasicrystalline Approximation with Coherent Potential (QCA-CP)

Under QCA, scattering from a particle is assumed to be dependent on the dielectric contrast between the particle and the background medium. As the concentration of particles in the medium increase, the medium surrounding a particle is a mixture of the background medium and other particles. A modified version of QCA which takes this into account is the quasicrystalline approximation with coherent potential (QCA-CP). In this approximation, the scattering from a particle depends on the dielectric contrast between the particle and the effective dielectric constant of the random medium which is not known a priori.

For small scatterers ($ka << 1$), a closed form expression for K_{QCA-CP} of a dense random medium consisting of a collection of spherical particles of a given particle size distribution has been derived in [11] and [56]. The effective propagation constant K under QCA-CP, with the Percus-Yevick as the pair distribution function, can be cast into the following form

$$\begin{aligned} K^2_{QCA-CP} = \; & k^2 \; + \frac{3K^2_{zr}}{D(K_{zr})} \sum_{l=1}^{L} f_l y_l(K_{zr}) \\ & \times \; \{1 + i\frac{2K^3_{zr}}{3D(K_{zr})}[a_l^3 y_l(K_{zr}) + \sum_{j=1}^{L} y_j(K_{zr}) \\ & \times \; a_j^3 n_j 8\pi^3 H_{jl}(\omega = 0)]\} \end{aligned} \tag{7.4}$$

where K_{zr} represents the zeroth order solution which satisfies the following non-linear equation

$$K^2_{zr} = k^2 + \frac{3K^2_{zr}}{D(K_{zr})} \sum_{l=1}^{L} f_l y_l(K_{zr}) \tag{7.5}$$

and

$$
\begin{aligned}
D(K_{zr}) &= 1 - \sum_{j=1}^{L} f_j y_j(K_{zr}) \\
y_j(K_{zr}) &= \frac{k_j^2 - k^2}{3K_{zr}^2 + (k_j^2 - k^2)}
\end{aligned}
\tag{7.6}
$$

Here, k_j, f_j, a_j, and n_j are the wavenumber, fractional volume, radius, and number density of the jth particle size respectively. $H_{jl}(\omega = 0)$ is related to the Fourier transform of the pair distribution function of two particles of species j and l separated by a distance $\mathbf{r}$. The details of computing $H_{jl}(\omega = 0)$ for the Percus-Yevick pair distribution functions can be found in [11].

7.2 Experimental Results and Comparison with Analytical Models

In this section, the effects of various electrical and physical properties of dense random media on its effective propagation constant are investigated experimentally. In general, the effective propagation constant of a random medium is influenced by the size, shape, orientation distribution, volume fraction, particle arrangement, and permittivity of the constituent particles. The measurements reported here were conducted with the following objectives in mind: (a) examination of the dependence of K on the physical and electrical parameters, (b) characterization of the scattering mechanisms in random media as a function of volume fraction of particles, and (c) generation of a data base to be used as a benchmark for further comparisons with existing theoretical models.

These measurments were conducted using the same experimental setup used in

Chapter VI to validate the CBSM technique.

7.2.1 Random Media with Spherical Particles of Fixed Size

In this section, random media with spherical particles of fixed size and dielectric constant are considered. As a result, only the effects of the volume fraction, particle arrangement, and the dielectric constant of the constituent particles on the effective propagation constant are studied. Teflon spheres of diameter 6.35 mm ($a/\lambda_o = 0.1$ at 9.5 GHz) and Soda-Lime glass spheres of diameter 6.0 mm ($a/\lambda_o = 0.095$ at 9.5 GHz) were used to construct random media over a wide range of volume fractions (10% to 60%). Permittivity of the Teflon and glass particles were characterized experimentally by measuring the bistatic scattering response of solid Teflon and glass spheres. For example, the measured bistatic response of a 16 mm glass sphere and the best fit based on the Mie solution are shown in Fig. 7.1. The dielectric constants of glass and Teflon were found to be $\epsilon_{glass} = 6.93 + j\ 0.10$ and $\epsilon_{tef} = 2.10 + j\ 0.001$ respectively. The large contrast between permittivity of the constituent particles are chosen to demonstrate the effect of multiple scattering on the effective propagation constant. In evaluation of K of constructed dense random media, the co-polarized responses (VV and HH) of 100 independent spherical clusters of the medium were measured at six bistatic scattering angles (10°, 20°, 30°, 40°, 50°, and 180°) and 18 frequency points within 0.5 GHz bandwidth centered around 9.5 GHz.

Different methods were used to construct random media with different volume fractions. To construct the 10% volume fraction, a styrofoam sphere was used as a host for the scattering particles. In this case, similar to the case of 1% volume fraction the location of particles were determined using the random number generator described in Chapter VI. For higher volume fractions, a hollow styrofoam shell with spherical inner

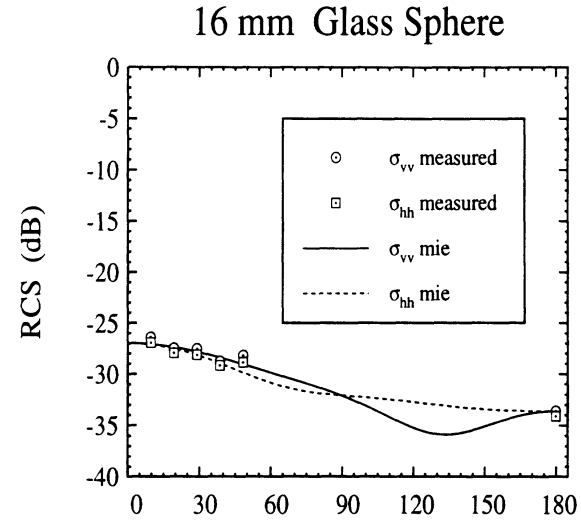

(a)

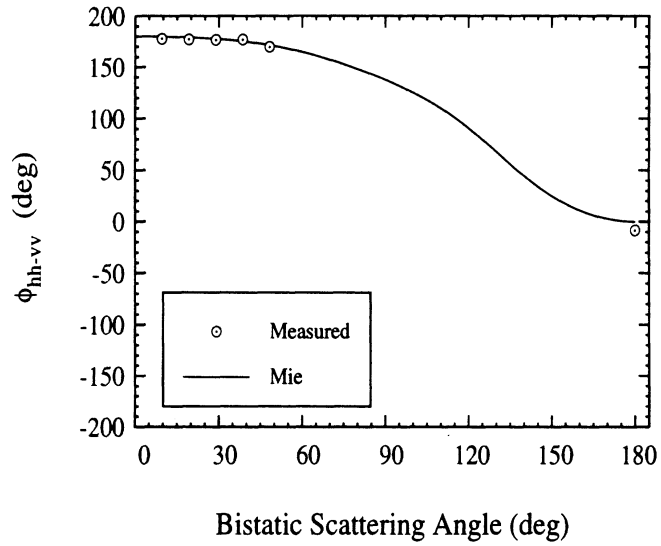

(b)

Figure 7.1: Comparison between the measured and theoretical bistatic response of a glass sphere with diameter 1.6 cm and $\epsilon_{glass} = 6.93 + j0.10$, (a) radar cross sections, and (b) phase-difference.

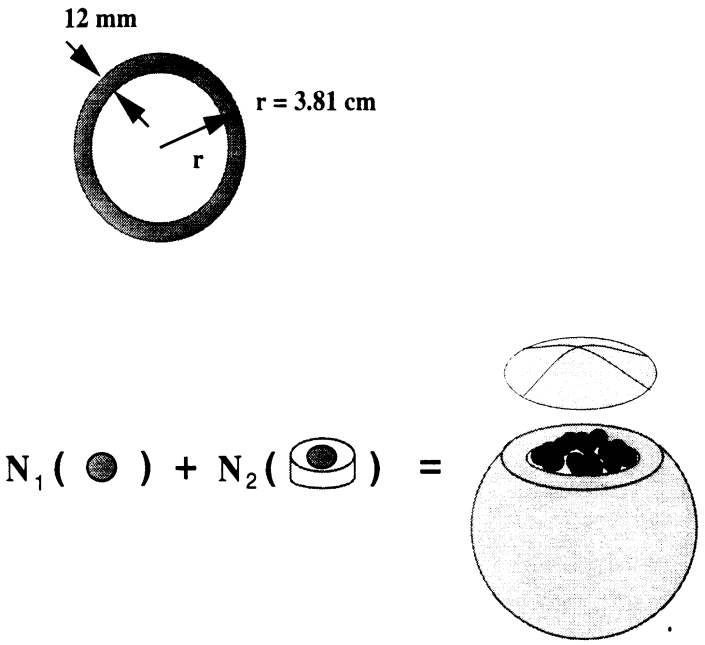

Figure 7.2: The technique used for constructing random media with different volume fractions. Appropriate numbers of free and spaced particles are poured into the hollow styrofoam shell.

and outer surfaces was used to hold the random cluster of the constituent particles. The inner and outer diameters of the styrofoam shell were 7.62 cm ($r/\lambda_o = 1.21$ at 9.5 GHz) and 10.16 cm respectively. In order to achieve the desired volume fraction ($> 10\%$), a mixture of particles embedded into styrofoam disks (spaced particles) and free particles was poured into the styrofoam shell as shown in Fig. 7.2. The styrofoam disks were 1.0 cm in diameter and 0.6 cm in thickness. The average number of free (N_1) and spaced particles (N_2) required to fill the styrofoam shell are listed in Table 7.2.1 for the five different volume fractions used in this experiment. The number of spaced particles was chosen such that the spherical shell would be fully packed with the mixture of free and spaced particles.

Independent realizations of the dense random medium were produced by rotating the cluster of particles in all directions in increments of 20°. In general, the

volume fraction	20%	30%	40%	50%	60%
N_1	170	431	697	962	1240
N_2	240	183	123	64	0

Table 7.1: Average number of free and spaced glass particles required to fill the styrofoam shell (r=3.81 cm) for different volume fractions.

incoherent component of the bistatic scattered field for any realization must be mutually uncorrelated with that of other realizations. To examine whether independent measurements can be realized by simply rotating the cluster, the cross correlation between the incoherent components of the bistatic field as a function of rotation angle (realization number) must be computed. As an example, the normalized correlation function of the bistatic scattered incoherent power of the 40% packed glass particles, measured at $\theta = 20°$, is plotted in Fig. 7.3a. Figure 7.3a clearly shows that rotating the cluster of particles in the prescribed manner produces an independent realization of the random medium. It is well known that the statistics of the magnitude of the scattered field from a statistically homogeneous random medium can be described by the Rayleigh probability density function, provided that the medium includes a sufficient large number of independent scattering centers [44]. Figure 7.3b shows the histogram of the magnitude of the incoherent component of the bistatic scattered field of the 40% packed glass particles. In this figure, a Rayleigh probability distribution function (pdf) with the same mean as the histogram is also shown. The Rayleigh pdf agrees well with the histogram of the measured scattered field which implies that the measured samples of dense media were large enough to include many independent scattering centers. The incoherent bistatic RCS of the cluster is the second moment of the bistatic scattered field which represents the fluctuations around the mean bistatic

scattered field and can be used to determine the uncertainty in the evaluation of the mean-field.

Search routines for the minimization of the nonlinear error function given by (6.1) may arrive at an incorrect value for K, unless certain physical constraints on values of K are imposed. In particular, it is required that $n'_{eff} = K'/k_o \geq 1$ and $n''_{eff} = K''/k_o \geq 0$ which set the lower limits of the search routine. An appropriate selection of the upper limit for n'_{eff} is the index of refraction of the constituent particles. Another important issue is an appropriate choice of the initial guess for the search routine. As will be shown later the Polder-Van Santen mixing formula provides an accurate estimate of the real part of the effective index of refraction of the random medium regardless of the volume fraction. Therefore, the Polder-Van Santen mixing formula is used to provide the initial guess in the search routine. Using the constrained search algorithm, the effective index of refraction of the aforementioned random media were accurately characterized. Figures 7.4a and 7.4b demonstrate the magnitude and phase of the bistatic scattered field of the random medium constructed from glass spheres with 40% volume fraction and a homogeneous sphere with $n_{eff} = 1.6457 + j\ 0.0704$ obtained from the search routine. A similar result is shown in Fig. 7.5 where the bistatic RCS of the random medium constructed from Teflon spheres with 10% volume fraction and the equivalent homogeneous sphere with $n_{eff} = 1.04736 + j\ 0.00155$ as function of frequency for five bistatic angles are shown. These figures demonstrate the accuracy of the search routine in obtaining the effective index of refraction of the random media used in these experiments.

The measured effective index of refraction ($n_{eff} = K/k_o$) for the various dense random media considered here, are summarized in Figs 7.6 and 7.7. In both figures, the measured n_{eff} are compared with theoretical predictions based on EFA, QCA-CP

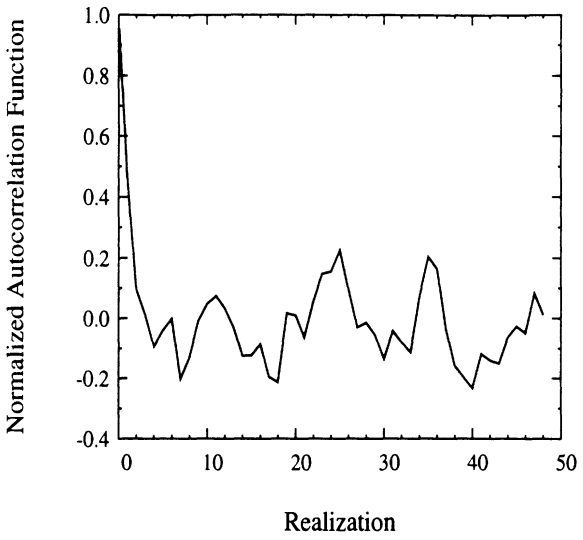

(a)

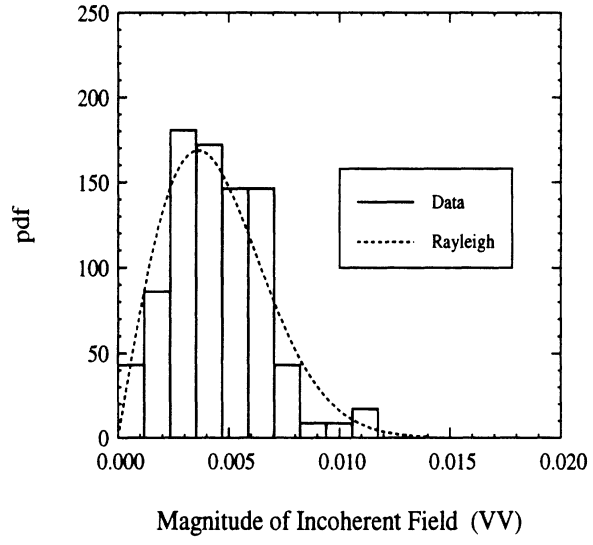

(b)

Figure 7.3: (a) The normalized correlation function of the bistatic scattered incoherent power of the 40% packed glass particles, measured at $\theta = 20^{\circ}$, as a function of the realization number, and (b) Histogram of the magnitude of the measured incoherent bistatic scattered field of the same random media.

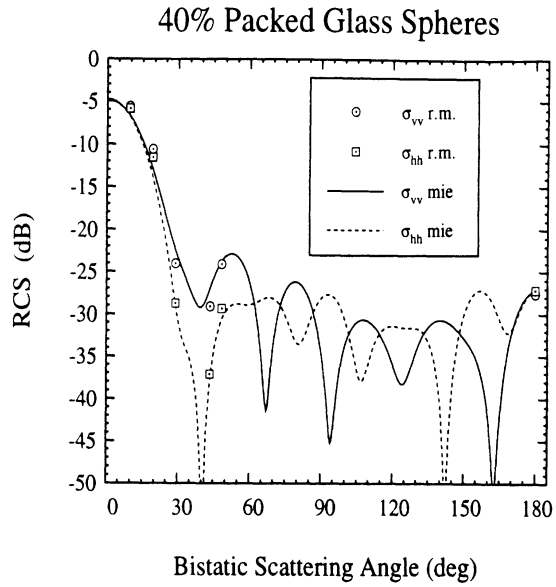

(a)

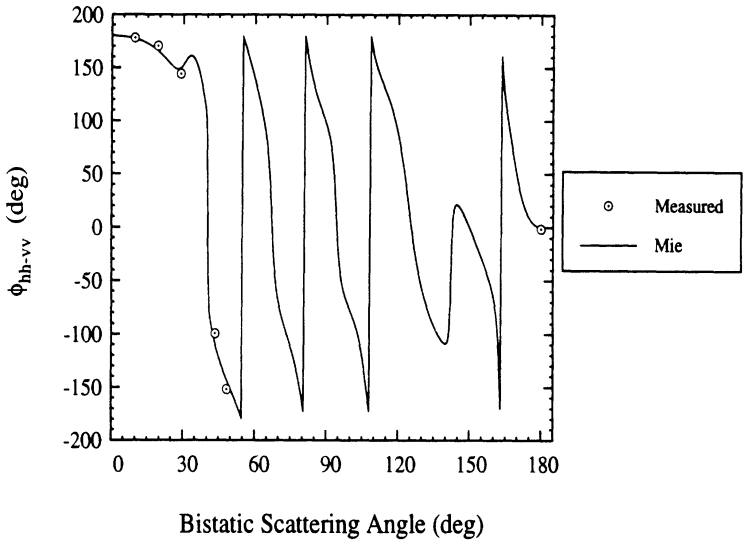

(b)

Figure 7.4: The measured mean bistatic radar cross section and the co-polarized phase difference of 40% packed glass particles are compared with the theoretical responses of a homogeneous sphere computed at 9.5 GHz with $n_{eff} = 1.6457 + j0.0704$ derived from the inversion algorithm.

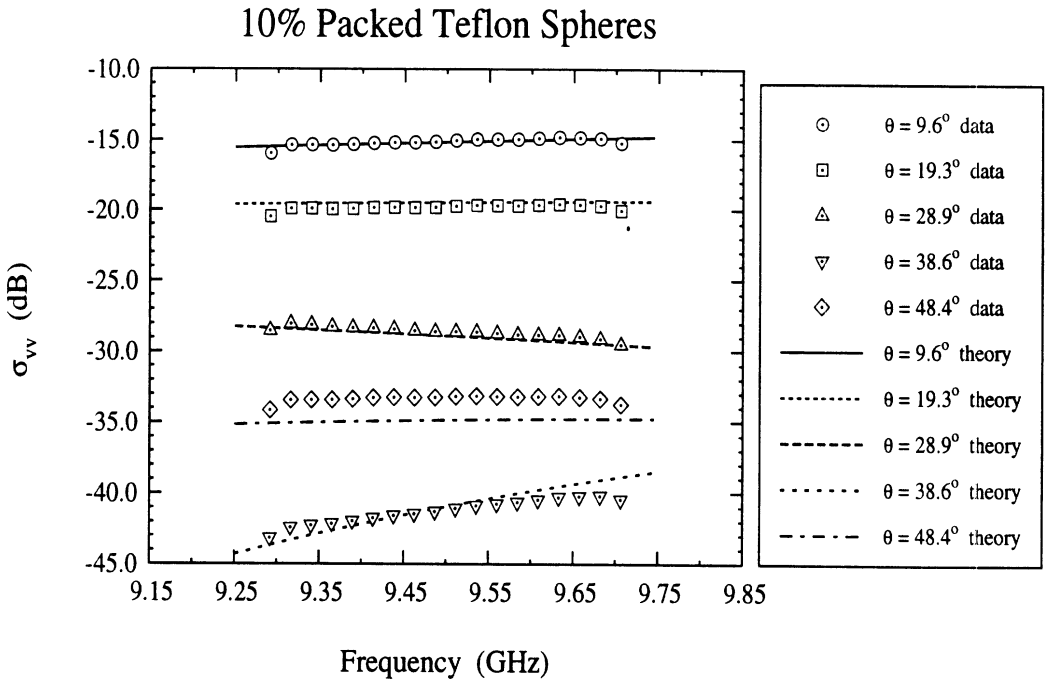

Figure 7.5: The measured mean bistatic radar cross section of 10% packed Teflon particles, as function of frequency, are compared with the theoretical response of a homogeneous sphere with $n_{eff} = 1.04736 + j0.00155$ derived from the inversion algorithm.

under the Percus-Yevick pair distribution function (QCA-CP-PY), and Polder-Van Santen mixing formula as functions of the volume fraction. It is observed that for both dielectric materials, the mixing formula can reasonably estimate the real part of n_{eff}. None of the discussed models, (in particular QCA-CP-PY), were able to predict correctly the imaginary part of n_{eff} for volume fractions above 10%. Comparing Figs. 7.6b and 7.7b, it can be seen that the scattering losses in media constructed from glass spheres is much higher than those of the media constructed from Teflon spheres. This is due to stronger scattered fields generated by the glass spheres with higher permittivity contrast than the Teflon spheres.

As the volume fraction of a random medium increases, it is expected that the internal fields of the scatterers within the random medium become correlated and therefore the incoherent scattered field is reduced. Based on this argument, one may deduce that the scattering loss predicted by the EFA is an upper limit, because EFA assumes uncorrelated scattered fields which would maximize the incoherent scattered power (i.e. maximizes scattering loss). However, as our experimental results indicate (see Figs. 7.6b and 7.7b) this is not the case. At intermediate volume fractions (15%-50%) the scattering loss in both glass and Teflon media is more than what is predicted by the EFA. This phenomenon can be explained by examining the particle arrangement at these intermediate volume fractions. In these cases, the probability of finding two or more phase-correlated particles is rather high. These correlated particles may be viewed as a larger particle whose scattered field is much higher than the sum of the scattered fields from isolated particles which in turn produces higher incoherent scattered power in the random media.

Sand Type	f	$< a >$	$< a > / \lambda_0$
S1	0.65	0.20	0.0064
S2	0.69	0.42	0.0134
S3	0.61	0.59	0.0186

$< a >$ = mean particle radius (mm).

Table 7.2: Summary of physical parameters of each sand type.

7.2.2 Random Media of Sand Particles of Different Sizes

In the previous section, the effective propagation constant of dense random media with spherical particles of fixed size and dielectric constant were measured. In this section, a preliminary investigation of the effects of particle size distribution on the effective propagation constant is conducted. Three types of random media consisting of sand particles of fixed dielectric constant ($\epsilon_{ss} = 3.78 + j0.0004$) each with its own particle size distribution, are measured. The first random medium (S1) consists of ellipsoidal particles (4/3 axial ratio) with sizes described by the particle size distribution shown in Fig. 7.8. On the other hand, the second random medium (S2) consists of spherical particles with sizes described by the particle size distribution shown in Fig. 7.9. The third random medium (S3) consists of angular particles with sizes described by the particle size distribution shown in Fig. 7.10. The experimental procedure described before was used to measure the effective index of refraction of the three random media. The random cluster of sand particles was held in the same hollow styrofoam shell with spherical inner and outer surfaces (see Fig. 7.2).

Full packing of the three random media was achieved at different volume fractions due to differences in particles shapes and size distributions. The magnitudes of the measured bistatic scattered fields of each random medium and the theoretically computed bistatic scattered field of an equivalent homogeneous dielectric sphere with the same effective index of refraction are shown in Fig. 7.8 through 7.10. The measured

effective index of refraction n_{eff} (K/k_o) for the three dense random media along with the theoretically predicted n_{eff} using EFA, QCA-CP under Percus-Yevick pair distribution function, and Polder-Van Santen mixing formula are summarized in Table 7.3. It is observed that for all three ramdom media, the mixing formula and QCA-CP can reasonably estimate the real part of n_{eff}. Again, none of the discussed models and in particular QCA-CP were able to predict correctly the imaginary part of n_{eff}.

	Effective Index of Refraction		
Case	S1 ($f = 0.65$)	S2 ($f = 0.69$)	S3 ($f = 0.61$)
P.V.S. Formula	(1.60, 6.5e-5)	(1.64, 7.0e-5)	(1.56, 6.0e-5)
EFA	(1.39, 3.2e-5)	(1.41, 9.4e-5)	(1.37, 1.9e-4)
QCA-CP-PY	(1.62, 6.8e-5)	(1.65, 7.4e-5)	(1.58, 7.5e-5)
Measured	(1.65, 9.3e-3)	(1.67, 1.2e-3)	(1.59, 9.8e-3)

Table 7.3: Summary of measured and theoretically predicted effective index of refraction of the three random media of sand particles.

7.3 Conclusions

Measurements of the effective propagation constants of different dense random media comprised of homogeneous spherical particles with different packing densities are reported and compared with existing analytical models. It is shown that none of the existing analytical models are able to predict the extinction accurately at volume fractions beyond 10%. It is also shown that Polder-Van Santen mixing formula can be used to predict the real part of K with reasonable accuracy.

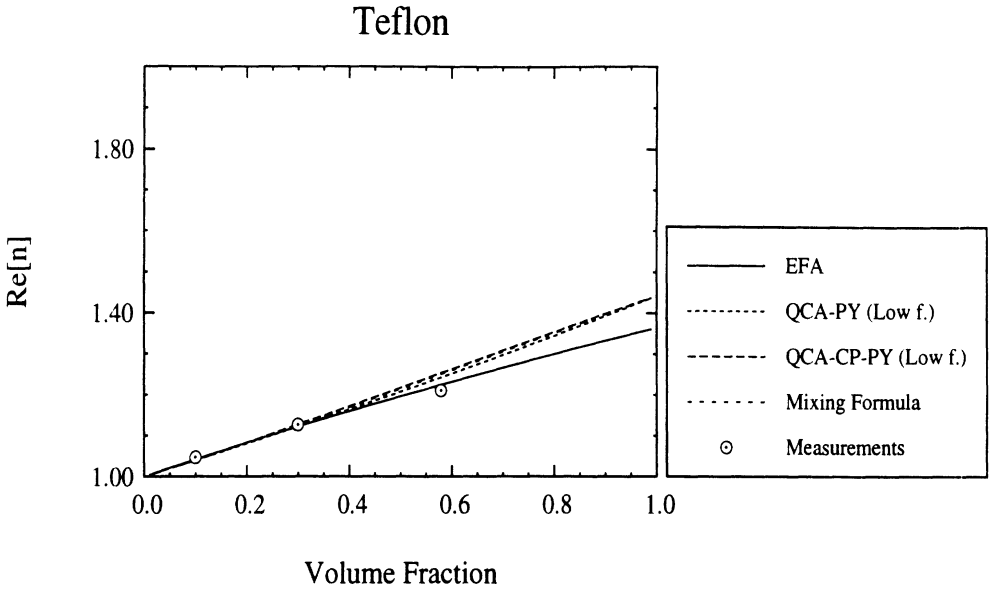

(a)

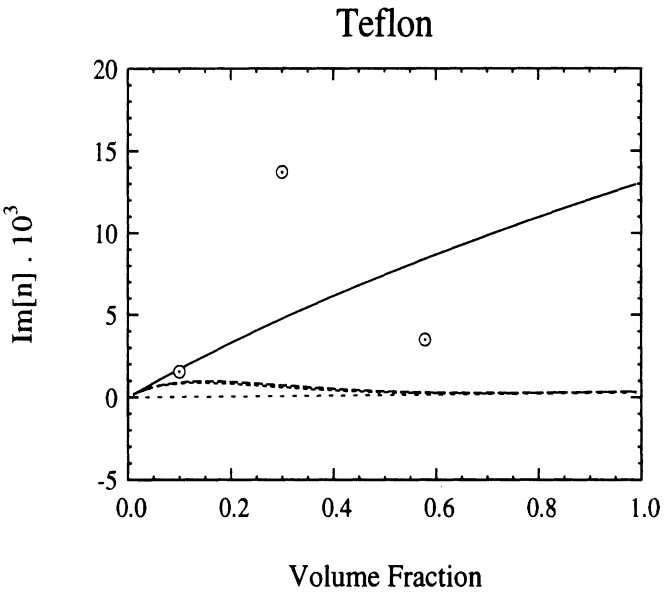

(b)

Figure 7.6: The effective index of refraction (a) real part, and (b) imaginary part of random media constructed from Teflon particles as function of volume fraction. The measured effective index of refraction is compared with those computed using EFA, QCA-PY, and Polder-Van Santen mixing formula.

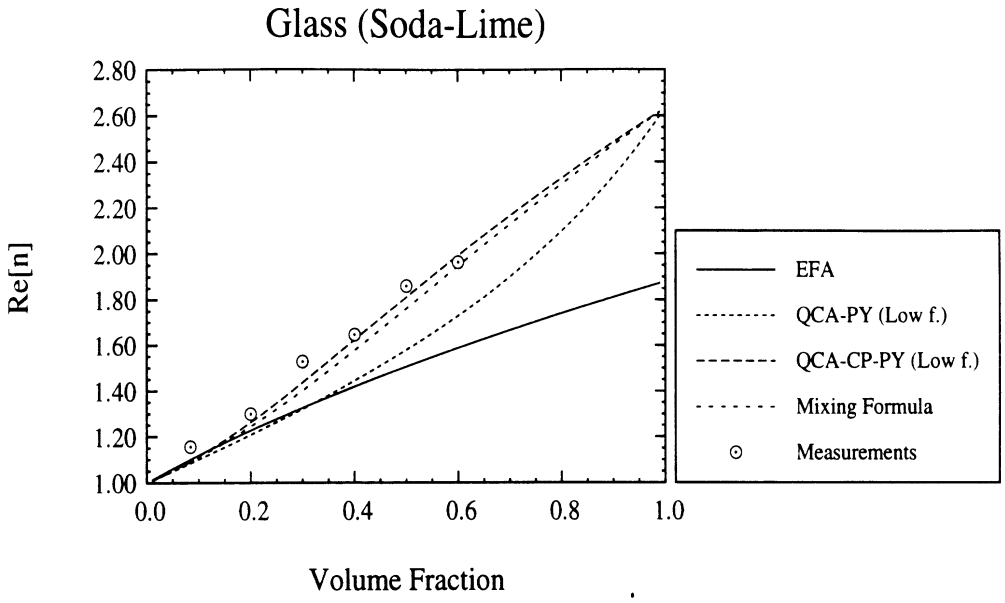

(a)

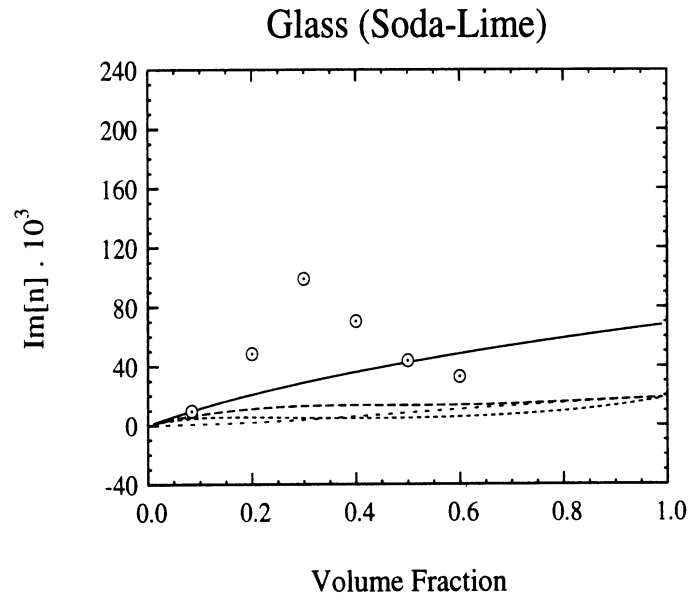

(b)

Figure 7.7: The effective index of refraction (a) real part, and (b) imaginary part of random media constructed from glass particles as function of volume fraction. The measured effective index of refraction is compared with those computed using EFA, QCA-PY, and Polder-Van Santen mixing formula.

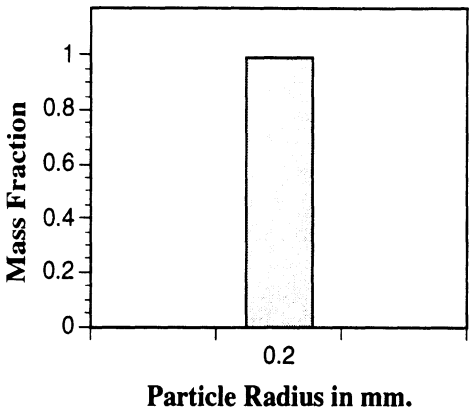

(a)

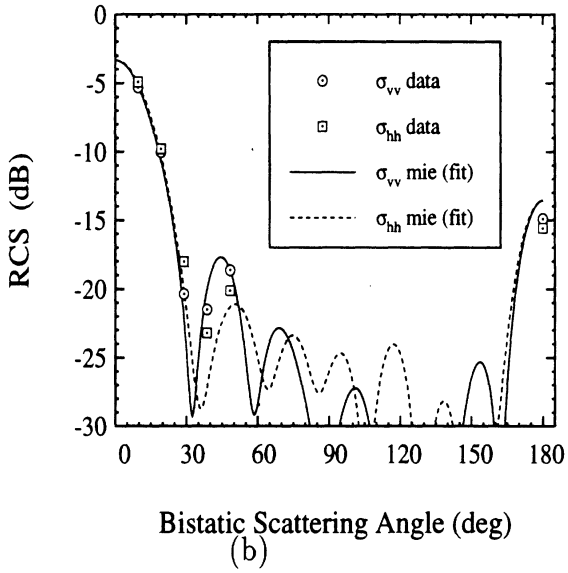

(b)

Figure 7.8: (a) Particle size distribution of the S1 random medium, and (b) comparison between the measured mean bistatic radar cross section of the S1 random medium and the theoretical responses of a homogeneous sphere computed at 9.5 GHz with $n_{eff} = 1.65 + j0.0093$ derived from the inversion algorithm.

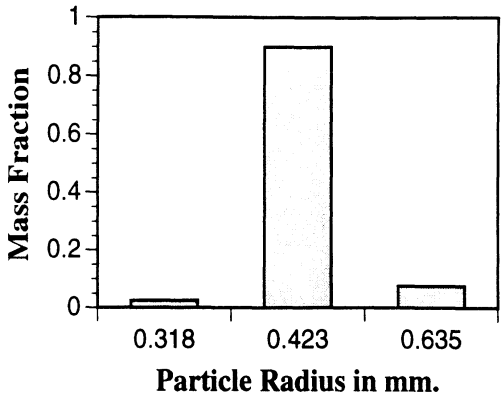

(a)

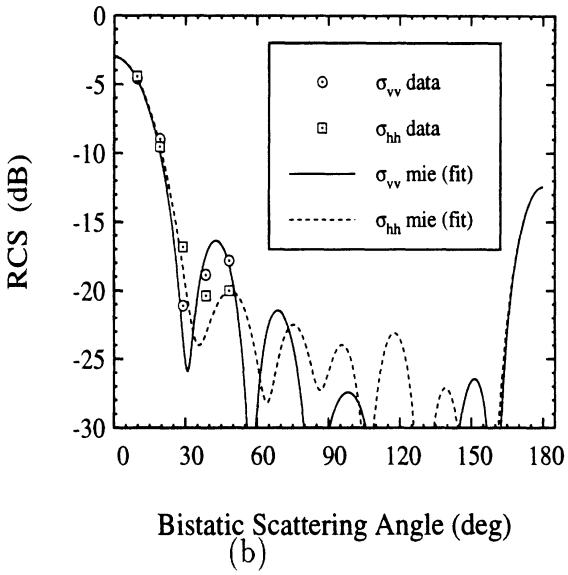

(b)

Figure 7.9: (a) Particle size distribution of the S2 random medium, and (b) comparison between the measured mean bistatic radar cross section of the S2 random medium and the theoretical responses of a homogeneous sphere computed at 9.5 GHz with $n_{eff} = 1.67 + j0.0012$ derived from the inversion algorithm.

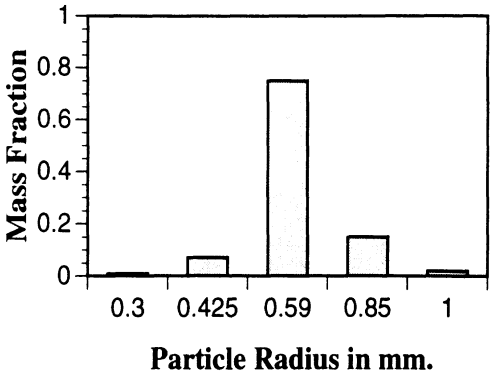

(a)

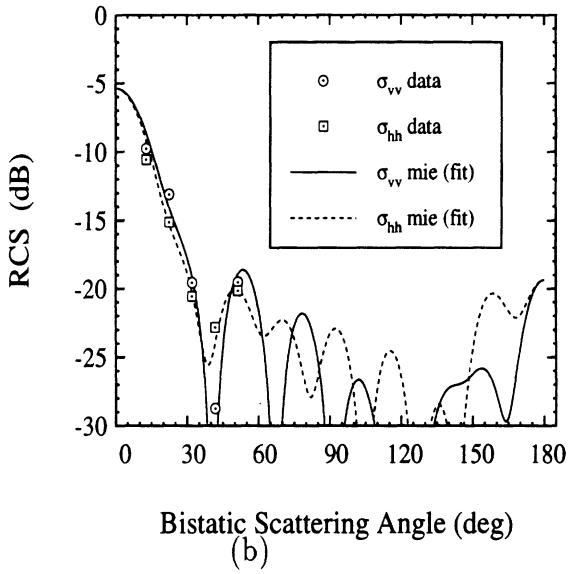

(b)

Figure 7.10: (a) Particle size distribution of the S3 random medium, and (b) comparison between the measured mean bistatic radar cross section of the S3 random medium and the theoretical responses of a homogeneous sphere computed at 9.5 GHz with $n_{eff} = 1.59 + j0.0098$ derived from the inversion algorithm.

CHAPTER VIII

CONCLUSIONS AND RECOMMENDATIONS

8.1 Summary

This thesis comprises six major contributions:

1. Development of a new and accurate calibration technique for coherent-on-receive polarimetric radars.

2. Polarimetric measurements of the backscattering response from bare soil surfaces at millimeter-wave frequencies. These measurements provided evidence of significant volume scattering contribution to the total response from dry soil surfaces.

3. Introduction of a two component hybrid model for predicting the backscatter response from soils at millimeter waves. The first component is a semi-empirical model to predict surface scattering and the second component is a radiative transfer based-model to predict the volume scattering contribution.

4. Development of a novel bistatic measurement technique for measuring the bistatic scattering matrix of point targets using a monostatic polarimetric radar and a ground plane.

5. Development of an accurate technique for measuring the effective propagation constant of random media that is not restricted by the physical properties of the random media.

6. Data base construction of measured effective propagation constants of dense random media of different volume fractions and dielectric properties. The data base can be used to examine the validity region of existing theoretical models.

In Chapter 2, a new technique for calibrating a millimeter-wave coherent-on-receive polarimetric radar system was introduced. A coherent-on-receive polarimetric radar is capable of measuring the Mueller matrix of point or distributed targets directly by transmitting at least four independent polarizations and measuring the vertical and horizontal components of the backscatter signal simultaneously. The calibration technique requires the use of two calibration targets, a metallic sphere and any depolarizing target (for which knowledge of its scattering matrix is not required) to determine the system distortion parameters. In comparison, other technique requires the use of a sphere and a wire grid (limited by polarization purity of the wide grid). The validity of the new calibration technique was examined by measuring the scattering matrices of spheres and cylinders as test targets using a coherent-on-receive radar operating at 34.5 GHz. Excellent agreement between the theoretical and the measured scattering matrices for the test targets were obtained.

In Chapter 3, the millimeter-wave backscatter response of bare-soil was examined by conducting experimental measurements at 35 and 94 GHz using a truck-mounted polarimetric scatterometer. The experimental measurements were conducted for three soil surfaces with different roughnesses under both dry and wet conditions. In this chapter, only wet soil surfaces were examined. Because theoretical surface scattering models were found incapable of predicting the measured backscatter, a semi-empirical

surface scattering model was developed that relates the surface scattering component of the total backscatter to the roughness parameter and the dielectric constant of the soil surface. The proposed model was in good agreement with experimental observations of wet soils at 60 GHz done by Yamasaki *et al.* [73].

In Chapter 4, the surface and volume scattering contributions to the measured backscattering response from dry soil surfaces were considered. Evidence on the presence of significant volume scattering from a dry soil surface at millimeter-wave frequencies was presented. A model based on radiative transfer theory was introduced to compute the volume scattering contribution from a thin dry soil layer with an undulating surface. This approach, which led to good agreement with the experimental observations, indicates that at 94 GHz the surface and volume scattering components are of comparable magnitude for σ^o_{vv} and σ^o_{hh}, but for the cross-polarized σ^o_{hv}, volume scattering is the dominant contribution.

In Chapter 5, a novel technique for the bistatic scattering measurement of point targets was developed. In this technique, a monostatic radar with fine spatial resolution in conjunction with a rotatable ground plane were used to measure the bistatic scattering matrix. The new technique circumvents the difficulties associated with the traditional measurement technique. It was shown that for depolarizing targets, an independent radar measurement after loading the ground plane with a dielectric slab is required for determining the cross-polarized components of the bistatic scattering matrix. The accuracy of the new method was demonstrated by comparing the measured bistatic scattering matrices of cylinders and spheres with the theoretical ones over a wide range of scattering angles.

In Chapter 6, a new technique for measuring the effective propagation constant of dense random media was introduced. The proposed method is not restricted by the

physical properties of the random medium such as particles size, shape and density. In this technique, the mean bistatic scattered fields of a cluster of random medium, confined in a known geometrical boundary, are measured using a monostatic radar and a rotatable ground plane. Then the measured mean bistatic scattered fields are fitted to the bistatic scattered fields of a homogeneous lossy material with the same geometrical boundary. The accuracy of the new technique in measuring the effective propagation constant of a dense random medium was verified both experimentally and numerically in the low volume fraction limiting case. It was also shown that using this technique, the permittivity of low dielectric materials such as styrofoam can be measured very accurately.

In Chapter 7, an experimental study of the effective propagation constant of dense random media aimed at establishing the region of validity of existing theoretical models was performed using the measurement technique developed in Chapter 6. Measurements of the effective propagation constants of different dense random media comprised of homogeneous spherical particles with different packing densities were compared with existing analytical models. It was shown that none of the existing analytical models, including the QCA-CP model that was developed specifically for dense media, were able to predict the extinction accurately at volume fractions beyond 10%. It was also shown that Polder-Van Santen mixing formula can be used to predict the real part of the effective propagation constant with reasonable accuracy.

8.2 Recommendations for Future Work

The semi-empirical surface scattering model that is developed in this thesis is based on a limited number of different soil surfaces. Since, the backscattering response

from soil is a function of the surface height statistics and dielectric properties of the soil medium, it would be recommended to conduct additional measurements over a wide range of surface roughnesses, soil types, and wetnesses. In particular, further measurements are needed for surfaces with short correlation lengths which were not covered in the present model.

Effects of soil moisture, in the transition region between wet and dry soil conditions ($0 < m_v < 10\%$), on the relative contribution of both volume and surface scattering to the backscattering response at millimeter-wave frequencies is another problem of interest. We believe that this problem can be best solved by conducting a set of indoor measurements in a controlled laboratory enviroment where soil moisture can be controlled easily. In fact, with an indoor experimental setup, surface scattering contribution can be easily minimized by "smoothing" the top soil layer so that only volume scattering from within the soil layer is studied. Issues like the effects of particle size distribution, layer depth, volume density, and soil moisture content can all be probed closely for different types of soil.

The effective propagation constant was measured for dense random media consisting of particles with size parameters $ka < 1$. We propose extending the experimental study to dense random media consisting of particles with size parameters between 1 and 10. This can be particularly useful at millimeter-wave frequencies where snow and soil particles are of appreciable size compared to wavelength. For these size parameters we expect significant scattering loss due to multiple scattering between the particles.

We have established through our measurements of the effective propagation constant of dense random media that existing theoretical models do not consistently predict the amount of scattering loss in the medium. We have at this point three

options to pursue: (a) develop new theoretical models that include higher orders of multiple scattering, (b) develop an empirical model that can predict the effective propagation constant of dense random media based on extensive measurements spanning the parameter space, and (c) develop computer programs that can simulate numerically the expected bistatic scattered fields from a cluster of particles of a dense medium, from which the effective propagation constant can be computed using a technique similar to the measurement technique introduced in Chapter 6.

The new measurement techniques described in Chapters 5 and 6 provide us with powerful tools to measure not only the effective propagation constant of dense random medium but also the incoherent bistatic scattered fields which are proportional to the phase function. Recall that the extinction coefficient and phase function are fundamental quantities in the radiative transfer equation which basically determine the propagation and scattering behavior of a wave in a random medium. We have shown experimentally that the existing theoretical models have failed in predicting accurately the extinction in dense random media with fractional volumes beyond 10%. We believe that the best approach to modeling scattering from dense random media is to develop a hybrid experimental/theoretical model. In the hybrid model, the experimentally determined extinction and phase function are used in the mathematical machinary of the radiative transfer model. The concept of the hybrid model is a very powerful one since it comprises the strengths of each approach while minimizing their respective weaknesses.

APPENDIX

APPENDIX

DERIVATION OF THE JOINT PROBABILITY DENSITY FUNCTION $P_{\theta_t,\phi_t}(\theta_t, \phi_t)$

For most natural surfaces, the surface height $z(x,y)$ is a stationary Gaussian random process with zero mean and variance s^2, and an autocorrelation function ρ. It can be shown that the surface slopes Z_x and Z_y along x and y respectively are normal and independent random processes with their joint probability density function given by

$$P_{Z_x,Z_y}(Z_x, Z_y) = \frac{1}{2\pi m^2} e^{-(Z_x^2+Z_y^2)/2m^2} \tag{A.1}$$

where the variance is given by $m^2 = s^2\rho''(0)$. In the case of a Gaussian surface auto-correlation function, the rms slope is $m = \sqrt{2}\ s/l$, where l is the correlation length.

To derive the joint probability density function of the angles θ_t and ϕ_t, it is essential to first relate these angles to the surface slopes Z_x and Z_y. This can be accomplished by recognizing that the unit vector $\hat{n}$ representing the surface normal

can be expressed in terms of the surface slopes as follows

$$\hat{n} = (-Z_x\,\hat{x} - Z_y\,\hat{y} + \hat{z})\,D_o \tag{A.2}$$

with $D_o = 1/\sqrt{1 + Z_x^2 + Z_y^2}$. The surface slopes can be related to angles θ_t and ϕ_t by equation (4.7) to (A.2).

$$\begin{aligned} \cos\phi_t \sin\theta_t &= -Z_x\,D_o \\ \sin\phi_t \sin\theta_t &= -Z_y\,D_o \\ \cos\theta_t &= D_o \end{aligned}$$

and after simple algabraic manipulations, we obtain

$$\begin{aligned} Z_x &= -\frac{\cos\phi_t \sin\theta_t}{\cos\theta_t} \\ Z_y &= -\frac{\sin\phi_t \sin\theta_t}{\cos\theta_t} \end{aligned} \tag{A.3}$$

It is straight forward to show that the joint probability density function for the angles (θ_t, ϕ_t) takes the following form

$$P_{\theta_t,\phi_t}(\theta_t, \phi_t) = \frac{1}{2\pi m^2}\,\frac{\tan\theta_t}{\cos^2\theta_t}\,exp(-\tan^2\theta_t/2m^2) \tag{A.4}$$

In addition, the marginal probability density function of θ_t is obtained by integrating over ϕ_t

$$P_{\theta_t}(\theta_t) = \frac{1}{m^2}\,\frac{\tan\theta_t}{\cos^2\theta_t}\,exp(-\tan^2\theta_t/2m^2) \tag{A.5}$$

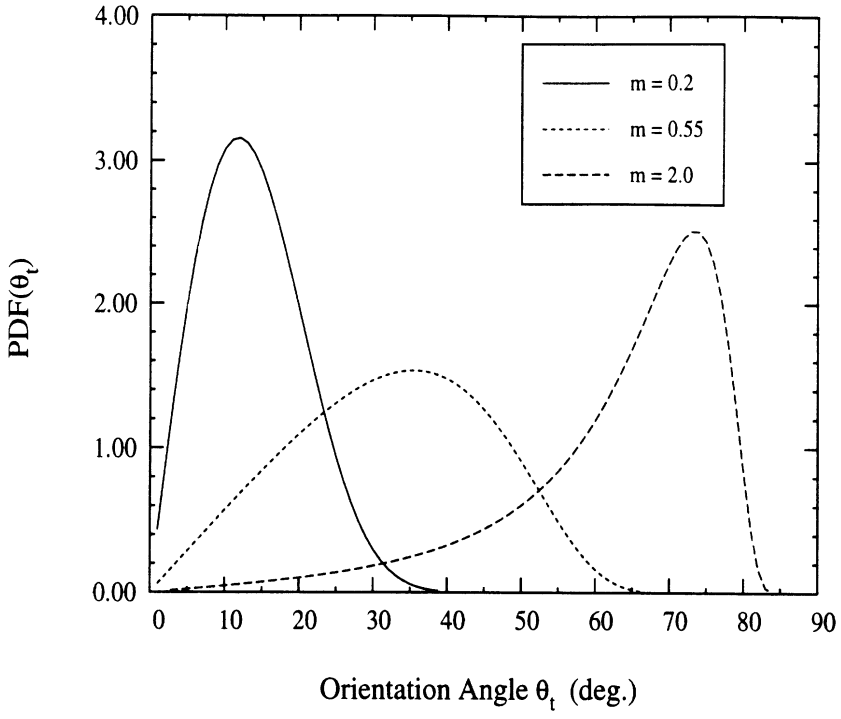

Figure A.1: The marginal probability density function $P_{\theta_t}(\theta_t)$ for different values of the rms slope m.

and is plotted in Fig. A.1 for different values of m.

BIBLIOGRAPHY

[1] Barnes, R.M., "Polarimetric Calibration Using in-scene Reflectors," Rep. TT.65, MIT, Lincoln Laboratory, Lexington, MA, Sept. 1986.

[2] Blom, R. G. and C. Elachi, "Spaceborne and Airborne Imaging Radar Observations of Sand Dunes," *J. Geophys. Res.*, vol. 86, pp. 3061, 1981.

[3] Bohren, C. F., and D. R. Huffman, *Absorption and Scattering of Light by Small Particles,* John Wiley, 1983.

[4] Borel, C., and R. E. McIntosh, "Millimeter Wave Backscatter from Deciduous Trees," *IEEE Trans. Antennas Propagat.,* vol. 38, no. 9, pp. 1391-1398, Sept. 1990.

[5] Borgeaud, M., R. T. Shin, and J. A. Kong,"Theoretical Models for Polarimentric Radar Clutter," *J. Electromagn. Waves Appl.*, vol. 1, no. 1, pp. 73-89, 1987.

[6] G. S. Brown, "Coherent Wave Propagation Through A Sparse Concentration of Particles," *Radio Sci.,* Vol. 15, No. 3, pp. 705-710, 1980.

[7] Bush, T. F., F. T. Ulaby, and W. H. Peake, "Variability in the Measurement of Radar Backscatter," *IEEE Trans. Antennas Propag.,* vol. 24, pp. 896-899, 1976.

[8] W. C. Chew, *Waves and Fields in Inhomogeneous Media,* Van Nostrand Reinhold, 1990.

[9] Cosfriff, R.L., W. H. Peake, and R. C. Taylor,"Terrain Scattering Properties for Sensor System Design (Terrain Handbook II)," Engineering Experiment Station Bulletin 191, Ohio State University, 1960.

[10] De Roo, R.D., and F.T. Ulaby,"Bistatic Specular Scattering from Rough Dielectric Surfaces," *IEEE Trans. Antennas Propagat.*, vol. 42, No. 2, pp. 220-231, Feb. 1994.

[11] Ding, K. H., and L. Tsang,"Effective Propagation Constants of Dense Nontenuous Media with Multi-Species of Particles," *J. Electro. Waves Applic.,* Vol. 2, No. 8, pp. 757-777, 1988.

[12] K. H. Ding,"Electromagnetic Wave Propagation and Scattering in Dense Media," Ph. D. Thesis, Univeristy of Washington, 1987.

[13] Ding, K. H., C. E. Mandt, L. Tsang, and J. A. Kong, "Monte Carlo Simulations of Pair Distribution Functions of Dense Discrete Random Media With Multiple Sizes of Particles," *J. Electro. Waves Applic.,* vol. 6, no. 8, pp. 1015-1030, 1992.

[14] Dobson, M.C., F.T. Ulaby, M. T. Hallikainen, and M.A. El-rayes, "Microwave Dielectric Behavior of Wet Soil-Part II: Dielectric Mixing Models," *IEEE Trans Geosci. Remote Sensing*, vol. GE-23, pp. 35-46, Jan. 1985.

[15] A. Fung,"A Review of Volume Scatter Theories for Modeling Applications," *Radio Sci.,* vol. 17, no. 5, pp. 1007-1017, 1982.

[16] Fung, A. K., and M. F. Chen, "Scattering from a Rayleigh Layer with an Irregular Interface," *Radio Sci.,* vo. 16, no. 6, pp. 1337-1347, 1981.

[17] Hallikainen, M. T., F. T. Ulaby, and M. Abdelrazik,"Dielectric Properties of Snow in the 3 to 37 GHz Range," *IEEE Trans. on Antennas and Propagat.,* vol. AP-34, no. 11, pp. 1329-1340, Nov. 1986.

[18] J. R. Huynen "Measurement of Target Scattering Matrix," *Proc. IEEE,* vol. 53, pp. 936-946, 1965.

[19] A. Ishimaru, *Wave Propagation and Scattering in Random Media,* Academic Press, 1978.

[20] Kendra, J. R., F. T. Ulaby, and K. Sarabandi,"Snow Probe for *In Situ* Determination of Wetness and Density," *IEEE Trans. Geosci. Remote Sensing*, vol. 32, No. 6, pp. 1152-1159, 1994.

[21] Kuga, Y., F.T. Ulaby, T. F. Haddock, and R. D. DeRoo, " Millimeter-wave Radar Scattering from Snow 1. Radiative Transfer Model," *Radio Sci.*, vol. 26, pp. 329-341, March-April 1991.

[22] Lee, J. K., and J. A. Kong,"Active Microwave Remote Sensing of an Anisotropic Random Medium Layer," *IEEE Trans. Geosci. Remote Sensing*, vol. GE-23, no. 6, pp. 910-923, Nov. 1985.

[23] Lim, H. H., M. E. Veysoglu, S. H. Yueh, R. T. Shin, and J. A. Kong, "Random Medium Model Approach to Scattering From a Random Collection of Discrete Scatterers," *J. Electromagn. Waves Appl.*, vol. 8, no. 7, pp. 801-817, 1994.

[24] Ma, Q., A. Ishimaru, P. Phu, and Y. Kuga, "Transmission, Reflection, and Depolarization of an Optical Wave for a Single Leaf," *IEEE Geosci. Remote Sens.,* vol. 28, no. 5, pp. 865-872, 1990.

[25] Ma, Q., A. Ishimaru, and Y. Kuga, "Scattering and depolarization of Waves Incident Upon a Slab of Random Medium with Refractive Index Different From that of the Surrounding Media," *Radio Sci.*, vol. 25, no. 4, pp. 419-426, 1990.

[26] K. McDonald,"Modeling Microwave Backscatter from Tree Canopies," Ph.D. dissertation, The University of Michigan, Ann Arbor, MI, 1989.

[27] Mandt, C. E., Y. Kuga, L. Tsang, and A. Ishimaru,"Microwave Propagation and Scattering in a Dense Distribution of Non-tenuous Spheres: Experiment and Theory," *Waves in Random Media,* vol. 2, pp. 225-234, 1992.

[28] Mautz, J. R., and R. F. Harrington,"Radiation and Scattering From Bodies of Revolution," *Appl. Sci. Res.,* vol. 20, p. 405, 1969.

[29] Mead, J. B., P. M. Langlois, P. S. Chang, and R. E. McIntosh, "Polarimetric Scattering from Natural Surfaces at 225 GHz," *IEEE Trans. Antennas Propagat.,* vol.39, no. 9, pp. 1405-1411, Sept. 1991.

[30] J.B. Mead, "Polarimetric Measurements of Foliage and Terrain at 225 GHz," Ph.D. thesis, University of Massachusetts, Amherst, MA, 1990.

[31] Nyfors, E., and P. Vainikainen, *Industrial Microwave Sensors,* Artech House, 1989.

[32] T. Oguchi, "Electromagnetic Wave Propagation and Scattering in Rain and other Hydrometeors," *Proc. IEEE*, vol. 71, no. 9, pp. 1029-1078, Sept. 1983.

[33] Oh, Y., K. Sarabandi, and F.T. Ulaby, "An Empirical and an Inversion Technique for Radar Scattering from Bare Soil Surfaces," *IEEE Trans Geosci. Remote Sensing*, vol. GE-30, pp. 370-381, Mar. 1992.

[34] Oh, Y., K. Sarabandi, and F.T. Ulaby, "An Empirical Model for Phase Difference Statistics of Rough Surfaces,"*Proceedings of IGARSS '93 Symposium*, Tokyo, Japan, vol. III, pp. 1003-1005, August 1993.

[35] Pak, K., L. Tsang, L. Li, and C. H. Chan, "Combined Random Rough Surface and Volume Scattering Based on Monte Carlo Simulations of Solutions of Maxwell's Equations," *Radio Sci.*, vol. 28, no. 3, pp. 331-338, 1993.

[36] Peake, W. H., and T.L. Oliver, "The Response of Terrestrial Surfaces at Microwave Frquencies," Air Force Systems Command, Air Force Avionics Laboratory, Technical Report AFAL-TR-70-301 (AADD 884 106), 1971.

[37] Polatin, P.F., K. Sarabandi, and F.T. Ulaby,"Monte Carlo Simulation of Electromagnetic Scattering from a Heterogeneous TwoCcomponent Medium," *IEEE Trans. Antennas Propagat.,* submitted for publication (Nov. 1993).

[38] Press, W.H., S.A. Teukolsky, W.T. Vetterling, and B.P. Flannery, *Numerical Recipes in FORTRAN: the art of scientific computing,* Cambridge University Press, 2nd edition, 1992.

[39] Ruck, G. T., D. E. Barrick, W. D. Stuart, and C. K. Krichbaum, *Radar Cross Section Handbook,* Plenum Press, New York, 1970.

[40] Sarabandi, K., and F.T. Ulaby, "A Convenient Technique for Polarimetric Calibration of Radar Systems," *IEEE Trans. Geosci. Remote Sensing*, vol. 28, No. 6, pp. 1022-1033, Nov. 1990.

[41] K. Sarabandi, "Simulation of A Periodic Dielectric Corrugation With An Equivalent Anisotropic Layer," *Int. Journal Infra. Millimeter Waves*, vol. 11, No. 11, pp. 1303-1321, Nov. 1990.

[42] K. Sarabandi,"Electromagnetic Scattering From Vegetation Canopies," Ph.D. dissertation, University of Michigan, Ann Arbor, Mi, 1989.

[43] Sarabandi, K., T.B.A. Senior, and F.T. Ulaby,"Effect of Curvature on the Backscattering from a Leaf," *J. Electro. Waves Appl.*, vol. 2, no. 7, pp. 653-670, 1988.

[44] K. Sarabandi,"Derivation of Phase Statistics From The Mueller Matrix," *Radio Sci.*, vol.27, No. 5, pp. 553-560, Sept.-Oct. 1992.

[45] Sarabandi, K., and Eric S. Li, "A Microstrip Ring Resonator for Soil Moisture Measurements," *IEEE Trans. Geosci. Remote Sensing*, in review.

[46] Sarabandi, K., and A. Nashashibi, " A Novel Bistatic Scattering Matrix Measurement Technique Using A Monostatic Radar," *IEEE Trans. Antennas and Propagat.*, accepted for publication.

[47] Sarabandi, K., F.T. Ulaby, and M.A. Tassoudji, "Calibration of Polarimetric Radar Systems with Good Polarization Isolation", *IEEE Trans. Geosci. Remote Sensing*, vol. 28, no. 1, 1990.

[48] Sarabandi, K., and P. Siqueira, "Numerical Scattering Analysis for Two Dimensional Dense Random Media: Characterization of Effective Permittivity," *IEEE Trans. Antennas and Propagat.*, in review.

[49] Senior, T.B.A., K. Sarabandi, and F.T. Ulaby,"Measuring and Modeling the Backscattering Cross Section of a Leaf," *Radio Sci.*, vol. 22, No. 6, pp. 1109-1116, Nov. 1987.

[50] Siquiera, P., and K. Sarabandi,"Numerical Simulation of Scatterer Positions in a Very Dense Medium with an Application to the Two-Dimensional Born Approximation," *Radio Sci.*, accepted for publication.

[51] Tassoudji, M. A., K. Sarabandi, and F.T. Ulaby, " Design Consideration and Implementation of The LCX Polarimetric Scatterometer (POLARSCAT)," University Of Michigan, Ann Arbor, MI, Radiation Lab. Tech. Rep. 022486-4-T, June 1989.

[52] Tsang, L. , J. A. Kong, and R. T. Shin, *Theory of Microwave Remote Sensing*, John Wiley, 1985.

[53] Tsang, L. and A. Ishimaru,"Radiative Wave Equations for Vector Electromagnetic Propagation in Dense Nontenuous Media," *J. Electromagn. Waves Appl.*, vol. 1, no. 1, pp. 52-72, 1987.

[54] L. Tsang and J. A. Kong,"Multiple Scattering of Electromagnetic Waves by Random Distribution of Discrete Scatterers with Coherent Potential and Quantum Mechanical Formulism," *J. Appl. Phys.,* vol. 15, pp. 3465-3485, 1980.

[55] Tsang, L., and J. A. Kong, "Scattering of Electromagnetic Waves from a Dense Medium Consisting of Correlated Mie Scatterers With Size Distributions and Applications to Dry Snow," *J. Electromagn. Waves Appl.*, vol. 6, no. 3, pp. 265-286, 1992.

[56] L. Tsang, "Dense Media Radiative Transfer Theory For Dense Discrete Random Media with Particles of Multiple Sizes and Permittivities," Progress in Electromagnetics Research, vol. 6, ch. 5. New York: Elsevier, 1992.

[57] Tsang, L., C. E. Mandt, and K. H. Ding, "Monte Carlo Simulations of the Extinction Rate of Dense Media with Randomly Distributed Dielectric Spheres Based on Solution of Maxwell's Equations," *Optical Society of Aomerica*, pp. 314-316, 1992.

[58] Ulaby, F. T., K. Sarabandi, K. McDonald, M. Whitt, and M. C. Dobson, "Michigan Microwave Canopy Scattering Model (MIMICS)," Radiation Laboratory Rep. 022486-T-1, The University of Michigan, Ann Arbor, MI, 1988.

[59] Ulaby, F. T., T. H. Haddock, and Y. Kuga, "Measurement and Modeling of Millimeter-Wave Scattering from Tree Foliage," *Radio Sci.,* vol. 25, no. 3, pp. 193-203, 1990.

[60] Ulaby, F. T., and C. Elachi, *Radar Polarimetry for Geoscience Applications,* Artech House, 1990.

[61] Ulaby, F. T., M. Whitt and K. Sarabandi, "AVNA-Based Polarimetric Scatterometers," IEEE AP magazine, vol. 32, 1990.

[62] Ulaby, F. T., R.K. Moore, and A.K. Fung, *Microwave Remote Sensing*, Vol.II-III, Artech, 1986.

[63] F. T. Ulaby," Radar Signatures of Terrain: Useful Monitors of Renewable Resources," *Proc. IEEE*, vol. 70, no. 12, pp. 1410-1428, Dec. 1982.

[64] Ulaby, F. T., T. H. Haddock, and Y. Kuga, "Measurement and Modeling of Millimeter-Wave Scattering from Tree Foliage," *Radio Sci.,* vol. 25, no. 3, pp. 193-203, May-June, 1990.

[65] Ulaby, F. T., T. E. Van Deventer, J. R. East, T. H. Haddock, and M. E. Coluzzi, "Millimeter-Wave Bistatic Scattering from Ground and Vegetation Targets," *IEEE Trans Geosci. Remote Sensing*, vol. 26, no. 3, pp. 229-243, May 1988.

[66] Ulaby, F. T., and T. F. Haddock, "Millimeter-Wave Radar Scattering From Terrain: Data Handbook (Version 2)," University of Michigan, Ann Arbor, MI, Radiation Lab. Tech. Rep. 026247-4-T, Sept. 1990.

[67] Van Deventer, T.E., J.R. East, and F.T. Ulaby,"Millimeter Transmission Properties Of Foliage," *1987 IEEE Int. Geosc. Remote Sensing Symposium*, Ann Arbor, Michigan.

[68] Wen, B., L. Tsang, D. P. Winebrenner, and A. Ishimaru, "Dense Medium Radiative Transfer Theory: Comparison with Experiment and Application to Microwave Remote Sensing and Polarimetry," *IEEE Trans. Geosci. Remote Sensing*, vol. 28, no. 1, pp. 46-59, Jan. 1990.

[69] West, R., L. Tsang, and D. P. Winebrenner,"Dense Medium Radiative Transfer Theory for Two Scattering Layers with a Rayleigh Distribution of Particle Sizes," *IEEE Trans. Geosci. Remote Sensing*, vol. 31, no. 2, pp. 426-437, Mar. 1993.

[70] M. W. Whitt, "Microwave Scattering From Periodic Row-Structured Vegetation," Ph.D. dissertation, The University of Michigan, Ann Arbor, MI, 1991.

[71] Whitt, M.W., F.T. Ulaby, P. Polatin, and V.V. Liepa, "A General Polarimetric Radar Calibration Technique," *IEEE Trans. Antennas Propagat.*, vol. 39, no. 1, pp. 62-67, Jan. 1991.

[72] Whitt, M.W., and F.T. Ulaby,"A Polarimetric Radar Calibration Technique with Insensitivity to Target Orientation," *Radio Sci.*, vol. 25, no. 6, pp. 1137-1143, Nov.-Dec. 1990.

[73] Yamasaki, H., J. Awaka, A. Takahashi, K. Okamoto, and T. Ihara, "Measurements of Soil Backscatter with A 60 GHz Scatterometer," *IEEE Trans Geosci. Remote Sensing*, vol. GE-31, pp. 761-766, July 1992.

[74] Zhou, J. L., and A. L. Tits, " User's Guide for FSQP Version 3.3b: A FORTRAN Code for Solving Constrained Nonlinear (Minimax) Optimization Problems, Generating Iterates Satisfying All Inequality and Linear Contraints," *Electrical Engineering Department and Institute for Systems Research,* University of Maryland, Colledge Park, MD.

[75] Zurk, L. M., K. H. Ding, L. Tsang, and D. P. Winebrenner, "Monte Carlo Simulations of the Extinction Rate of Densely Packed Spheres with Clustered and Non-Clustered Geometries," *IEEE Int. Geosci. Remote Sens. Sympos.*, pp. 535-537, 1994.